UNIVERSITY OF LIVERPOOL

A Modelling Study of Transparent Cathode Discharge Breakdown

Thesis submitted in accordance with the requirements of the University of Liverpool for the degree of Doctor in Philosophy by

Ali Hussein Al-Khateeb

August 2018

بسم الله الرحمن الرحيم

Dedication

To the

Memory of My Parents,

My Wife and Sons,

My Brother and Sister and their families

Declaration

I hereby declare that this thesis is my own work and no further sources of information have been used other than the references cited.

Abstract

Transparent cathode discharge (TCD) devices, from their name, have a transparent cathode rather than the conventional solid cathode by constructing it of metal grid wires. They have been proposed initially in the early fifties as an approach to confine a hot fusion plasma. Interest has grown in these devices since they have offered a compact source to generate by-products for many applications. Most research in this area focuses on operation stage of the discharge rather than the ignition stage which has a significant effect on that stage, this thesis establishes a two dimensional model for the ignition stage of a cylindrical TCD, and compares it to the experimental work carried out separately within the group.

A particle trajectory simulation was developed to study this problem. The code calculated the trajectory of charged and fast neutral particles in the vacuum electric fields, and included collisions in the gas-phase between these particles and the background neutrals, and on the electrode and chamber wall surfaces. The onset breakdown was determined by monitoring the increase of the charged particles in the first few microseconds of the calculation.

The work studied the effects of individual mechanism on breakdown such as, effects of fast neutrals, and surface effect processes, such as secondary electron emission, particles backscattering, and also ion and neutral conversion by reflection. It has been shown that these mechanisms became less effective as the pressure increased.

Cumulative effects of particle processes where also studied, which revealed that the electron backscattering is the most effective process.

Another interesting result was the accumulation of ion population in the interior of the cathode at the end of simulation which is explained as the early stages of virtual electrode formation.

Furthermore, the effects of changing some factors in the geometry of the original (experimental) configuration are discussed as well.

The cases studied were, changing number of electrode wires, 8-wire 20-wire respectively, changing anode radius, smaller 4.3 cm and larger 7.2 cm, and unaligned anode and cathode, i.e. the anode was rotated half the angle between the apertures, so the electrode apertures were not facing each other.

The effects of electrical potential distribution and transparency due to these changes, resulting changes in ion microchannel was confirmed.

The result showed that these effects became less as the pressure increased, where the electron became more effective which reduces the effects of ion microchannels.

Acknowledgments

I here would like to thank my government, the Foundation of Political Prisoners, Baghdad University, my department for nominate me to study Ph. D., also I would thank University of Liverpool, Electrical and Electronic Engineering Department, Plasma Group for offering me the opportunity to do my Ph.D.

I would like to my great gratitude and thankfulness to my supervisor Dr. Mark Bowden for his guidance, patience, kindness, I learned a lot from him and will always be beholden for him. I would also thank Dr. Paul Bryant, Samuel M. for explaining basics of PIC code, special thanks to Dr. Mohammad Hasan who offered me support all the time, also special thanks to Dr. Thomas Hardiment my office made, for friendly discussion, I am grateful to his kindness proof reading my thesis.

I would like to thank all my colleagues who offered me a very friendly environment, my family who suffered a lot until I reach this stages, and all my friend who supported me.

Content

List of Abbreviations

1D 1v	one dimension one velocity component
2D	Two dimension
3D	Three dimension
BS	Backscattering
CIC	Cloud in Cell
DMC	Direct Monte Carlo
FDM	Finite Difference Method
IEC	Inertial Electrostatic Confinement
MFP	Mean Free Path
Pd	Pressure Electrode-Distance
PIC	Particle in Cell
PIC-MCC	Particle in Cell – Monte Carlo Collision
SE	Secondary Electron
SEE	Secondary Electron Emission
SEY	Secondary Electron Yield
TCD	Transparent Cathode Discharge

Chapter 1

1.1 Introduction

A Transparent cathode discharge (TCD) is a low-pressure electrical discharge struck between concentric electrodes - spherical or cylindrical - in which the cathode or both anode and cathode, are in the form of a transparent metal grid. Interest in these devices comes from their simple construction and near-term applications, examples include a small neutron source for Neutron Activation Analysis (NAA) to determine impurities in ores or coal at the mine. Extension of that technology discussed in this book includes land mine detection, neutron radiography, clandestine material detection at air- and seaports, medical isotope production, plasma space propulsion, subcritical fusion–fission hybrid reactors, and tunable x-ray sources, to name a few [1].

Modelling the ignition phase of a cylindrical TCD is the aim of this work to gain a better understanding and predication of the effects of different factors on such discharges, such as the operating voltage, when the electrons start to have effect on the regime, the early stages of virtual electrode formation. The work will focus on helium He since it matches the original purpose these devices proposed for in addition of the availability of researches to compare with. A related basic background will be extended in the next sections of this chapter.

1.2 Plasma

When a significant amount of a matter is charged particles, ions and electrons, interacting with neutrals, this matter is said to be in plasma state. Plasma is an ionized gas (sometimes referred to as the fourth state of matter), most of the universe is in this state, such as sun,

stars, and across interstellar space. The ionosphere and Aurora are examples of plasma on earth.

As the charged particles in plasma move around, they can generate local concentration of positive or negative charges, which give rise to electric fields. The motion of charges also generates currents, and hence magnetic fields, these fields affect the motion of other charged particles far away [2].

Plasmas are characterize by particle density *n* (i.e. n_e , n_i , n_n , for electron, ions and neutral densities respectively), temperature or mean energy of each species *T* (in eV, where 1 eV = 11605 K), and steady- state magnetic field B (in tesla) [3]. They are also characterized as fully ionized and partially ionized plasmas, where the fractional ionization or degree of ionization ($\frac{n_i}{n_i+n_n}$) is important. Based on the relative temperature between plasma species, plasma is classified into thermal or hot plasma, where electrons and heavy particles are in thermal equilibrium, electrons, ions and neutrals temperatures are equal, $T_e = T_i = T_n$, i.e. in Maxwellian distribution, and non-thermal and cold plasmas, where $T_e >> T_n$ (non-Maxwellian). Plasma differs as well in extent, density and way or place of existence (i.e. DC, RF power source, terrestrial or space etc.) [4], Fig. (1-1) shows number of different states of matter and plasmas.

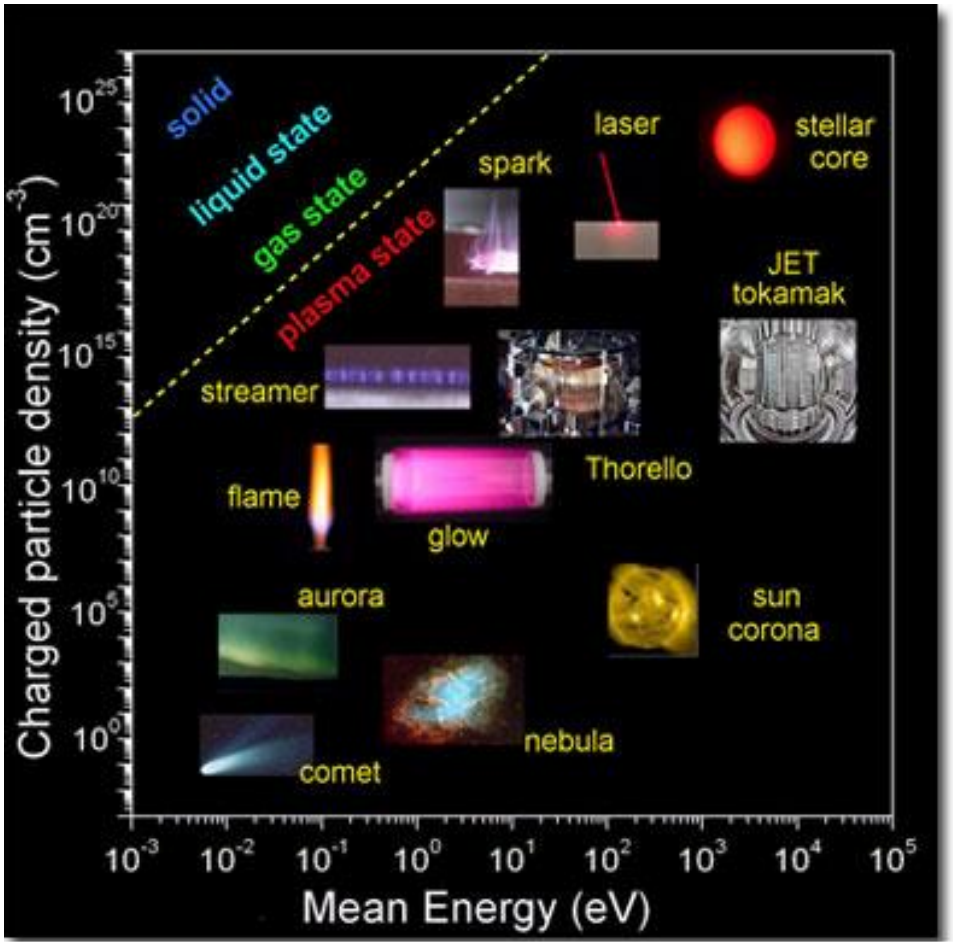

Fig. 1-1

Different states of matter and plasmas (energy eV vs charged particles density particle/cm^{-3}) [5]

Topics studied in plasma physics are many and varied. Some of these are directed towards controlled thermonuclear fusion (terrestrial), such as in magnetic confinement devices like tokamaks, stellarators, reversed field pinches, mirror devices, in which an externally produced 1-10 T magnetic field of carefully chosen geometry is imposed on plasma (hydrogen or deuterium), with densities ranging from 10^{19}-10^{21} m^{-3} and 10-10^4 eV temperatures. Another approach, inertial confinement fusion uses fast pulsed laser focused to compress a plasma pellet rapidly to attain instant densities larger than solid density (~ 10^{28} m^{-3}). All of these devices are large, complex units, and very expensive. The inertial electrostatic confinement (IEC) approach offers smaller, easier to construct, and cheaper plants [2,3]. Transparent Cathode Discharge (TCD) is another name of these devices, the

plasma in these devices are non- Maxwellian, the ratio of ion to electron "temperature" (average energy) still need work to resolve in addition the electron temperature differs according to the fuel (talking about fusion) aimed for use [1], and the ion density in the core ~ 10^{16} cm^{-3} for spherical geometry, while the cylindrical geometry has less core density. Since they are the subject of this work they will be explained more in section 1.5.

Other terrestrial plasmas, e.g. arcs, neon signs, fluorescent lamps, processing plasmas, welding arcs, lightning etc., have T_e of a few eV and (T_i colder often room temperature). These are typically weakly ionized, dominated by collisional and radiative processes, with densities ranging from about 10^{14} to 10^{22} m^{-3} [3]. Other examples of plasmas are space plasmas. Their parameters cover wide range, apart from the neutral fusion plasmas in the stellar core, and for example their density varies from 10^{6} m^{-3} in interstellar space to 10^{20} m^{-3} in the solar atmosphere. Most of the investigated astrophysics plasmas have temperature in the range 1-100 eV and usually they are fully ionized.

To produce plasma, electrons need to gain sufficient energy (ionization energy) to be released from the neutrals of the gas - atoms or molecules, and produce pairs of charged particles, this requires very high temperatures, which alternatively can be achieved through electrical discharge, for example by applying sufficient high voltage between two electrodes in a chamber containing gas. The atoms and molecules become ionized, which lets current flow through the gas, the so called Plasma Breakdown. Due to the huge growth in plasma applications, and great development in science knowledge and technology, plasma remains a very active area of researches.

1.3 Gas Discharge

Gaseous discharges have a number of important applications ranging from materials processing to lasers [2]. A gas discharge can be viewed as the conduction of charge through

gas, due to movement of ions and electrons produced by collisions between charged particles and the neutrals. To explain a gas discharge, a schematic diagram of a low pressure D.C. discharge between two flat parallel plates and the voltage vs current characteristic of such discharge are illustrated in Fig. (1-2 a) and (1-2 b) respectively.

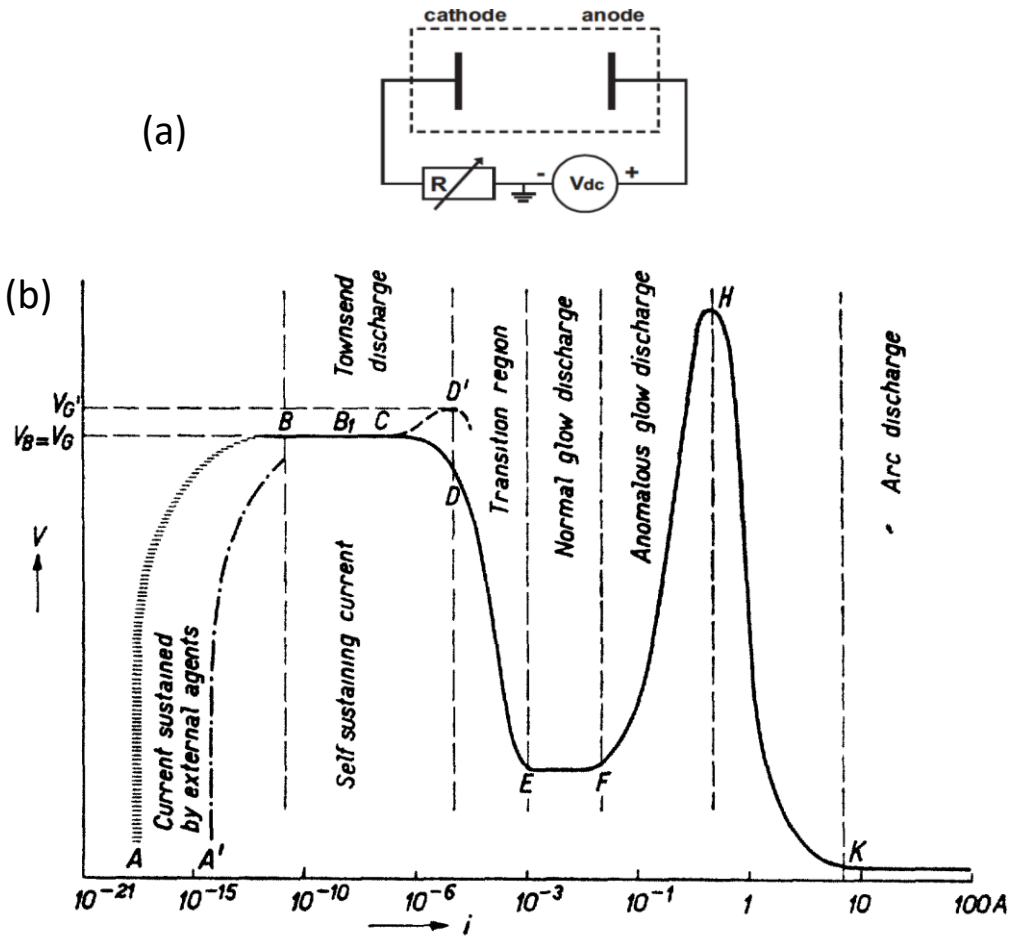

Fig. 1-2

(a) Schematic diagram of D.C. discharge between flat parallel plates [7],
(b) The voltage current characteristic for this type of discharge [8]

In the normal state, and with low values of voltages, a gas is a very good insulator. Nevertheless, even applying voltage between cold electrodes without photoelectric and auto-electronic emission, a very small current flows, which is due to ionization by external agents, such as cosmic rays, in form of random bursts, “A” in Fig. (1-2 b). If there is a supplementary source electrons such as a UV source, this part shifted to the right, “A’ ”. With increasing the applied voltage, the current increases very slowly in the beginning, then faster,

due to the secondary ionization; before point B, (region AB), if we apply an external source for creation of electrons, a somewhat higher steady current will be observed, and by removing this source the current reverted to the random bursts. Since it needs external source for the creation of electrons, it is characterized as the non-self-sustained discharge region.

By increasing the electrodes' voltage, current will increase very rapidly, while the voltage remains almost the same, this voltage is called the breakdown potential or Breakdown voltage V_B , (region BC). In this region increasing the applied voltage causes greater electric field in the discharge gap, until the electrons can ionize neutral gas atoms through impact, which in turn causes a multiplication of ions and electrons in the discharge gap. On the other hand, the ions impact on the cathode release new electrons by secondary emission. This compensates the electron loss at the anode, and sustains the current in the discharge gap, which doesn't change anymore by the removal of the external source. This is called Townsend or dark discharge - and it is characterized from now on as the self-sustained discharge region. The currents flowing in this discharge are small and the number of charged particle is limited, so space charges are negligible. Thus the electric field is uniform in the discharge gap, and determined by the geometry and the electrodes' voltage [6,7,8].

The glow discharge (region CH), which can be divided into three sub divisions; first, subnormal glow discharge, (region CDE), in which an additional voltage increase will cause significant space charge effects in the discharge gap. Due to the mobility differences between the ions and electrons, this space charge will be mainly positive and away from the cathode, generating a cathode fall region, which has almost the same potential difference between the electrodes. That means higher electric field, which leads to higher electron multiplication in this region, and allows the voltage needed to sustain the discharge to be reduced, therefore the *V* - *I* curve shows a voltage drop with current increase. This discharge is often

unstable and goes easily into the second, normal glow discharge, (region EF) [7]. This occurs when the formation of the cathode fall region is completed, so the minimum voltage required to sustain the discharge is reached, and the discharge covers only a part of the cathode. As the current increased, the discharge spreads on the cathode, so that the current density will remain the same. Since the voltage depends on the current density rather than the current itself, the voltage will remain constant, until the discharge covers the whole cathode. Finally, the abnormal glow discharge, (region FH) is reached; since the whole cathode is covered by the discharge, any increase in the current will cause an increase in the cathode fall, which consequently lead to voltage increase.

Following the glow discharge regime is arc discharge, region (HK). If the current is increased more, the voltage will reach a maximum, then drop down to very low values. This is because of the large ion current towards the cathode, causing it to be heated and thermoelectric emission will become the major factor affecting the discharge. The required voltage to sustain the discharge is then lowered substantially [6,7,8].

There are many types of gas discharges, such as micro-discharges, RF discharges and also including the transparent cathode discharge (TCD), where the cathode is transparent and its effect such as allowing the ions to go through to the other side, hence prolong their path and life-time and increase the ionization probability which reduce the breakdown voltage. However, the basic principles explained above still apply.

1.4 Plasma Breakdown

Vacuum breakdown or ignition can be defined in general as the transition process from an insulating neutral gas to a partially ionized conducting state [6,7,8]. Early studies of plasma breakdown were related to the investigations of the gas discharges themselves. In 1889

Paschen studied the minimum voltage needed to create a spark between two electrodes in a glass tube, a discharge close to that in Fig. (1-2 a). He found that this voltage depends on the type of the gas in the tube, the gas pressure *P*, the distance between the two electrodes *d*, and the electrode material. Fig. (1-3) shows a schematic plot of a graph for the relation between *Pd* and breakdown voltage V_B for different gases. These are nowadays known as Paschen curves. To achieve breakdown, two factors play the main role, ionization via collision electron with gas neutrals, and the secondary electrons created due to ions impacting the cathode. Increasing the pressure *P* reduces the main free path (MFP) of the electron, i.e. the average path the electron can move before facing a collision, so will reduce the energy electrons gain from the electric field before the next collision. If this energy is less than the ionization energy required for ionization collisions, consequently the voltage must increase; on the other hand, the distance between the electrodes *d* divided by the mean free path will set the average number of collisions with neutral, that an electron may face during a trip form the cathode to the anode. In other words, *Pd* determines the probable number of charged particle pairs created in this trip. Therefore, in the case of high values of *Pd*, the number of collisions will be higher, but the energy gained between two consecutive collisions will be lower, making the breakdown voltage V_B higher. Reducing *Pd* will reduce V_B gradually, until an minimum *Pd* value with $V_{B\,min}$ is reached, then the opposite situation takes place; higher energy gained between two consecutive collisions, and lower number of ionization collisions, due to longer mean free path, eventually results in enough ionization collisions to sustain the discharge. This explains the rapid increase in V_B with decreasing *Pd* decreased (the right side of *Pd* for $V_{B\,min}$ of the graph) called high-pressure insulation.

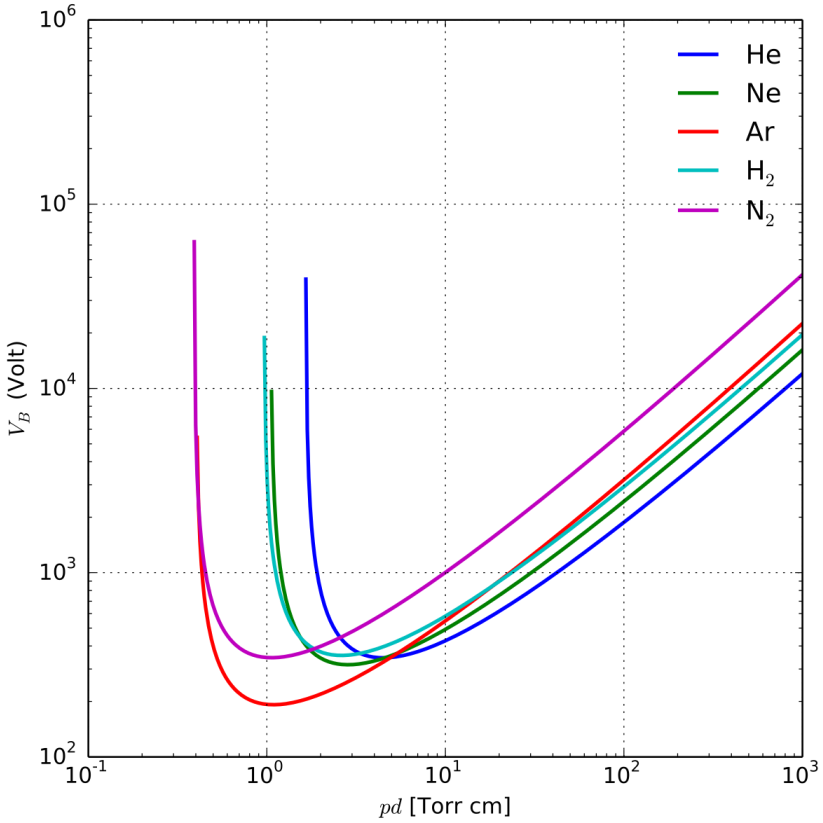

Fig. 1-3

Paschen curves, showing the breakdown voltage, V_B as function of *Pd* for different gases [9]

Paschen found that breakdown voltage was described [10]

$$V_B = \frac{BPd}{\ln(Apd) - \ln(\ln\left(1 + \frac{1}{\gamma_{se}}\right))} \qquad 1\text{-}1$$

Where V_B is the breakdown voltage in volts, *P* is the gas pressure, *d* is the gap distance in meters, γ_{se} is the secondary electron emission coefficient, *A* and *B* are constants determined experimentally, where *A* is the saturation ionization in the gas at a particular *E/P* (electric field/ pressure), and *B* is related to the excitation and ionization energies of the gas. They are found to be roughly constant over a restricted range of *E/P* for any given gas [9,10].

In the early twentieth century, Townsend proposed a theory that could explain Paschen's law and curves. He described neutral particles ionization by electron impact, charge multiplication in electron avalanches, secondary electron creation at the cathode surface by

ion impact, and proposed a breakdown criterion. Until today, Townsend theory is generally used in low pressure discharges, but since there are many types of gas discharges, as mentioned in the previous section, types of plasma breakdown are many as well. Some of these are not in agreement with Townsend theory, and Paschen's law is not applicable. A Transparent Cathode Discharge (TCD) is one of these, and this work is a contribution towards a better understanding of this kind of plasma breakdown, based upon which a new theory for such discharges may be developed, more details about the differences of discharge and breakdown in these devices will be discussed in the next section.

1.5 Transparent Cathode Discharge (TCD)

Transparent Cathode discharge (TCD) devices have concentric electrodes - spherical or cylindrical - in which either a single cathode or multiple electrodes are constructed of a transparent metal grid or a cage maintained on a stalk in the center of the discharge chamber. The anode may simply be the chamber wall. These devices were first proposed and studied in the 1950s and 1960s as a possible fusion reactor [11,12], suggesting electrostatic plasma confinement, in which the transparent cathode accelerates the positive ions to the center, and causes them to oscillate many times (2-3 times) before they are lost from the system. This prolong the ion trajectory and raise the ionization collision probability in addition to may generate a highly energetic ion population in the interior of the cathode, and increase the probability of two ions trajectories to intersect and perhaps undergo fusion [11,12,13]. Electrostatic confinement represents a dynamic situation where the inertia of the recirculating ions in the potential well electrostatically confines the electrons, thus the name "inertial electrostatic confinement (IEC)" [1], which is another name for these devices. IEC offers simplified support structures, plus the ability to create non-Maxwellian plasmas that can use various fusion fuels, and a number of near-term applications [1]. IEC recently has been

investigated as a compact fusion source, to generate by-products of fusion reaction for many applications; to name one example a small neutron source for neutron activation analysis (NAA) [1], where the device is built to use an ion source in the region between the grid and wall. To operate in this mode, the background neutral density must be large enough to sustain the gas discharge that serves as the ion source. As a result, the fusion reactions produced are predominantly due to collision of the ions and neutrals, while to achieve high fusion rate ions must be accelerated to high energies within a single free path with a high applied voltage. This is the beam- background reaction, instead of the ion beam-beam fusion reaction required to move to a suitable power-producing reactor. For this it seems to be necessary to generate ion externally and operate in low gas pressure regime, to avoid neutral charge exchange and scattering effects [1].

George H. Miley & S. Krupakar Murali [1], collected and summarized a lot of researches, works and ideas about IEC. They illustrated different set-ups design issues, fundamentals and applications, and so it is a very valuable reference for anyone interested in the field. In chapter 3 they discuss discharge and breakdown in IEC, stating that all DC discharge modes discussed in section 1-3 can occur in IEC, but that they are more complicated.

Miley, G.H., et al. [14], using a single grid spherical IEC, indicated that there are two key features:

1. Breakdown voltage V_B characteristics as a function of pressure-grid/wall distance *Pd*.
2. Formation of ion “microchannels” that carry the main ion flow through grid openings.

For fixed V_B , the value of *Pd* is about three times higher for both spherical and planar solid-cathode discharges, which is attributed to the transparency of the IEC grid cathode, which allows ion flow on a chord through the center of the grid to the opposite side. The main ion

flow through the microchannels (grid openings) results in an effective rather than the geometric grid transparency [14].

Horhberg, TA. [14,17], in his M.S. thesis derived an empirical scaling law from a plot of breakdown voltage V_B versus the parameter $A/(Pd)^2$, where A is the atomic mass of the gas species, as follows:

$$V_B \approx 0.118A / (Pd)^2 \qquad 1\text{-}2$$

where the units of the constant 0.118 are kV × (Torr × cm^2) / um (atomic mass unit)

For such devices, i.e. spherical single grid-type, and by equation (1-2) a good prediction of the operating voltage V can be made as well as break down voltage V_B, because $V \sim V_B$.

The cylindrical IEC can be viewed as a two dimensional form of the spherical IEC, so the gas discharge in these devices, in general, follows the same description. There is one exception, the "C-Device", which is cylindrical but uses a hollow electrode-type discharge [1].

Jung, Bong-Ki, et al. [16], worked on a cylindrical IEC device at various pressures and geometries to understand their effect on discharge. Three key features are observed and discussed:

1. Discharge voltage in IEC device increases with a less transparent cathode at an identical operating pressure.
2. A high voltage and current discharge can be obtained with higher operating pressure at an identical *Pd* value.
3. A high voltage discharge can be obtained without decrease of operating pressure by altering the cathode diameter in an IEC device.

Based on these results, it is supposed that transparency and size of cathode in an IEC device can be optimized for a high-voltage and high-current discharge with relatively high operating

pressure, to increase fusion reactions of beam-cathode surface and beam-background gas besides ion-ion fusion reactions in a continuous IEC discharge. Consequently, these results can be reflected in the design of a high-yield fusion source.

Both of these experiments (Miley, G.H., et al. [14] and Jung, Bong-Ki et al. [16]) were carried out at a very low pressure ($\leq$ 15 mTorr), and with little variation in conditions, (more details about these two experiments and their founding are discussed in section 5.5), which shows the limitation of experimental work verses simulation, where one or more factor can be changed at a time.

Most of the research on IEC focusses on the operation phase rather than the ignition phase, which is still little covered and not well understood, such as the effect configuration changes, individual mechanism, and cumulative effects of particles process. This work is an approach in that direction.

1.6 Modeling and Simulation

The term modeling means a system of assumptions, approximation, and mathematical equations based on theory (physics here) to describe a regime or a system or a physical phenomenon, or in other words a mathematical representation of a physical phenomenon. By solving the model's equations - mostly numerically, the phenomenon is simulated. Models are used to theoretically interpret and predict experimental observation [15].

In plasma modelling there are two major approaches, the fluid and particle approaches. In the fluid approach, the plasma particle species (ions, electrons, excited neutrals) are treated as fluids interacting with each other. This describes the plasma macroscopically, while in the particle approach the species' trajectories are tracked, and the interactions between them are treated through collisions. These are simulated by using random numbers, a technique

called Monte Carlo. Thus this approach models the plasma microscopically and called Monte Carlo models. Because the number of particles is too large, it is unfeasible to track all of them, and so the term “super particles” is proposed. Each of these will represent a group of particles say 10^7 particles, which are treated as test particles, and supposed to be sufficient to produce a reliable result, although it is still computationally expensive. In plasma breakdown there is no space charge and the number of particles are limited, so this problem does not exist. For the same reason no collective motion could assumed, hence the fluid approach is not suitable, and so the model in this thesis will consider the particle approach.

Two pioneer books on the particle approach (particle in cell PIC), “Plasma physics via computer simulation” by Bridsall, C.K., and Langdon, A.B. [20], and “computer simulation using particles” by Hockney, R.W., and Eastwood, J.W. [21], are the cornerstone to an understanding PIC, as they explained the principles and ideas for this approach. Fig. (1-4) shows a typical Particle In Cell with Monte Carlo Collision (PIC-MCC) simulation cycle.

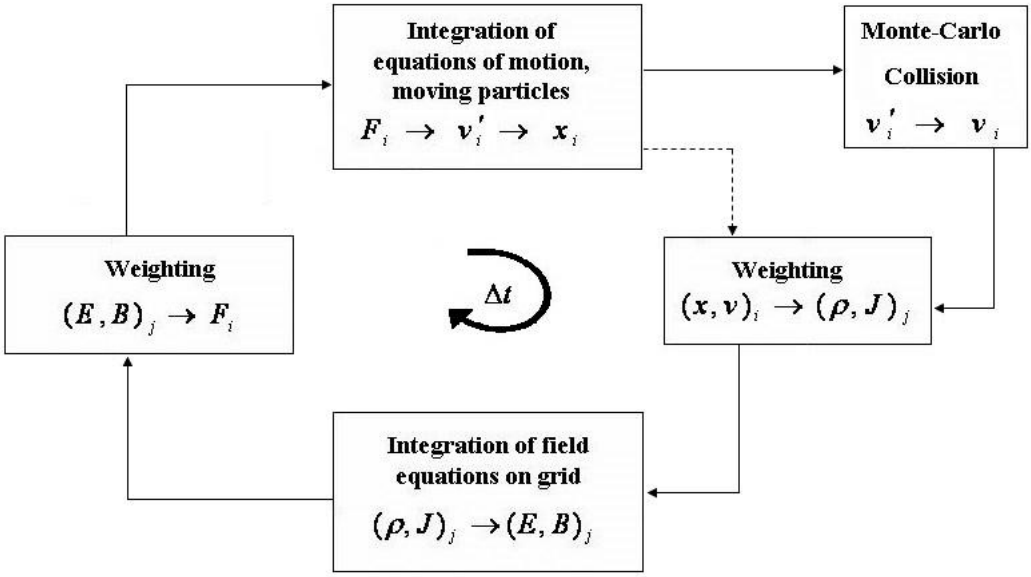

Fig. 1-4
Computing sequence for PIC-MCC with Monte Carlo collision velocity change made after the particle mover [18,19]

The simulation starts by initiating space and velocity (x_i, v_i) for each particle, and then calculating weighting of charge and current density. This is fed to the field solver, which calculate electric and magnetic fields, used to calculate the force acting on each particle. The next step is the particle mover which calculates the new velocity and new position for a short period of time Δt, and then a new cycle starts for another time step, by weighting charge and current density etc. Because the mathematical technique used for calculation is the finite difference (a discrete analogue of the derivative), Δt must be chosen optimally, small enough to minimize statistical error, and to get a reasonable output, but large enough to reduce computing expenses.

The Monte Carlo Collision technique is explained in many papers, e.g. Bridsall, C.K. [18], Tskhakaya, D. [22], which this work will depend on. Both of these explain the null collision technique which proposed by Skullerud, H.R. [25]. A crucial element of a breakdown collision model is the data set of cross-sections $\sigma(E)$ for different kinds of collision, especially for high energy ranges. This thesis will rely on the cross-sections adopted by Hartmann, P. et al. [23], and Liang Xu et al. [24], and a collisional model that is computationally efficient proposed by Nanbu, K. [26,27]. Details about particle approach, field solver, particle mover, velocity centering (Leap Frog), traditional collision model, null collision model, and Nanbu collision model will be discussed in the next chapter.

Since breakdown is effected by surface interactions, simulations do include such effects, like secondary electron emission, and backscattering or reflection, Langley, R.A. et al. [28] in a data compendium for plasma-surface interaction, discuss these interactions, and give an expression for reflection for ratio of average particle and energy reflected of light ions from solids (interest focused here on He from Fe).

Thomas, E.W. et al. [56], reviewed this expression for normal incident, and proposed another formula using six parameters, generalized for more targeted elements, gathering elements in groups that have the same parameters.

Eckstein, W. [57], surveyed calculated and experimental particle and energy reflection Coefficients, proposed more efficient formulas with four parameters rather than six (Thomas'). This work will adopt these formulas and parameters because they are recent, reviewed pervious researches and adopted by the IAEA.

Although Langley et al., also discussed electron backscattering and secondary electron yield, this work will rely on Baglin, V. et al. [29], for electron secondary yield by electron impact, Szapiro, B. et al. [30], for electron secondary yield by helium bombardment, and El Gomati, M.M. et al. [31], for electron backscattering, because they are more recent and cover wider ranges of energy. Baglin, V. et al. also looked at different conditions of surface treatments and their effects, the data for the surface as received will be used in this work because it is closer to experimental conditions, Szapiro, B. et al. used conditioned surfaces, and El Gomati, M.M. et al. compare a number of experimental and Monte Carlo simulations which make their data more considerable.

Thomas, T.M. et al. [32], and Souda, R. et al. [33], studied scattered He ion yield from He^{+}, He^{0}, and He^{*}, bombardment of solid surfaces. In theory ions are neutralized before reaching the surface; they assessed the ionization and reionization of scattered neutrals and ions, discussing the threshold energy of He^{0} to reflect as He^{+}, which differs for various surfaces, as well as the probability of such reflection. Their data are however very limited.

A cylindrical TCD to be simulated in this work, a schematic diagram of this configuration is illustrated in Fig (1-5)

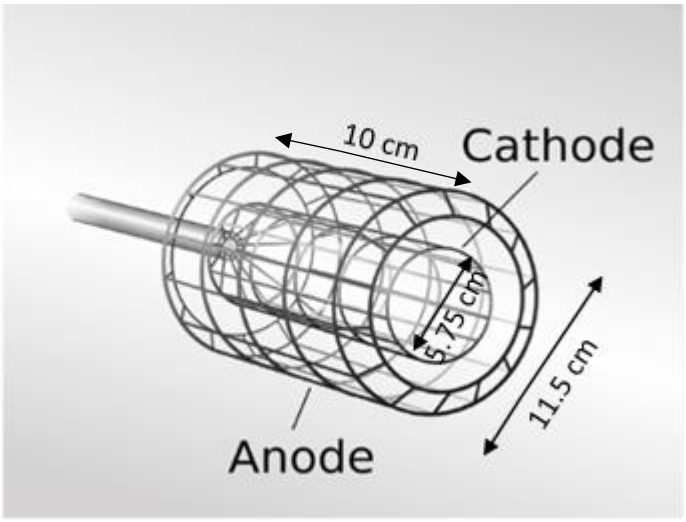

Fig 1-5

Schematic diagram for cylindrical TCD

The breakdown criterion is based on that to sustain the discharge, the charge particles lost in the discharge must be compensated by other process such as ionization and secondary electron emission (see section 3.4).

1.7 Thesis Outline

The thesis is a 2D simulation model for breakdown of cylindrical TCD, it consists of six chapters, the model was implemented from scratch, the first two chapters expounds the background theory of the model, all the equations used in the model are explained in chapter two, chapter three explain the model itself, chapter four present, and discusses the results of the model for specific configuration to compared to experimental work done within the group, chapter five discusses simulation of alternative configuration and the effects of the changes in geometries, chapter six provide summary and conclusions.

Chapter 2

Simulation Theoretical Foundations

Although the operating phase of Inertial Electrostatic Confinement devices (IEC) has been studied since the early fifties of the last century, the phase prior this, and which has a great influence on it, i.e. the ignition or breakdown phase of such devices, is not yet covered such how the breakdown evolved, what are the effective mechanisms, operating voltage ...etc. A good description of this phase will reveal the mechanism of the plasma formation and underlying physics, which will provide keys to understand or even control the next stage. An effective way to achieve this goal is through mathematical modelling, and because it has not been carried out before, this is the aim of this work. In this chapter the foundations of the particle approach will be explained, in details. A brief description for the regime to be simulated will be given at the end of this chapter as well.

2.1 Particle Tracking (Particle Mover)

In the particle approach the trajectory of a particle is tracked by applying Newton's laws of motion. The two first-order differential to be solved for each particle are

$$m\,\frac{d\mathbf{v}}{dt} = \mathbf{F} \qquad 2\text{-}1$$

$$\frac{d\mathbf{x}}{dt} = \mathbf{v} \qquad 2\text{-}2$$

here **x** is displacement vector. Treating these equations by finite difference method leads to

2-3

$$m\frac{\mathbf{v}_{\text{new}}-\mathbf{v}_{\text{old}}}{\Delta t}=\mathbf{F}$$

$$\frac{\mathbf{x}_{\text{new}}-\mathbf{x}_{\text{old}}}{\Delta t}=\mathbf{v}_{\text{new}} \qquad 2\text{-}4$$

For a charged particle moving in electric field **E** the equation of motion become

$$\mathbf{v}_{\text{t}+\Delta\text{t}}=\mathbf{v}_{\text{t}}+\frac{q\mathbf{E}}{\Delta t} \qquad 2\text{-}5$$

$$\mathbf{x}_{\text{t}+\Delta\text{t}}=\mathbf{x}_{\text{t}}+\mathbf{v}_{\text{t}+\Delta\text{t}}\Delta t \qquad 2\text{-}6$$

For simplicity one dimension will be considered. The same equation will be valid for other coordinates, and from now on $v_{t+\Delta t}$ and $v_{t-\Delta t}$ will be written as v_{t+1} and v_{t-1} respectively. This is first order accurate, and a comparison between this method and the analytical solution for simple harmonic oscillation shows a divergence as the number of time step increased, i.e. instability. An alternative method proposed using the velocity in the middle of the time step, instead of the velocity of the beginning of it. This is called time centering [20,21], this is done by pushing the initial velocity $v(0)$ at $t = 0$ of the particle a half time step $\Delta t/2$ back to $v(-\Delta t/2)$, using the force (electric field) calculated at $t = 0$ only once at the beginning of the simulation. This is also called the leap-frog method, Fig. (2-1) shows a sketch of leap-frog method and time centering

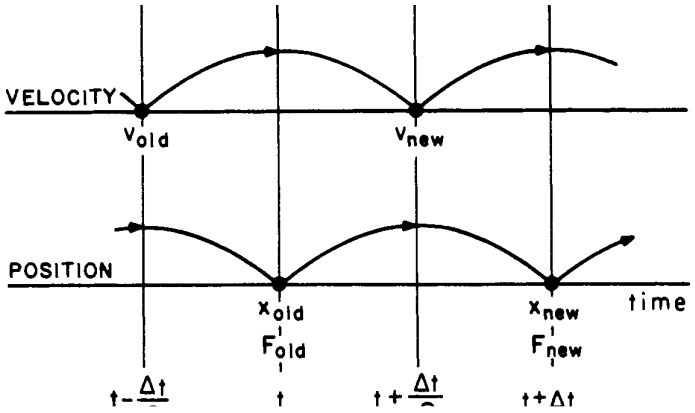

Fig. 2-1

Sketch of leap-frog integration method showing time centering of F while advancing v, and while advancing x [20]

According to equations (2-6) the leap-frog for $v_{t-\Delta t/2}$ and $v_{t+\Delta t/2}$ will be

$$\mathbf{v}_{t-\Delta t/2} = \frac{\mathbf{x}_t - \mathbf{x}_{t-\Delta t}}{\Delta t} \ , \mathbf{v}_{t+\Delta t} = \frac{\mathbf{x}_{t+\Delta t} - \mathbf{x}_t}{\Delta t} \qquad 2\text{-}7$$

So the computation cycle starts with a position x_t and velocity $v_{t-\Delta t/2}$, then calculate the electric field for that position. This is then used to calculate new velocity $v_{t+\Delta t/2}$, which is applied to determine new position x_{t+1} , then go to a new cycle and so on.

The leap-frog has error, which vanishes as $\Delta t \to 0$ [20]. And since it is simple (easy to understand and implement) and also surprisingly accurate, so it is used in this work.

2.2 Field Solver

In Monte Carlo models, the physical continuous domain is divided into a grid, a mathematical construct that makes it possible to solve differential equations numerically through the finite difference method (FDM). The Poisson equation for electrostatic potential, ϕ, FDM writes the differential equation of the potential in discrete intervals, e.g. by using a Taylor series expansion, first in the forward direction [18,20,22]

$$\varphi(x + \Delta x) = \varphi(x) + \Delta x \frac{\partial \varphi}{\partial x} + \frac{(\Delta x)^2}{2} \frac{\partial^2 \varphi}{\partial x^2} + \cdots \qquad 2\text{-}8$$

and then the same is done in the backward direction

$$\varphi(x - \Delta x) = \varphi(x) - \Delta x \frac{\partial \varphi}{\partial x} + \frac{(\Delta x)^2}{2} \frac{\partial^2 \varphi}{\partial x^2} + \cdots \qquad 2\text{-}9$$

By neglecting higher orders, the second derivative can be found approximately via combining equations (2-8) and (2-9); this known as central differencing and it is second order accurate [20]

$$\frac{\partial^2 \varphi}{\partial x^2} = \frac{\varphi(x+\Delta x) - 2\varphi(x) + \varphi(x-\Delta x)}{(\Delta x)^2} \qquad 2\text{-}10$$

In FDM, solutions are known only at the grid points, for clarity we rewrite equation (2-10) by labelling the grid point at position *x* with the grid number *j*

$$\frac{\partial^2 \varphi}{\partial x^2} = \frac{\varphi_{j+1} - 2\varphi_j + \varphi_{j-1}}{(\Delta x)^2} = -\frac{\rho_j}{\epsilon_o} \qquad 2\text{-}11$$

where ρ_j is the charge density at point *j*.

The value of the potential ϕ_j at point grid *j* depend on the potential at the grid points next to *j* on both sides, i.e. *j*+1 and *j*-1. If there are *N* grid points, therefore there are *N* equations, and in order to solve for the potential ϕ for each point, we must specify the boundary conditions. This is done by setting the potential at the point where the electrodes or the wall are existing to the desired potential (Dirichlet boundary conditions), i.e. if *i* is the point at the boundary the coefficient multiplied by ϕ_i is equal to 1 and the other coefficient is equal to 0 at that point (ϕ_i = the boundary potential). The charge density, ρ_j , is evaluated at each grid point by calculating the contribution of the charged particles in the domain through weighting, which will be explained later in this section.

Writing equation (2-11) in matrix form

$$\begin{bmatrix} B_1 & C_1 & & & & \\ A_2 & B_2 & C_2 & & & \\ & A_3 & B_3 & C_3 & & \\ & & \ddots & \ddots & \ddots & \\ & & & A_{N-1} & B_{N-1} & C_{N-1} \\ & & & & A_N & B_N \end{bmatrix} \begin{bmatrix} \phi_1 \\ \phi_2 \\ \phi_3 \\ \vdots \\ \phi_{N-1} \\ \phi_N \end{bmatrix} = \frac{(\Delta x)^2}{\epsilon_o} \begin{bmatrix} \rho_1 \\ \rho_2 \\ \rho_3 \\ \vdots \\ \rho_{N-1} \\ \rho_N \end{bmatrix} \qquad 2\text{-}12$$

Where *A* = 1, *B* = -2, *C* = 1, here Δx is the distance between two successive grid points. This is a tridiagonal matrix; a matrix with non-zero elements only on the diagonal and one another

on both sides; there are many solvers for this kind of matrices, e.g. the tridag solver from Numerical Recipes [34].

To calculate the charge density ρ_j on each grid point, the particles are distributed in the domain randomly, and the influence of charge on the grid points will be taken, by calculating the contribution of each particle only on the nearby point of the gird, i.e. the point of the cell the particle is located in. This is called cloud in cell (CIC). If a particle of position x and charge q is in a cell between x_j and x_{j+1}, it contributes to x_j a charge of $q(1 - (x - x_j))$ and to x_{j+1} a charge $q(x - x_j)$. By summing the effect of all particles on a grid point, the charge density at that point is calculated, this process is called weighting [18,22].

Fig. (2-2) shows the contribution of a charged particle on two dimensional grid points in CIC, the area of the rectangles is proportional to the fraction of charge contribution on each point, each rectangle has the same colour as the grid point it is correlated with.

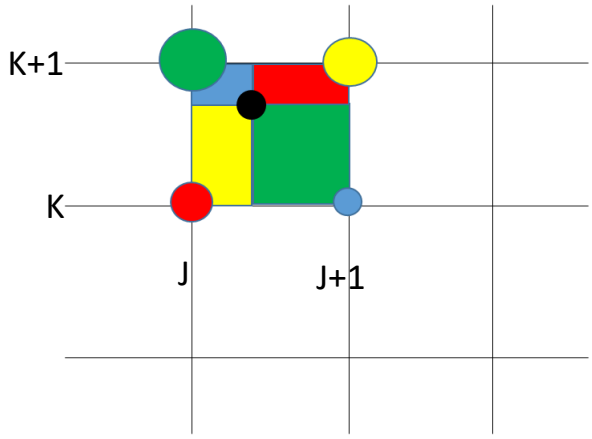

Fig. 2-2
A representation of two dimensional grid. The particle (black circle) moves through the domain and set charge on the around grid points of the cell it is in.

The charge density at each point of the grid because of this particle will be

$$\rho_{j,k} = \rho_c \frac{(\Delta x - x)(\Delta y - y)}{\Delta x \Delta y} \qquad 2\text{-}13$$

$$\rho_{\mathrm{j+1,k}} = \rho_{\mathrm{c}} \frac{x(\Delta y - y)}{\Delta x \Delta y} \quad \text{2-14}$$

$$\rho_{\mathrm{j+1,k+1}} = \rho_{\mathrm{c}} \frac{xy}{\Delta x \Delta y} \quad \text{2-15}$$

$$\rho_{\mathrm{j,k+1}} = \rho_{\mathrm{c}} \frac{x(\Delta y - y)}{\Delta x \Delta y} \quad \text{2-16}$$

Where *x, y* are coordinates of the particle in the domain, ρ_c is the charge density of the particle, *j, k, j+*1*, k+*1 are labels of the grid points [20]. The Poisson equation becomes

$$\frac{(\varphi_{\mathrm{j+1}} - 2\varphi_{\mathrm{j}} + \varphi_{\mathrm{j-1}})_{\mathrm{k}}}{(\Delta x)^2} + \frac{\varphi_{\mathrm{k+1}} - 2\varphi_k + \varphi_{\mathrm{k-1}})_{\mathrm{j}}}{(\Delta y)^2} = -\frac{\rho_{\mathrm{j,k}}}{\epsilon_{\mathrm{o}}} \quad \text{2-17}$$

After specifying the boundary conditions, this set of equations is then solved for all potential $\varphi_{j,k}$.

During the breakdown phase the space charge is negligible, so zero charge density assumed, and the distribution of the potential within the domain is considered to be only due to the applied voltage. The potential therefore needs to be calculated once only.

The electric field at each point is obtained from the potential values by using

$$\mathbf{E} = -\nabla\varphi \quad \text{2-18}$$

Which in one dimension becomes

$$E = -\frac{\partial\varphi}{\partial x} \quad \text{2-19}$$

By using the same logic of central difference method explained before this becomes

$$E_{\mathrm{j}} = -\frac{\varphi_{\mathrm{j+1}} - \varphi_{\mathrm{j-1}}}{2\Delta x} \quad \text{2-20}$$

The central differencing cannot be applied at the boundaries, because there are no neighbouring grid points, so either the forward or the backward difference can be used, that is

$$E_1 = -\frac{\varphi_2 - \varphi_1}{\Delta x} \qquad 2\text{-}21$$

$$E_{\mathrm{N}} = -\frac{\varphi_{\mathrm{N}} - \varphi_{\mathrm{N}-1}}{\Delta x} \qquad 2\text{-}22$$

But these are only a first order accurate, which affects the accuracy of the whole solution.

This can be improved to second order accuracy by using a further Taylor expansion

$$\varphi(x + 2\Delta x) = \varphi(x) + 2\Delta x \frac{\partial \varphi}{\partial x} + \frac{(2\Delta x)^2}{2} \frac{\partial^2 \varphi}{\partial x^2} + \cdots \qquad 2\text{-}23$$

By combining equations (2-8), (2-19), and (2-23) we get

$$E_1 = \frac{3\varphi_1 - \varphi_3 + 4\varphi_2}{2\Delta x} \qquad 2\text{-}24$$

Applying exactly the same procedure but in backwards direction gives

$$E_{\mathrm{N}} = \frac{-3\varphi_{\mathrm{N}} + \varphi_{\mathrm{N}-2} - 4\varphi_{\mathrm{N}-1}}{2\Delta x} \qquad 2\text{-}25$$

Now to obtain the electric field in two dimensions, equation (2-18) is used with the usual two-point difference form [20,21,35]; for E_x, as sketched in Fig. (2-3)

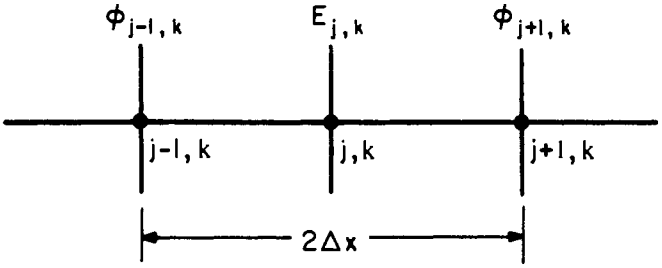

Fig. 2-3
Location of $E_{j,k}$ with relation to $\varphi_{j,k}$ [20]

$$(E_{\mathrm{x}})_{\mathrm{j,k}} = -\frac{(\varphi_{\mathrm{j}+1} - \varphi_{\mathrm{j}-1})_{\mathrm{k}}}{2\Delta x} \qquad 2\text{-}26$$

By using similar differencing for E_y

$$(E_{\mathrm{y}})_{\mathrm{j,k}} = -\frac{(\varphi_{\mathrm{k}+1} - \varphi_{\mathrm{k}-1})_{\mathrm{j}}}{2\Delta x} \qquad 2\text{-}27$$

For the points at the edges of the domain, formulas similar to equations (2-24) and (2-25) will be used inside the brackets of equations (2-26) and (2-27) instead of two-point difference. These calculated values of electric field E_x and E_y will be used to consider the force components F_x and F_y.

2.3 Collision

In the gaseous state the inter-molecular forces are negligible and the dominant processes are collisions (hard sphere collisions), through which the gaseous properties can be described, e.g. pressure, temperature, heat transfer…etc. Before breakdown the system is still in a gas state, and collisions are very important factor to take into account in a breakdown simulation. Because charged particles in this stage are extremely few, the collisions that will be focused on are particle-neutral collisions, that could effect and lead to breakdown. Collisional phenomena can be broadly divided into two types: elastic and inelastic. In an elastic collision the particles involved will retain their identity with conversation of energy and momentum, i.e. there are no changes in internal states of the collided particles and there is neither creation nor annihilation. In inelastic collisions however the internal states of some or all of the collided particles are changed and particles may be created or destroyed. A charged particle may recombine with another to form a neutral or may attach itself with a neutral to form a heavier particle, and ionization or excitation process can take place as well [36,37].

The collisions considered in this work are as mentioned where are these that can have influence on the ignition of the plasma, i.e. electron-neutral, ion-neutral and fast neutral-neutral collisions; elastic collisions, charge exchange collisions. (a special kind of elastic collision where the incident fast ion pick up an electron from a slow neutral, becoming a fast

atom and leaving a slow ion behind [18,23]), inelastic excitation collisions (where the collided energized particle, electron, ion or fast neutral give part of its energy to a ground state electron, causing it to move to a higher energy level within the involved neutral, leaving an excited neutral), and ionization collisions (also inelastic), where the collided particle affords an electron the energy required to escape from the collided neutral, creating a pair of charged particles [36,37].

2.3.1 Collision Theory

If two particles m_1 m_2 collide, then momentum must be conserved, i.e. the total momentum before and after the collision is equal. If the collision is an elastic collision the total energy of the particles before and after the collision will be equal as well. If both particles have the same mass and the target particle m_2 is at rest, the two particles will emerge from the collision at right angle to each other [38].

Fig. (2-4) illustrates this collision. The incident particle scatters along the tangent line to the point of collision, and the other particle scatters parallel to the line connecting the centres of the two colliding particles (collision axis) [39,40].

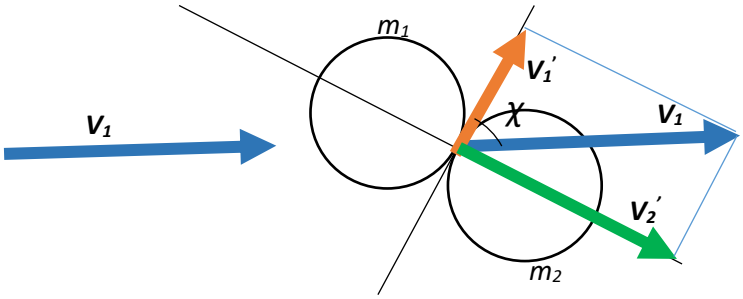

Fig. 2-4

Collision of two equal mass particles. One of them was initially at rest

where χ is the scattering angle, $\mathbf{v_1}$ is the incident velocity $\mathbf{v}_1$ of particle m_1, and $\mathbf{v_1}'$, $\mathbf{v_2}'$ are the particles velocity after collision. From the Fig. (2-4) the scattered velocity $\mathbf{v}_1'$ and the incident velocity $\mathbf{v}_1$ of particle m_1 are related by

$$\mathbf{v_1'} = \mathbf{v_1} cos\chi \qquad 2\text{-}28$$

The scattered particle energy E_s will be related to the incident particle energy E_i by

$$E_s = E_i cos^2\chi \qquad 2\text{-}29$$

The rest of the energy will go to the other particle.

2.3.2 Collision Simulation

2.3.2.1 Direct Monte Carlo

Since the number of particles in a gas is large and the collisions occur frequently and randomly, simulation of collisions is addressed by using a statistical technique called Monte Carlo, based on the collision probability, i.e. the chance of a particle traveling in the domain during a time-step Δt to suffer a collision. This is obviously related to the average distance that the particle can travel before suffering a collision, i.e. mean free path (mfp) λ, since $\lambda = 1/n\sigma$, where σ is the cross section (m^2) and n is the particle density (particle/m^3). The probability of collision is given by

$$P = 1 - \exp(-n\sigma_T(E)v\Delta t) \qquad 2\text{-}30$$

where $\sigma_T(E)$ is the total cross section as a function of relative energy between the colliding particles, i.e. the sum of all considered collisions, and v is the relative velocity. This probability is then compared with a uniform random number R_1 between 0 and 1. If $R_1 > P$, no collision

occurs and simulation continues without any effect, if $R_1 \leq P$, a collision is assumed, and the next step is to decide the type of this collision. This is done by assuming each type k of collision a probability equal to its contribution in the total cross section, i.e. σ_k/σ_T , these are distributed from 0 to 1, i.e. σ_1/σ_T , $\sigma_1+\sigma_2/\sigma_T$, . . . , and $\sigma_1+\sigma_2+\ldots+\sigma_n/\sigma_T$, and the fall of another uniform random number R_2 from 0 to 1 will decide which collision occurred. Fig. (2-5) illustrates this

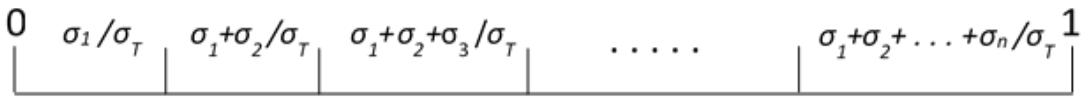

Fig. 2-5

Distribution of each type of collision according to its contribution in total

This is called Direct Monte Carlo (DMC), where all cross sections and total cross section obtained for each collision test [18,22].

2.3.2.2 Null Collision

Skullerud [25,41] proposed the null collision, by assuming an artificial probability P_{null} just larger than the maximum probability P_{max} , which can be obtained from the set of values of the assumed collisions, this P_{null} compared to a uniform random number R_1 0 to 1 instead of P_T in DMC; if it is less than R_1 no collision occurs. Since it is constant during the simulation, there is no need to obtain the total cross section, which is a significant saving in the simulation process, especially since P_{null} is typically of order 10^{-2}. If $P_{null} > R_1$, then the total cross section is calculated and if it is less than R_1 a null collision assumed, i.e. no effect; this justifies the name null collision.

2.3.2.3 Nanbu Collision Model

Nanbu [26,27] proposed a model based on dividing a line representing one into equal partitions, with each partition representing a type of collision, i.e. number of partition equal number of collisions under consideration. The right side of each partition is the collision probability, and the left side of this partition is non collision probability of that type, is based on

$$1 = (1 - P) + P = \sum_{i=1}^{K} [\left(\frac{1}{K} - P_{\mathrm{i}}\right) + P_{\mathrm{i}}] \qquad 2\text{-}31$$

Fig. (2-6) illustrate the structure of equation (2-30)

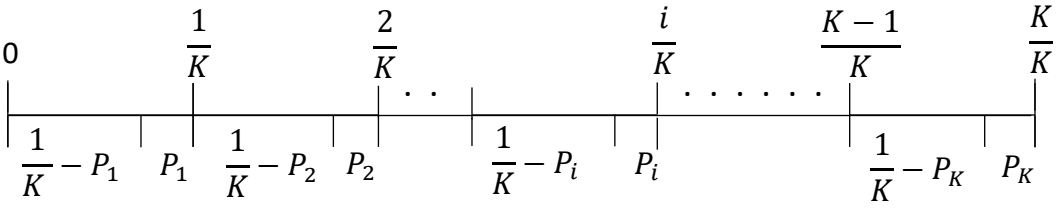

Fig. 2-6

Collision probability distributed on K type of collision (partition)

If *R* is a uniform random number 0 to 1, the integer of (1 + *KR*) will be the number of the partition *R* lies on, let it be *i.* If *R* lies on the left side of the *i* interval, i.e. $R < (i/K)-P_i$ no collision is assumed, otherwise *R* lies on the right side of the partition, i.e. $R \geq (i/K)-P_i$, the *i*th collision is assumed. Judgment of type and occurrence is therefore made at the same time with the same *R*. The time-step Δt should satisfy $P_i < 1/K$ for all intervals and for any energy [26,27]. This model will be adopted, because its efficiency and computational saving is quite significant.

This work will look at helium to compare to experimental work which has been done for helium and argon, and to literature which are available for helium in TCD.

As discussed above, cross sections are a crucial element in any Monte Carlo collision model. For this reason, Liang Xu et al. [24] discussed and compared different experimental, and theoretical data sets of cross sections in the literature which is of interest for this work. They chose an optimum set of cross sections and gave reasons for their selection, therefore these sets will be adopted in this work. While the reaction 2, 6 and 9 are implanted in the simulation, the metastable neutrals will not be followed [23,24], because the number of these during the ignition phase are very few (maximum in total less than five times the number of total ionization events) and their lifetime (loose its extra energy as heat and be in ground stat) is very short (in range of Nano second), so the probability to preform ionization collision is negligible. Table (2-1) list the physical processes implemented in the model with the recommended data set for that process, and these corresponding cross sections are plotted in Fig. (2-7) [24]

Table 2-1

Physical processes implanted in the model with the recommended data set for that process

No.	Reaction	Reaction type	Cross section source adopted
1	$e + He \longrightarrow e + He$	Elastic	39
2	$e + He \longrightarrow e + He^{*}$	Excitation	40
3	$e + He \longrightarrow 2e + He^{+}$	ionization	40
4	$He^{+} + He \longrightarrow He^{+} + He_{(f)}$	Elastic	41
5	$He^{+} + He \longrightarrow He_{f} + He^{+}$	Charge exchange	42
6	$He^{+} + He \longrightarrow He^{+} + He^{*}$	Excitation	43
7	$He^{+} + He \longrightarrow 2He^{+} + e$	ionization	44
8	$He_{f} + He \longrightarrow He_{f} + He_{(f)}$	Elastic	45
9	$He_{f} + He \longrightarrow He_{f} + He^{*}$	Excitation	46
10	$He_{f} + He \longrightarrow He_{f} + He^{+} + e$	ionization	47,48

The subscript (f) indicates a possibility for an atom to be produced as a fast neutral, while subscript f without brackets indicates a fast neutral [21]

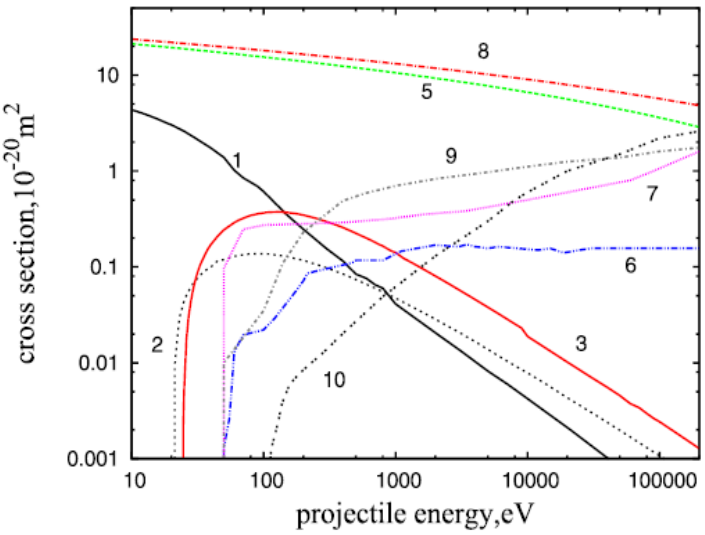

Fig. 2-7

Cross sections for collisions types as in table (2-1) (Matching numbers between Fig. and table) [24]

The ion-neutral elastic cross sections (4 in table) data were taken from Cramer and Simons [44], and were fitted to a functional form [23]

$$\sigma(E) = (7.04 - 0.62\ln(E))^2 - (5.2 - 0.302\ln(E))^2 \qquad 2\text{-}32$$

Where E in eV and σ in cm^{-2}. This is applicable for $E \leq 325\ eV$, because higher energies the charge exchange collisions dominate the pure elastic collisions, so that these can be neglected compared to charge exchange, and the formula (2-32) fails and gives negative results.

2.3.2.4 Treatment of Collisions

After deciding there is a collision and its type, consideration of its effect must be determined. First the types of collisions that will be dealt with for each particle are specified; as mentioned before the collisions under consideration are elastic, excitation, ionization for all particles (ions, electrons and fast neutrals with neutrals), and charge-exchange for ions. A

neutral is considered as fast neutral if it has the ability to perform an ionization collision, i.e. its energy equal or exceed the threshold ionization energy.

The simplest collisions to simulate are ion-neutral charge-exchange collisions. The collision is reduced to an exchange of velocities, i.e. the ion becomes a neutral (mostly a fast neutral) and the neutral becomes a slow ion [18,22,41].

The collisions for the ions and fast neutrals (elastic, excitation and ionization) are treated the same way, and they are all assumed to be isotropic in the plane perpendicular to the line connecting the center of the two collided particles [18,22].

In elastic collisions the problem is reduced to that discussed in (2.3.1), i.e. an incident particle on a target particle at rest, that is done by using a frame of reference maintained on the center of the target particle, i.e. using the relative energy E_r instead of E_i for the incident particle in equation (2-29)

$$E_s = E_r cos^2\chi \qquad 2\text{-}33$$

A uniform random number R 0 to 1 assumed so that

$$\cos\chi = \sqrt{1-R} \qquad 2\text{-}34$$

Equation (2-33) become

$$E_s = E_r(1-R) \qquad 2\text{-}35$$

And the energy of the neutral after collision in this frame E_n is

$$E_n = E_r R \qquad 2\text{-}36$$

After calculating the velocity in this frame for the ion and the neutral scattered energy, then the original frame (lab frame) is returned to by adding the velocity of the neutral to these calculated velocities.

The excitation and ionization collisions are treated in the same way but eliminating the excitation or ionization energy (according to the collision assumed) from the relative energy, and use equations (2-35) and (2-36) [18,22]. In an ionization collision the created ion will have the neutral velocity and the created electron will be assumed to have zero born energy.

Now looking at electron collisions to determine the energy partitioning and then determine the scattering angle. For elastic collisions, and due to the large mass differences between the electron and the neutral atom, the electron only scatters in angle, neglecting energy loss. The scattering angle is given by the equation [18,41}

$$\chi = cos^{-1}\left(\frac{2 + E - (1+E)^{R}}{E}\right) \qquad 2\text{-}37$$

Where χ is the scattering angle of the electron and E is its energy, and R is uniform random number from 0 to 1.

For excitation collisions the specific energy levels of the atom are not considered. The loss of energy is chosen randomly between the first excitation level and either the incident electron energy or the ionization energy, whichever is smaller, i.e.

$$E_{exc} = E_{exc1} + (E_{min} - E_{exc1})R \qquad 2\text{-}38$$

Where R is a uniform random number 0 to 1, E_{exc} is the excited state assumed, E_{exc1} is the first excited state, and E_{min} is the smaller of ionization energy E_{ion} and incident energy E_{inc} [22].

In ionization collisions the energy of the scattered E_{sc} and created $E_{created}$ electrons are partitioned [18,22]

$$E_{created} = B\ tan\left(R\ tan^{-1}\left(\frac{E_{\text{inc}} - E_{\text{ion}}}{2B}\right)\right) \qquad 2\text{-}39$$

Where B is an experimental const. (= 15 eV [22] for He and = 10 eV [18] for Ar) and R is a uniform random number from 0 to 1, E_{ion} is the ionization energy and E_{inc} is the incident energy.

$$E_{sc} = E_{inc} - E_{ion} - E_{created} \quad (2\text{-}40)$$

The two electrons velocities are perpendicular to each other and lie in the same plane with velocity of the incident electron. The scattering angles $\chi_{created}$ and χ_{sc} (measured with respect to the direction of velocity of the incoming electron) are calculated from [18,22]

$$\chi_{created} = cos^{-1}\left(\frac{E_{created}}{E_{inc} - E_{ion}}\right) \quad (2\text{-}41)$$

$$\chi_{sc} = cos^{-1}\left(\frac{E_{sc}}{E_{inc} - E_{ion}}\right) \quad (2\text{-}42)$$

The new ion has the velocity of the neutral before collision [18,22].

2.4 Surface Effects

Surface effects refer to the interaction of energetic incident particles (ions, fast neutrals, and electrons) on the electrodes (cathode and anode) and the wall surfaces, which including reflection (backscattering), and secondary electron emission.

2.4.1 Secondary Electron Emission (SEE)

When a particle (ion, neutral, electron, and photon) strikes a surface, an electron can be emitted; this process is called secondary electron emission (SEE). The number or the probability of electrons emitted per incident particle is called the secondary electron emission coefficient or yield, γ. It is a function of the kind of incident particle, its energy, and the surface material [6].

Since the energy of the secondary emitted electron is very low (a few eV), the SEE at the wall and the anode will not be considered. This is because the electric field is very strong at the anode and these electrons will be reflected and recaptured, while at the wall the electric

field is very weak, so the emitted electrons only can collide elastically until lost, and hence have no effect on breakdown, this was checked by adding it to the simulation and see their effect. Also, due to the repulsive field at the cathode, no SEE by electron impact is predicted. Another important issue is that the SEE for clean surfaces in gas discharges is not applicable, due to the energetic ions and neutrals bombardment on the surface, which causes roughness and contamination by attached or implanted neutrals due to the impact. Therefore, only SEE by ions and fast neutrals at the cathode, as a dirty surface, will be considered.

The secondary electron ejection mechanism is explained by two mechanisms, namely potential ejection and kinetic ejection. The potential mechanism which acts through electromagnetic interaction, dominates for secondary electron emission (SEE) by slow ions, because it is independent of ion velocity, but for fast ions the kinetic mechanism which acts through mechanical interaction, dominates because it depends strongly on ion velocity. The potential mechanism cannot apply for the ground state neutrals. Generally, the kinetic ejection has a larger yield for contaminated surfaces than for clean surfaces. Therefore, on contaminated surfaces, it is believed that the electron ejection by neutrals is considered to be like that by ions above several hundred electron volts [52]. K. Kadota and Y. Kaneko [52] studied γ_n by He and Ar atoms on contaminated surfaces and compared with many literatures, they stated that the electron ejection they studied for γ_n is thought to be similar to the kinetic ejection by ions on the contaminated surfaces. Furthermore, they noticed that γ_n obtained for contaminated surfaces have much larger magnitudes and lower thresholds than those for clean surfaces, and also that γ_n on a contaminated surface appears to be independent of the properties of the metal itself. It appears that the ionization processes by collision or adhered molecules with the incident atoms are involved in this ejection mechanism, as suggested by Paetow and Walcher [53], and Berry [54]. This hypothesis is supported by the fact the measured γ_n curves resemble well the ionization cross section curves measured by Utterback [55], and Hayden and Utterback [50] in neutral-neutral collision

[52]. Accordingly, and because of the lack of available data for γ_n on stainless steel, this for fast neutrals will be assumed equal to γ_i taken from Szapiro et al. [30].

To simulate secondary electron emission (SEE), since γ is the probable SEE due to the impact of a particle of energy *E* on a surface, the integer part of $\gamma(E)$ (may be more than 1) is assumed definite SEE, and the fractional part of $\gamma(E)$ will be compared with a uniform random number *R* from 0 to 1. If *R* is less than $\gamma(E)$ another secondary electron (SE) is assumed. The direction of these SE, will be distributed with an angle from 0 to π with line tangent to the surface at the impact point, the first SE, will be simulated in a direction of π divided by the number of created SE multiplied by a uniform random number *R* from 0 to 1, the next is simulated by adding π divided by the number of created SE to the previous SE angle and so on, each SE has an energy of 2 eV.

2.4.2 Particle Reflection (Backscattering)

When a solid surface is bombarded with particles, some of the particles will be backscattered (reflected), while the remaining particles come to rest in the solid. These fractions and the energy of the reflected particles depend on the energy of the incident particles and their angle of incidence.

2.4.2.1 Ions and Atoms Reflection

The particle reflection coefficient R_N is defined as the number of all backscattered particles divided by the number N_0 of incident particles, and the energy reflection coefficient R_E is defined as the total energy of the reflected particles divided by the total energy of the incident particles.

It has long been recognized that the most important scaling operation is to replot R_N and R_E as a function of the Thomas-Fermi reduced energy ϵ defined as

$$\epsilon = 32.55 \frac{M_2}{M_1 + M_2} \frac{1}{Z_1 Z_2 (Z_1^{2/3} + Z_2^{2/3})^{1/2}} E_0 = \epsilon_L E_0 \quad 2\text{-}43$$

Where E_0 is the energy of incident particle in keV, Z_1, M_1 and Z_2, M_2 are the nuclear charge and mass of the incident particle and the target atoms, respectively [28,56,57]. In the case of helium upon stainless steel, ϵ_L = 0.1814.

Eckstein [57] proposed for R_N, R_E, an empirical formula for normal incidence of noble gases

$$R_N(R_E) = \frac{a_1 \epsilon^{a_2}}{1 + a_3 \epsilon^{a_4}} \quad 2\text{-}44$$

Where a_1, a_2, a_3, a_4, are constants specific to combination of incident particle and target atom. In the case of helium on stainless steel, for R_N $a1$ = 0.2179, a_2 = - 0.1976, a_3 = 0.148, a_4 = 1.621, and for R_E a_1 = 0.09012, a_2 = - 0.2536, a_3 = 0.2304, a_4 = 1.589.

The present work will take into account the ion reflection at the cathode and the fast neutral reflection at the electrodes and the wall, considering that ions are neutralized when they backscattered at the cathode, and that neutrals may be ionized when they reflected at the anode or the wall. This has been discussed by Thomas et al. [32], and Souda & Aono [33]; they found that there is a threshold energy for combination of the incident particle and the surface atom. In the case of helium on stainless steel, the threshold energy becoming ionized as they are reflected is 1000 eV. Because the limited available data for this process are values around 0.1, we will estimate one of this kind of reflection (ionized reflected particle) from each nine reflections from the wall and the anode carrying the threshold energy of the process.

To simulate the reflection of the ions and neutrals, R_N is the probability of the reflection of an incident particle, so it will be compared to uniform random number R from 0 to 1, if $R <$

R_N reflection will be assumed, otherwise no reflection assumed and the particle lost. If a reflection is assumed the energy of the reflected particle will be considered equal to average reflected energy

$$E_{av} = \frac{R_E}{R_N} E_0 \qquad 2\text{-}45$$

Where E_0 is the incident particle energy.

2.4.2.2 Electron Backscattering (BS)

The effect of electron backscattering on breakdown was noticed through the dependence of breakdown on the anode materials [24]. It is a function of incident angle α, the surface material atomic number Z, and, to lesser extent, the electron incident energy E_0. The probability of backscattering as a function of incident angle α and normal incident backscattering coefficient η_0, is approximated to a fitting formula [55]

$$\eta(\alpha) = \eta_0 exp(B(1 - \cos\alpha)) \qquad 2\text{-}46$$

Where B is a constant. According to available data from Gemoti et al.[31] and Darlington [58] for stainless steel (anode and wall in present work) the empirical values of B = 1.154 and η_0 = 0.28 [24] are used The angular distribution ϕ of the backscattered electron is assumed (a half isotropic in volume): $\cos\phi = \sqrt{R}$, where R is uniform random number from *0* to *1* [24], and the electron backscattered energy is assumed $0.85\ E_0$, where the peak of energy distribution of the backscattered electron is according to that reported by Darlington [58].

2.4.2.3 Reflection Consideration

To consider that the particle will strike the electrode, let the electrodes consist of *N* wires of radius r (cathode and anode), and the radial distance of the electrode wire from the center of the cathode be *R*, then the wires will be located at angles from the x-axis equal to $2\pi n/N$ where n integer from 0 to *N.* If the particle's radial distance from the origin (center) and its polar angle are R_p and ϕ_p respectively, then the particle is assumed to strike the wire (electrode), if $|R_p - R| < r$ and the absolute value of the remainder to the nearest integer of dividing ϕ_p by $2\pi/N$ is < half the angular width of the wire $\Delta\Theta$, Fig. (2-8) illustrate this

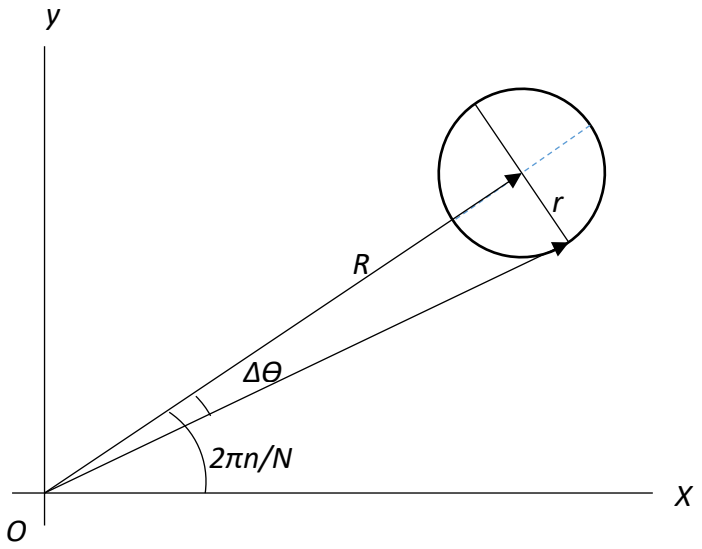

Fig. 2-8

Shows that particle hits the electrode wire if $R-r < R_p < R+r$ and $2\pi n/N - \Delta\Theta < \phi_p < 2\pi n/N+\Delta\Theta$ where R_p and ϕ_p are the polar coordinates of the particle

For the wall, it is clear if the x-axis or the y-axis of the particle exceeds that of the wall, it will be assumed to have hit the wall.

2.5 Present Simulated Cylindrical IEC

The IEC device simulated in the present work, consists of two concentric in phase cylindrical electrodes, of anode and cathode diameters 11.5 cm and 5.75 cm respectively. Each consists of 14 stainless steel wires of diameter 0.16 cm, maintained in a stainless steel cubic vessel of 30 cm a side. The wires are of equal angular separation $\pi/7$, and the first wire is located at zero angle with the positive x-axis.

Chapter 3
The Code

In this chapter, the code itself will be explained: its subroutines, its blocks, and how it is organized. Details will be given of what each block and subroutine contains, and also the way they are linked – their flow chart and role, and the flow chart of the main body of the code. Initial conditions will be described, and also the data files that are required for the code to run. Once the details of the code are made clear, the next concern is to show the validity of the code, first through tracking each species trajectory assuming free flight (no collision), then checking the collision block, and afterwards simulating a known case (breakdown between two parallel plates), applying the code in order to verify the results agree.

3.1 Data Files

In order to work, the code requires some data to be fed in. The sources of these files have been mentioned in chapter 2; these data files are of .txt type and stored in the same folder as the code file. These files are of different dimensions, and need to be declared and read. They include cross section data files – one file for each type of collision for each kind of species, and data files for secondary electron yield, electron backscattering, and electric field in x and y directions, i.e. E_x & E_y. The electric field files must be prepared in advance, which is the material of the next sub section.

3.1.1 Calculation of the Electric Potential and Field distribution

The potential distribution caused by applying voltage to the electrodes is calculated first, using the finite element method described in Section 2.2. As the number of charges involved in the breakdown process are relatively very small, i.e. space charge is negligible, it is assumed that the potential distribution is adequately represented by the effect of the

external voltage applied, i.e. this potential distribution is unaffected by the free charges generated during breakdown, and is hence valid throughout the breakdown calculation. Fig. (3-1) shows the potential distribution, where each electrode, anode and cathode, consists of 14 wires, with the wires aligned so that the anode and cathode wires lie at the same azimuthal position. The radii of the inner and outer grid circles are 2.875 cm and 5.75 cm respectively, and the electrodes are maintained in a cubic metal chamber with edges of 28.75 cm, which represents the grounded boundaries of the calculation. The calculation is carried out by dividing the domain into a 500 × 500 points grid; 250 squared cells from each side of the centre (origin) in both directions (*x & y)*, with each cell having 0.0575 cm sides, giving a spatial resolution of 0.0575 cm. The wire diameter is 0.16 cm. A plot of the calculated distribution is shown as Fig 3-1 using a scale for the case of 1kV applied voltage. The plot also shows the location of grid wires, which appear as small circles.

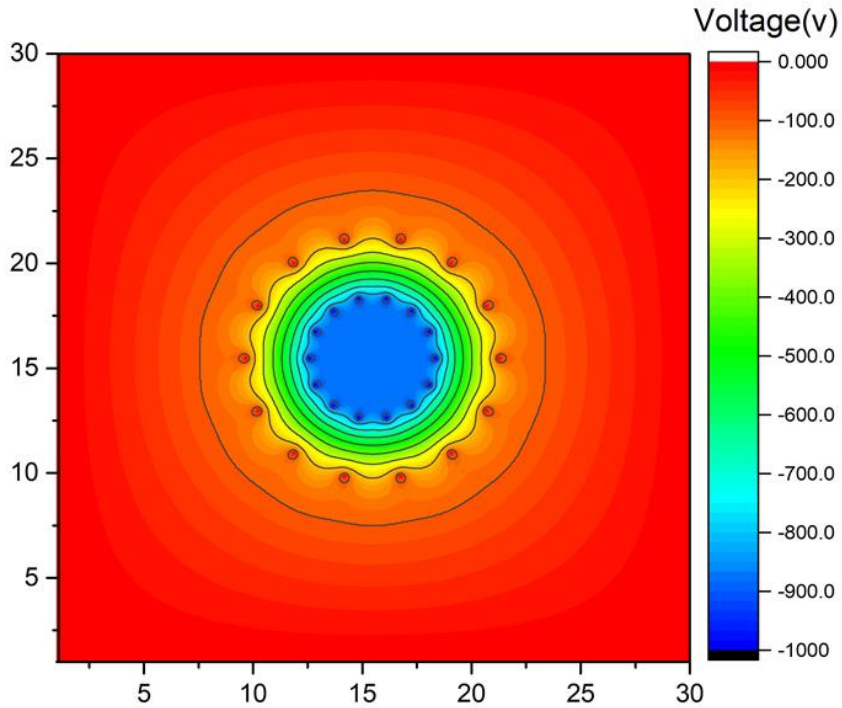

Fig 3-1

Potential Distribution for 14 wires aligned electrodes, 1 kV applied voltage

The 501 × 501 potential matrix is used to calculate the *x & y* components of the electric field E_x, E_y according to the equations given in section (2.2). The results are stored in two .txt type data files, one for each.

Even though the potential scale is only shown crudely in Fig. (3-1), the general features of the distribution are shown clearly. These main features can be summarized as follow:

- The region with the strongest gradient in field lies between the grid electrodes, as expected.
- The central region has a relatively flat potential, meaning that a large proportion of the central region can be considered field free.
- The effect of the electrode apertures can be seen, with the potential distribution being highly structured around the wires.
- A non-zero potential region exists between the outer grid and the chamber walls.

The details of the potential and field distribution depend strongly upon the geometry of the grid electrodes. However, these features outlined above, are generally true for this configuration, and will be useful when the performance of separate elements of the code is considered later in this chapter in section (3.2.1).

The electric field in the data files is known for the grid points, but a particle's position can be anywhere in the domain. The electric field must therefore be found in that position, and so first the grid cell that this position lies in is determined, then the electric field for the points in between the grid points will be found. The interpolated values will be assumed to lie on the straight line connecting consecutive grid points. This interpolation choice was made as a compromise between acceptable accuracy and computational expense, and so this will be applied in the code for all other data files.

3.2 Code Subroutines

The code contains subroutines called by the main code, that execute their function before returning to the main code. They can be classified into three blocks according to their function in the code, the read and calculate function block, the collision block (these will be explained in following subsections), and a subroutine that samples velocities for particles from a Maxwellian-distribution, since the particles are assumed to be in thermal equilibrium at the beginning of the simulation. This is done by working directly with a uniform set of random numbers, *R1, R2, . . . , RM,* between *0* and *1*, generating a normal (Maxwellian, Gaussian) distribution in

$$v_M = v_{th}\left(\sum_{i=1}^{M} R_i - \frac{M}{2}\right)\left(\frac{M}{12}\right)^{-\frac{1}{2}} \qquad 3\text{-}1$$

where v_M, v_{th}, are velocity from Maxwellian-distribution and thermal velocity respectively, and $v_M < v_{max} = v_{th}\sqrt{3M}$ [20].

3.2.1 Read & Calculate Functions Block

This block contains subroutines, one for each data file to be read, that stores it in an array declared – naming and reserving suitable memory size – previously in the block. These stored data will be linked to another function in the block, that calculates the interpolated values for values that don't exist in the data file, by using the same idea explained in (3.1.1) for electric field. These functions will respond to the main code call, calculate the desired value, and return it to the main code. Fig. (3-2) illustrates the flow chart of these 'read and calculate' functions block.

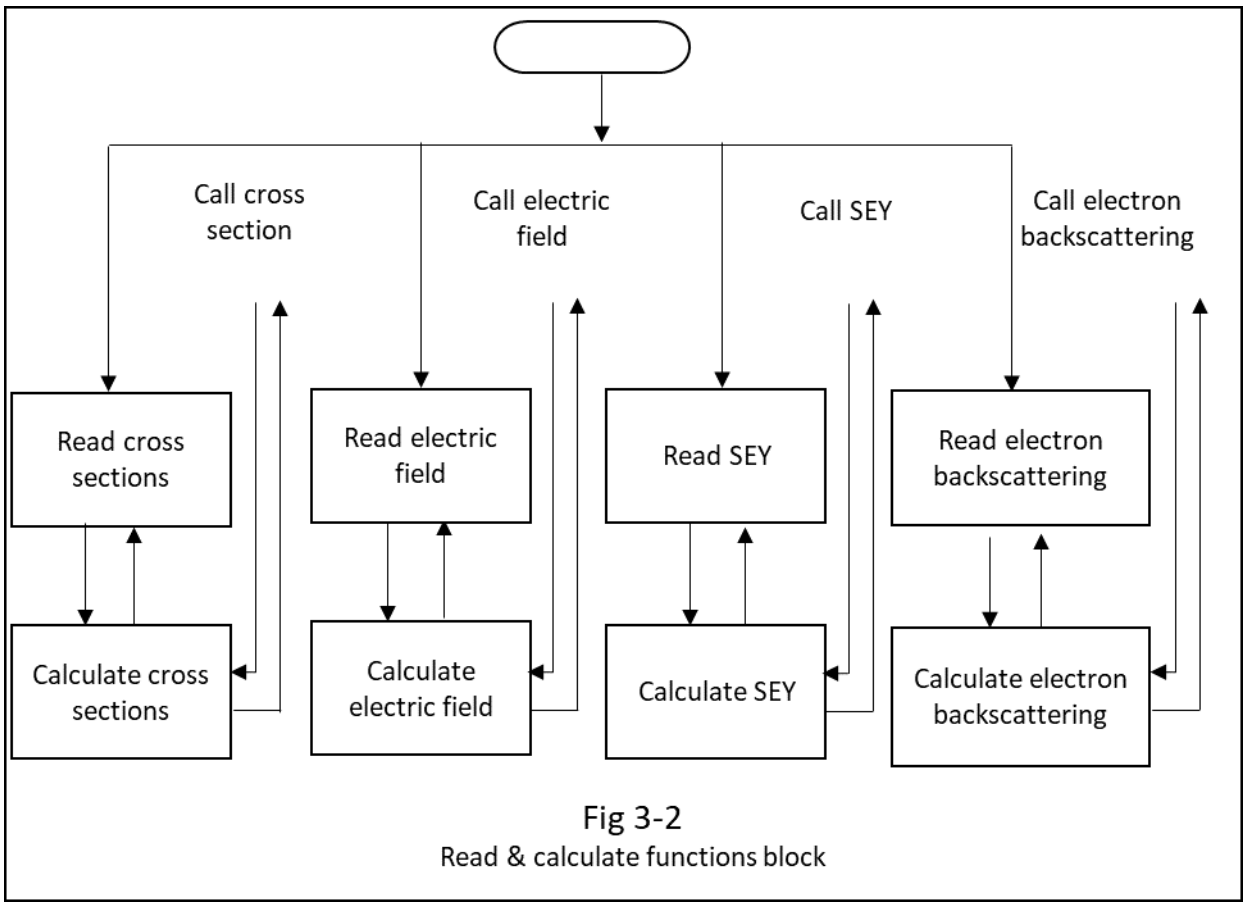

Fig 3-2
Read & calculate functions block

3.2.2 Collision Block

The main function of this block is to consider whether a collision has occurred or not, and if it has, the effect of this collision. It starts with first calculating the relative energy between the incident and target particles, then the kind of collision will be considered. These two factors are then fed to the cross section calculation functions, and accordingly the probability of that collision will be calculated. By comparing this probability with the same random number used to resolve the type of collision, the collision occurrence is then decided, and the effect of a collision will be resolved. If no collision occurs then there is no effect, and the code returns to the main program. Fig. (3-3) presents the flow chart of this block.

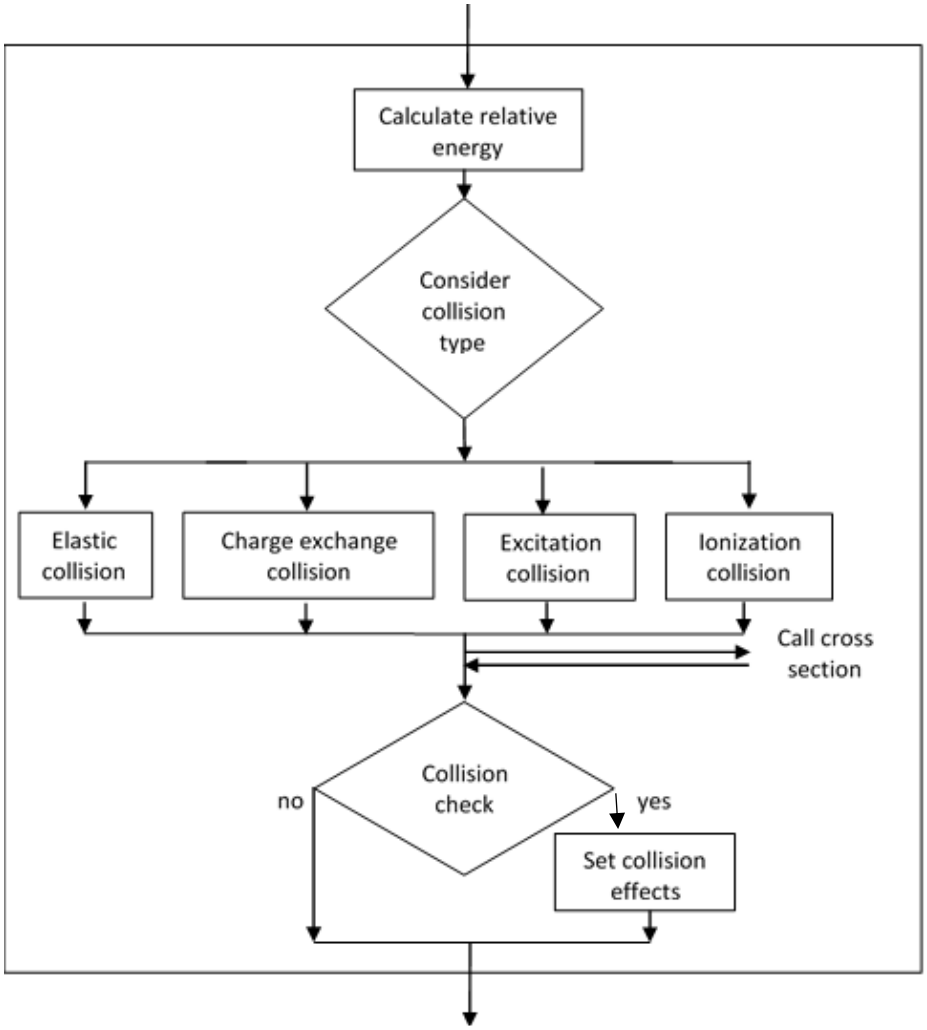

Fig. 3-3

Collision block for ions, other particles are similar except no charge exchange

3.3 Main Code

The main part of the code starts by setting the initial conditions, temperature (set to 300K, room temperature), pressure, applied voltage, time-step (= 10^{-11} sec), and a duration of 10^{6} time-steps, i.e. simulation time is 10^{-5} sec. When the time-step is reduced, the statistical error is also generally reduced but at greater computational expense, so the time-step was chosen in a way that the particles will travel an acceptable distance in one time-step, and the simulation time was chosen so that it is enough for the simulation to be almost stabilized. The same logic is applied in choosing one hundred ions and electrons positioned randomly – not too few, because then the error will be significant, and not too large, to avoid high

computational cost. Ions are distributed near the wall (r_i = 14.0 cm), and electrons around the cathode exterior (r_e = 2.95 cm). The velocities of these particles are sampled by calling the Maxwellian distribution function. The information for each particle is dealt with by using vectors, using dynamic arrays in c^{++} with the ability to resize automatically when an element is inserted or deleted. Their storage is handled automatically by the container, so creating and deleting particles can be treated smoothly. Time centring to leap-frog the particles, i.e. half time-step back is setup. After that the simulation time loop starts, which contains three independent loops, for ions, electrons and fast neutrals. Each one of these will loop on all the available particles of that kind at the time-step in action. Each particle loop includes the field solver (except for the fast neutrals), the particle mover, and a check to see if the particle hit the boundaries (wall or electrodes). If this happens, the possibility to be backscattered is evaluated, and also that for secondary electron emission if the cathode is hit. If secondary electrons are created and/or the particle is backscattered then, position and velocity x, y, v_x, and v_y, are set accordingly otherwise the particle is deleted. Then the collision check block runs, which evaluates the possibility and kind of collision, and if yes the effect of that collision. The same loop is run for all particles at the same time-step, and any particle created or deleted will take effect in the next time-step. Fig. (3-4) shows the flow chart of the particle loop block.

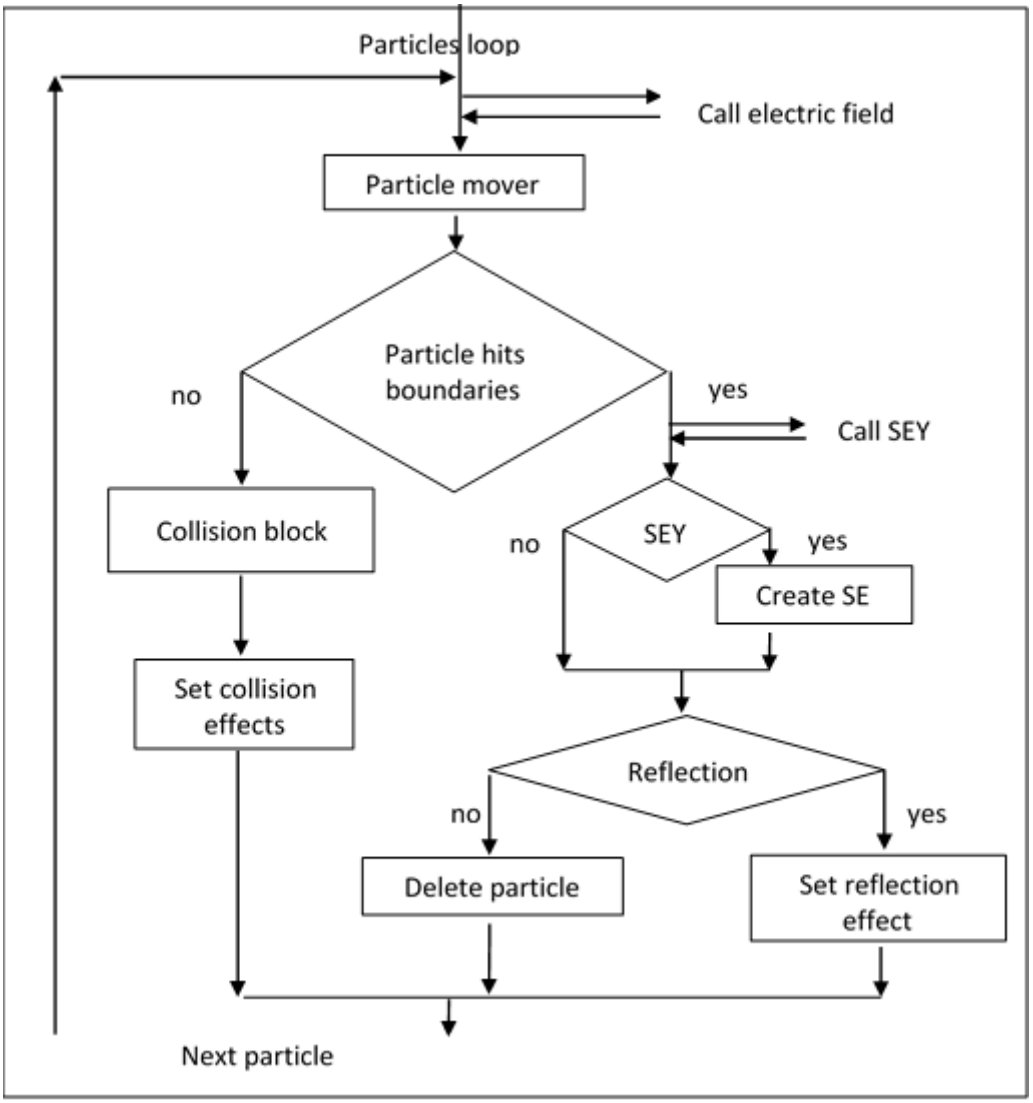

Fig. 3-4
Particle loop

When the particle loops are completed for that time-step, the next time-step starts, until the desired simulation time is reached. Fig. (3-5) shows the flow chart of the main part of the code. The information for each species is stored during the time-steps into two output files, one for events, i.e. number of collisions, reflections, creating etc., and a second for space and velocity. Another output file logs a record for events for all particles; the difference between this file and the first one is that, this file records the space and velocity and the kind of event only when it happens.

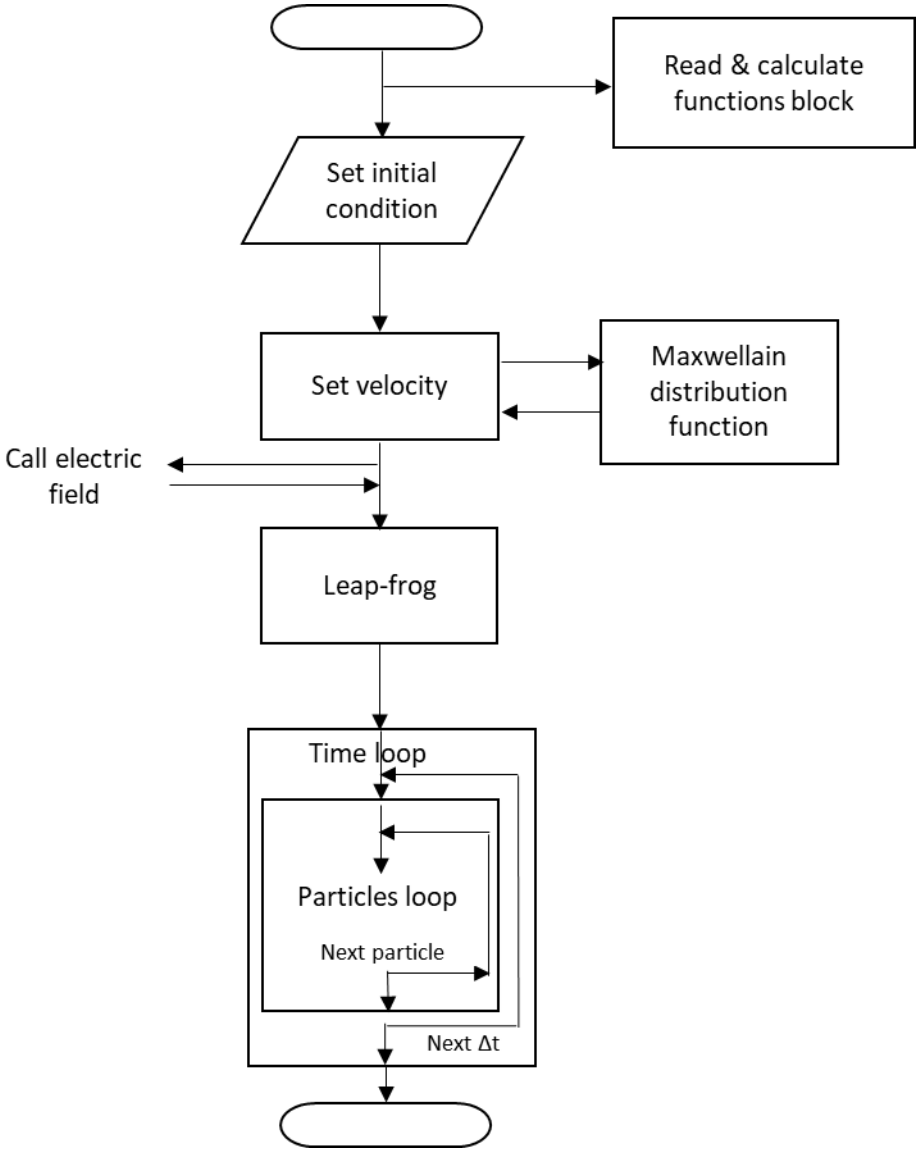

Fig. 3-5

Main code flow chart, particles loop consists of three loop, one for each particle, i, e, and fast n

3.4 Breakdown Criterion

The breakdown criterion is simply that the number of ions at the end of the simulation is equal or greater to that at the beginning - since ions are the effective charged particles in this regime. This means the lost particles are compensated by the created ones by ionization, so that any small voltage increment will cause an accumulated increase in the ions number, i.e. breakdown.

This was done in this work through two approaches. The first by starting with 100 charged particles (ions and electrons) to monitor the effects of different processes on the breakdown (see sections 4.4 and 4.5), this approach was the adopted in this work and all results introduced are according to it. The second was by following five parent ions, one after the other – for statistical purposes - and their creations i.e. daughter ions and daughter fast neutral until they all lost to boundaries or became not effective - i.e. the ions trapped or fast neutrals lost their energy through collisions that cannot cause ionization – or reach the selected simulation time, this was done as check, more details in section 4.2.

3.5 Verification of the code

Before running the code and collecting data, it is important to check the validity of the code and so be more confident about the output. This process will be described in the next three subsections

3.5.1 Particle Tracking

The idea is to track each kind of particle's trajectory alone according to the code without any collisions, and if that output is in agreement with that predicted according to theory, this will verify the field solver and the particle mover of the code.

Using the code with no collisions, tracking the trajectory of three single charged (He^+) ions whose initial position are distributed randomly in the domain is shown in Fig. (3-6). Two of them (grey and orange) hit the cathode and are lost; the orange had only one trip through the cathode, because it started from a point nearer to the anode than the wall, and gained less energy than the other two ions. The grey ion went four times through the cathode before it hit the cathode grid because it started from a point closer to the wall between two wires of the electrodes. The blue ion went through the cathode twice, but it started from the closest point to the wall, so it gained high energy and went near to the wall on the other side,

then back on almost the same track, but this time closer to a cathode wire, which affected its velocity, causing the track to bend. The bending effects of the wires and electric field are clearer for the other two ions because they had less energy, so these results are consistent with the theory prediction.

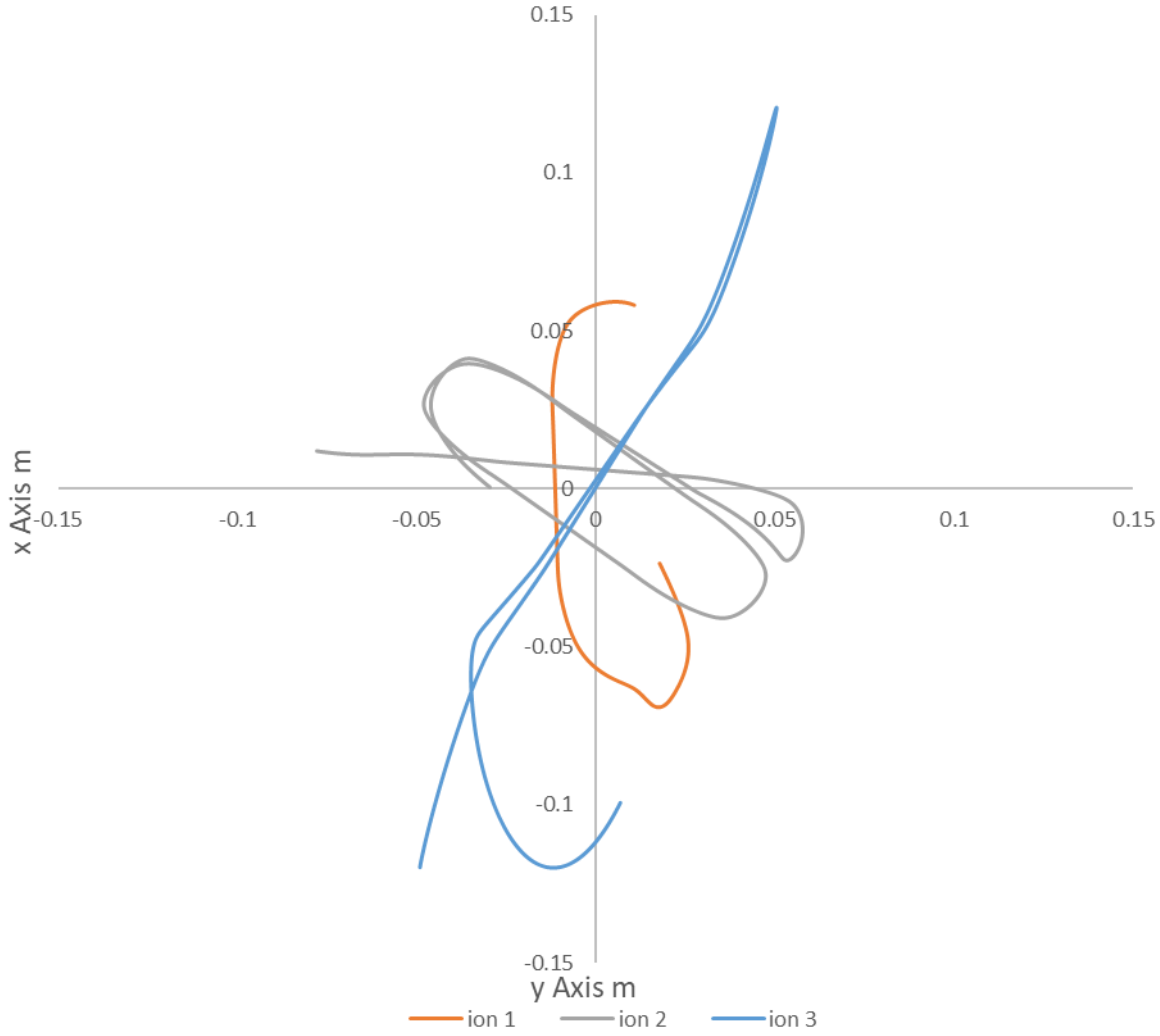

Fig. 3-6
Trajectory of three ions (without collision)

The same is done for electrons. Fig. (3-7) shows the trajectory (without collisions) of the last three electrons remaining in the simulation out of hundred electrons distributed randomly in the domain. Because these three electrons started from a point between the anode and the wall near the anode, where the electric field is relatively weak, they gained

less energy and remained in the simulation for longer time. The time required to lose all of them was 1.17 x 10^{-8} sec, which is a very short time because of the high mobility of the electrons, and all of them had only one trip toward the exterior, this is in agreement with predicted behaviour.

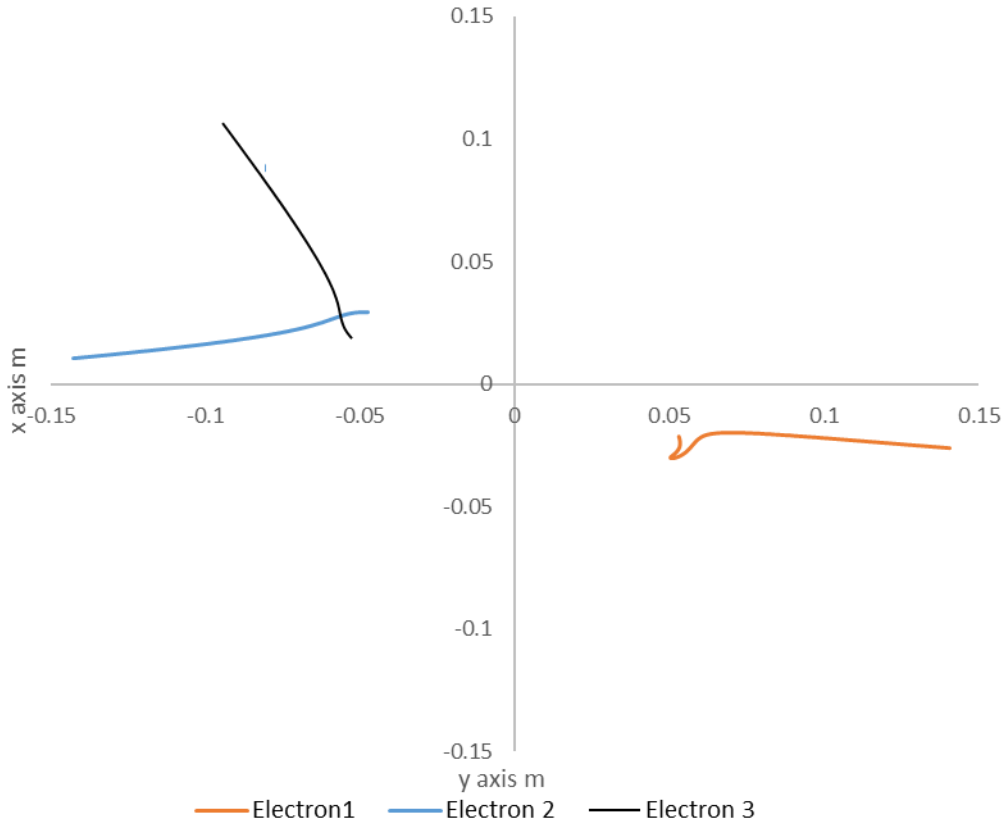

Fig. 3-7
Trajectory of last three electrons (without collision)

The code was also used to track three neutrals. Fig. (3-8) shows their trajectory, all had reflections from the wall, and one of them (orange) had three reflections from electrodes, two from the cathode and one from the anode. The electric field had no effect on them because of their neutrality, so there is no bending in their trajectories.

All three of the species' trajectories meet with the theoretical predictions, which supports the code validity.

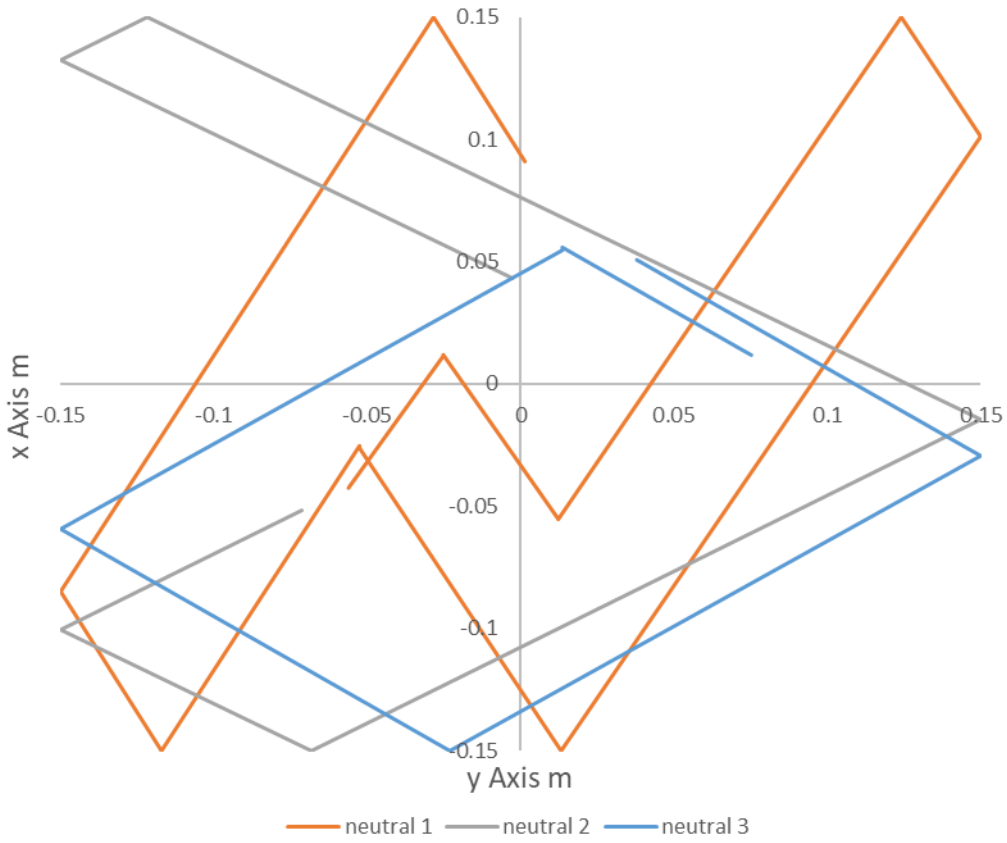

Fig. 3-8
Trajectory of three neutrals (without collision)

3.5.2 Collision Check

To test the collision block, a code based on the adopted theory of collision is used to evaluate the mean free path for each species. For all types of collision considered in the simulation, and for a specific energy, the cross section and the probability P_r of collision are calculated. Then, an iteration loop compares P_r with a random number R generated between 0 & 1; if no collision, i.e. $R > P_r$, the particle is advanced a distance of the particle velocity multiplied by one time-step, until a collision occurs. The travelled distance (free path) is recorded, and after the loop is repeated for a reasonable number of times to get an acceptable statistical error, the recorded paths are summed, and the total travelled distance is divided by the number of iterations to give the simulated mean free path (MFP). This is

then compared with the calculated MFP from the available cross section (σ) data (MFP = $1/n\sigma$ where n is the number of particles per unit volume). These were in good agreement with each other, Figures (3-9), (3-10), and (3-11) shown below, in which compare the calculated and simulated MFPs for all collisions, for ions, electrons, and neutrals respectively.

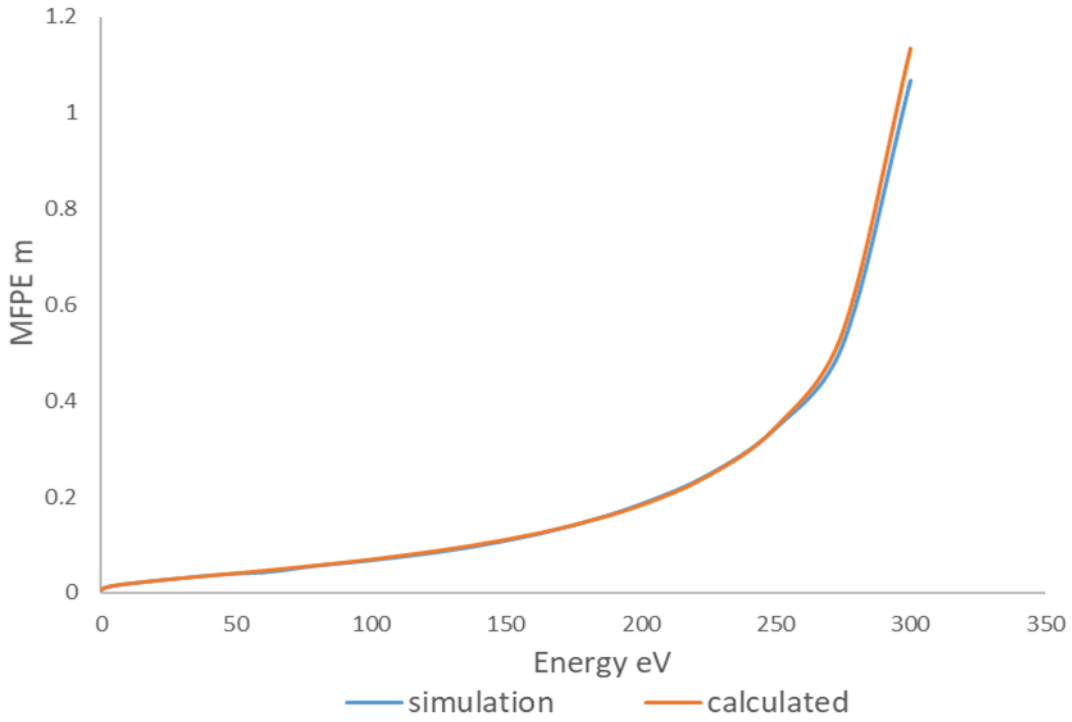

3-9 (a) Elastic

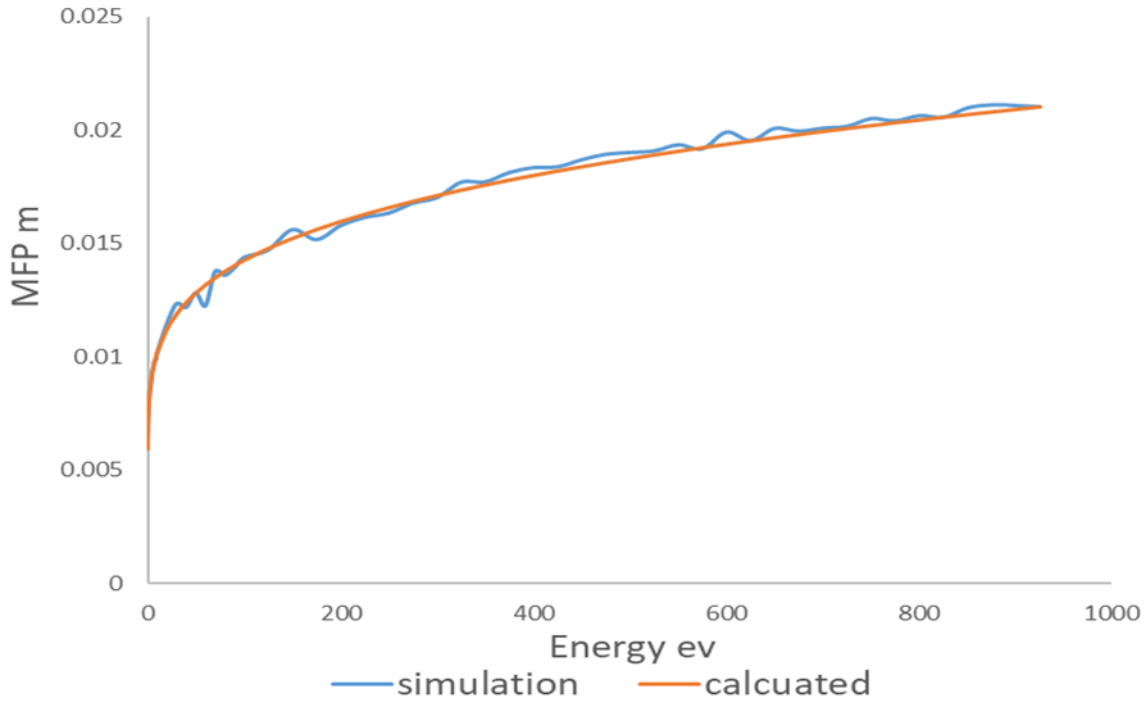

3-9 (b) Charge exchange

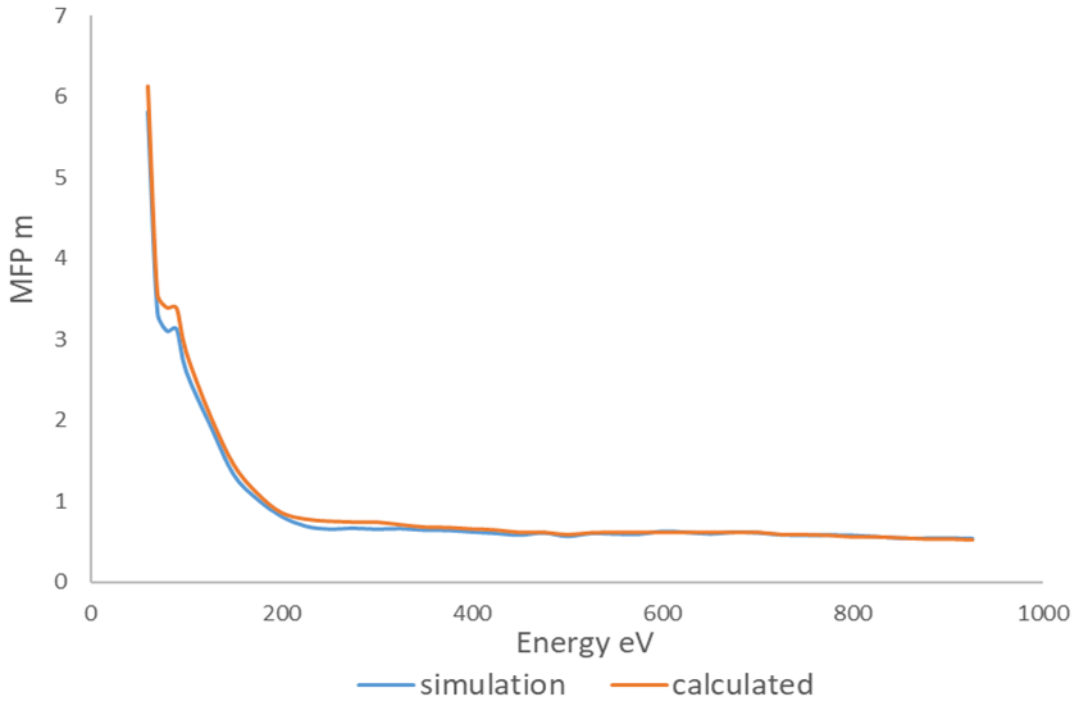

3-9 (c) Excitation

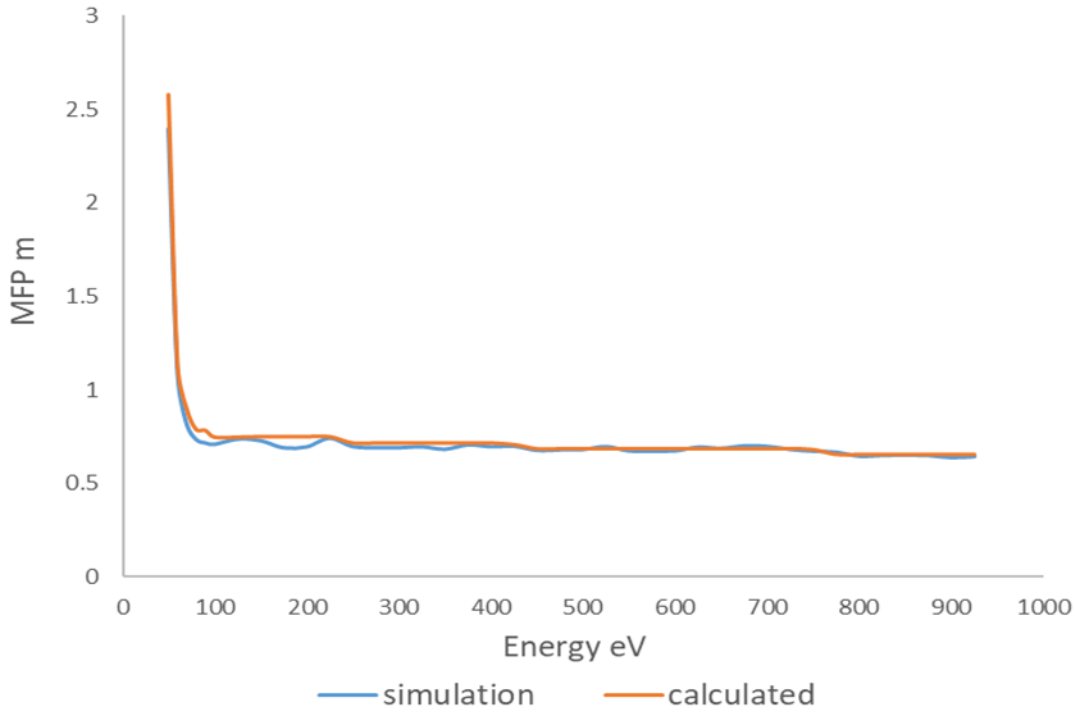

3-9 (d) Ionization

Fig. 3-9

Ions MFP calculated and simulated for (a) Elastic (b) Charge exchange

(c) Excitation (d) Ionization

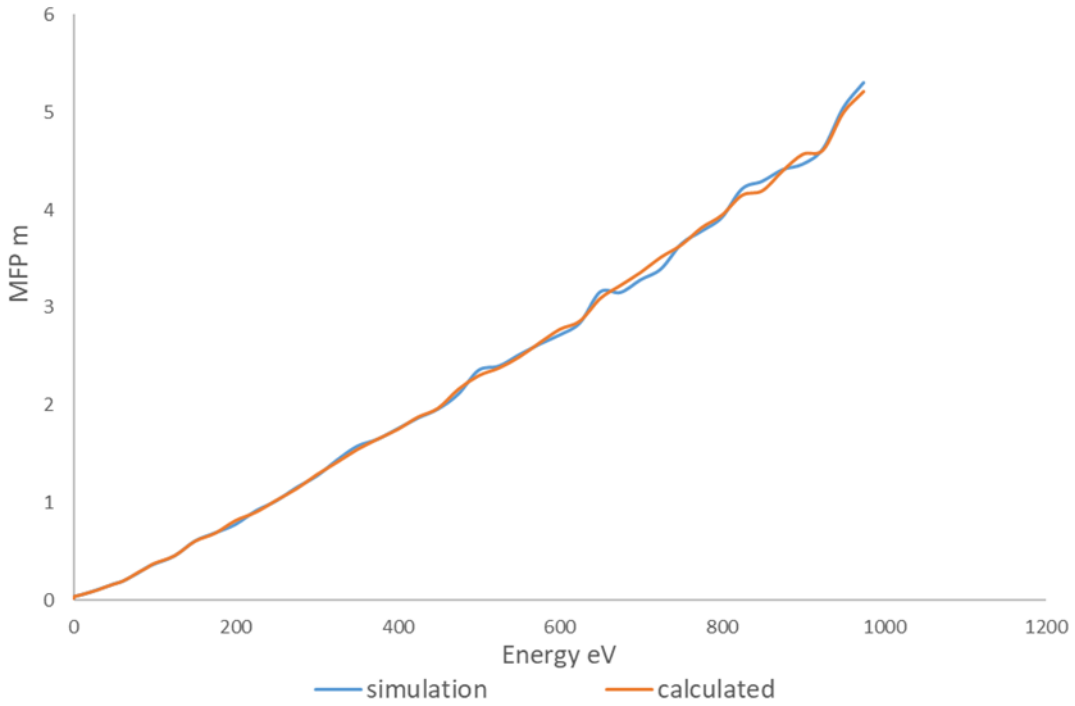

3-10 (a) Elastic

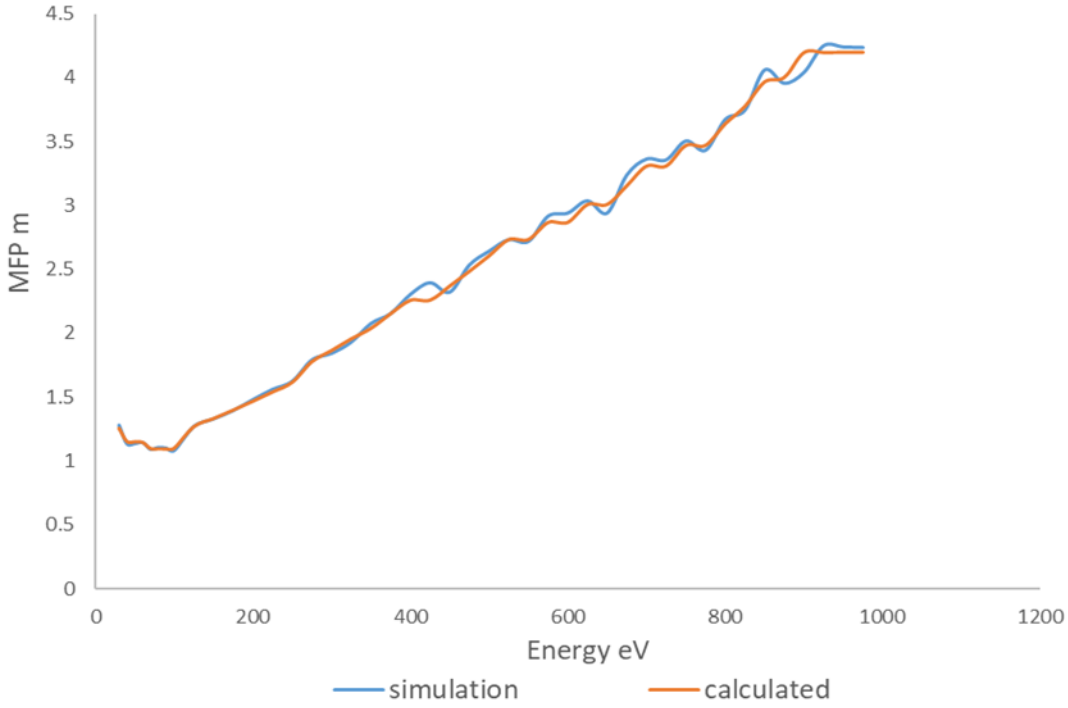

3-10 (b) Excitation

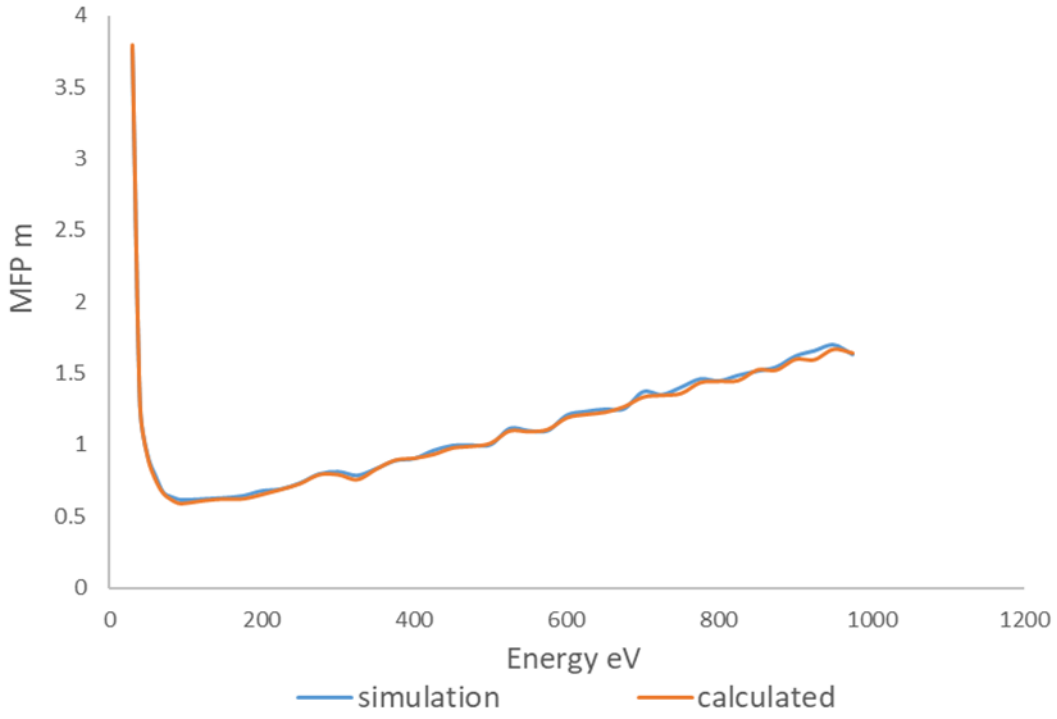

3-10 (c) Ionization

Fig. 3-10
Electrons MFP calculated and simulated for (a) Elastic (b) Excitation (c) Ionization

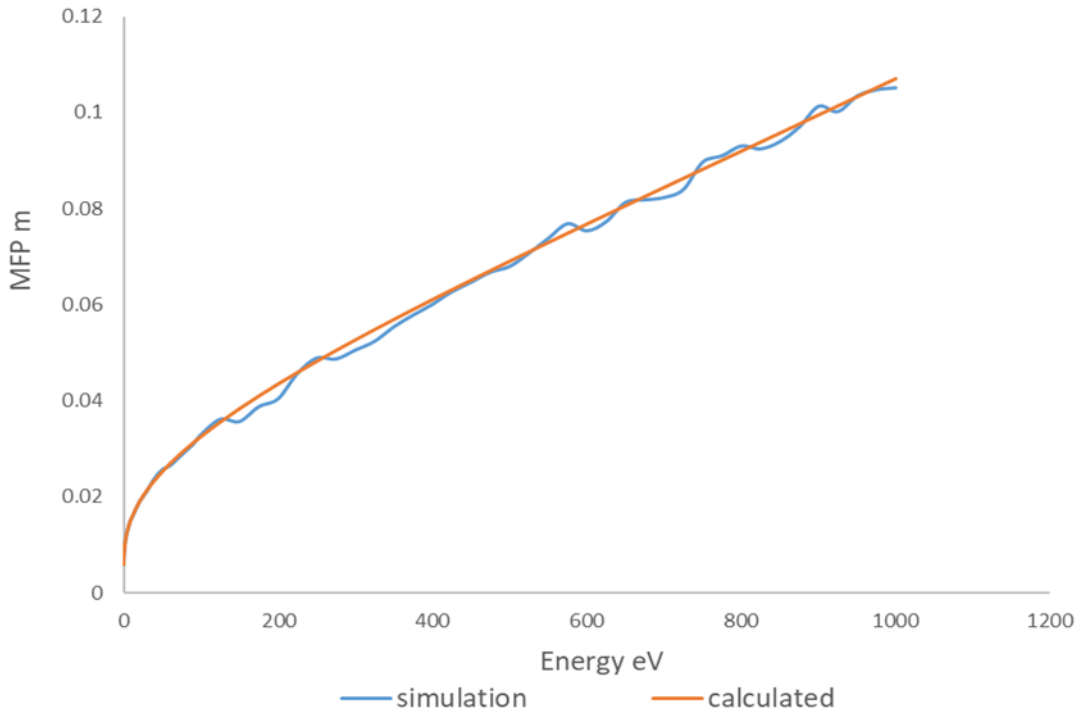

3-11 (a) Elastic

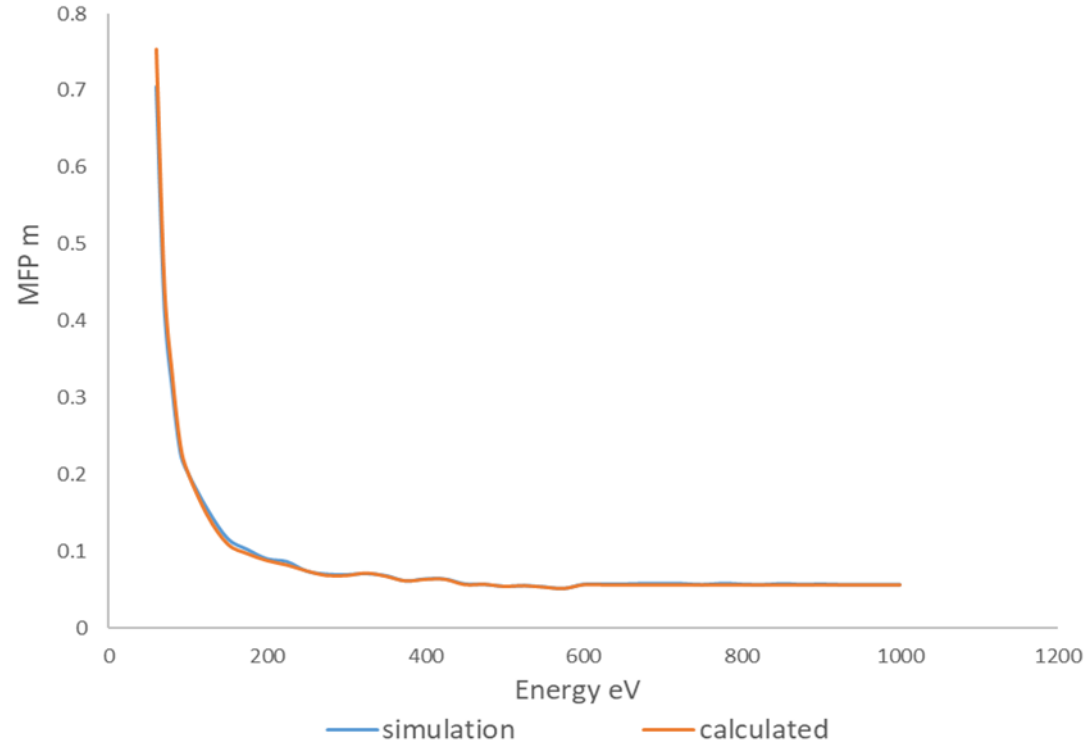

3-11 (b) Excitation

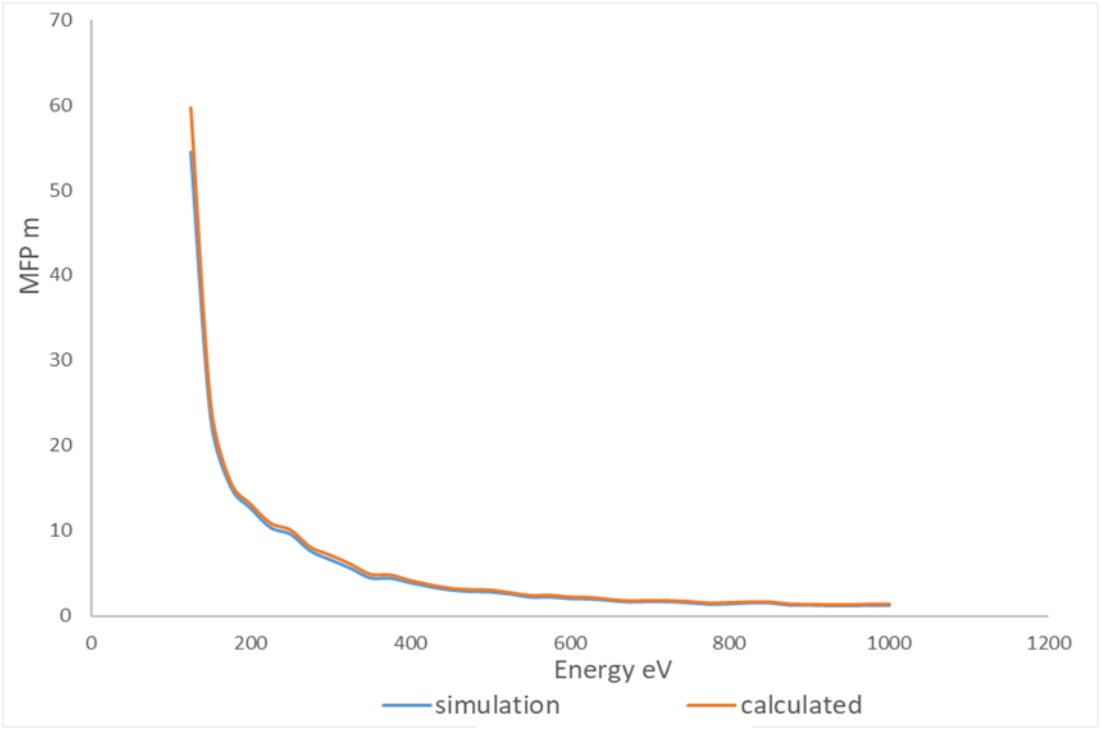

3-11 (c) Ionization

Fig. 3-11

Neutrals MFP calculated and simulated for (a) Elastic (b) Excitation (c) Ionization

The calculated curves are not smooth because they are in normal scale, while they have been generated from the smooth cross section curves which are in logarithmic scale.

3.5.3 Parallel Plates Paschen Curves

Another check was made by using the model to simulate the well-known parallel plates Paschen curves for helium. A model of 1D 1v with distance between the plates *d* = 20 cm is used to simulate the Paschen curve for helium. The electric field is constant, and so is equal to the applied voltage divided by the distance between the plates. The electrons are positioned next to the cathode, and the ions distributed randomly between the plates. The model is applied in the same way as outlined previously except the fast neutrals are not considered, since at the relatively high pressures at which this simulation is meant to function, the ions will collide before gaining enough energy to produce sufficient fast neutrals to affect the system. The results are plotted in Fig. (3-11) (orange) in comparison with the experimental data (blue). The plot shows a shift between them which is justified by knowing that the simulation results are just before the breakdown, while the experimental are just after that, although they are in good agreement.

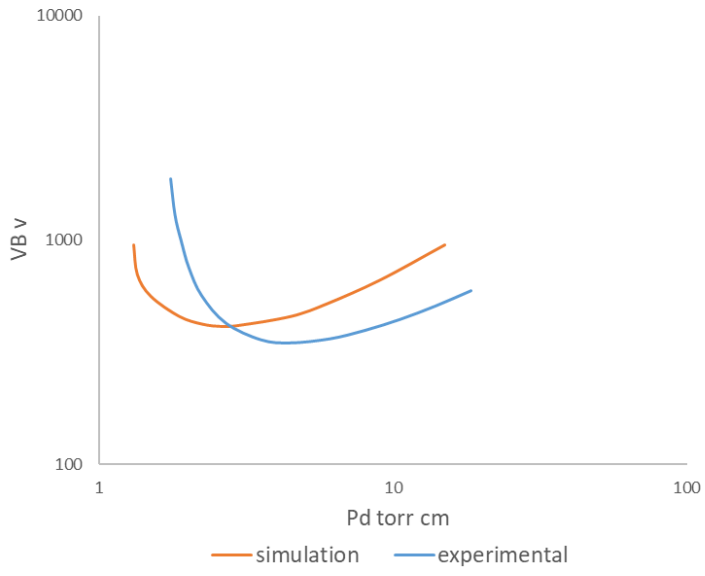

Fig. 3-12
He Paschen Curve simulated and experimental

Chapter 4
Simulation of Breakdown in a Cylindrical TCD

This chapter contains an investigation of breakdown for one particular configuration of a transparent cathode discharge (TCD). The majority of IEC discharge work has been performed at pressure between 2-7 Pa [1,13], and so the simulation code described in Chapter 3 was used to determine the breakdown voltage for a series of background gas pressures in this range. This TCD configuration was chosen because there are experimental values of breakdown voltage for this case, obtained by T. Hardiment as part of his PhD research [59]. These measurements are used to compare with the breakdown voltages determined by the code. Results are presented, and the relative importance of the different physical mechanisms are discussed.

4.1 TCD Configuration

The arrangement of the experimental TCD is shown in Fig. (4-1). This geometry has two concentric cylindrical grid electrodes, with the inner and outer grids having radii of 2.875 cm and 5.75 cm respectively. Each grid consists of 14 straight wires in the longitudinal (axial) direction and four circular wires (rings) in the azimuthal direction, with the outer grid wires forming apertures with a square cross-section of 2.5 cm x 2.5 cm and for the inner grid, 2.5 cm x 1.25 cm. Both grids are made of stainless steel wires of 0.08 cm radius. The electrodes were mounted by a stalk in the centre of a cubic vacuum chamber, made from stainless steel with each side having a length of 30 cm. In the experimental study, the inner grid was designated as the cathode and the outer grid as the anode. The cathode was connected to a large negative dc voltage, while the anode and chamber walls were grounded.

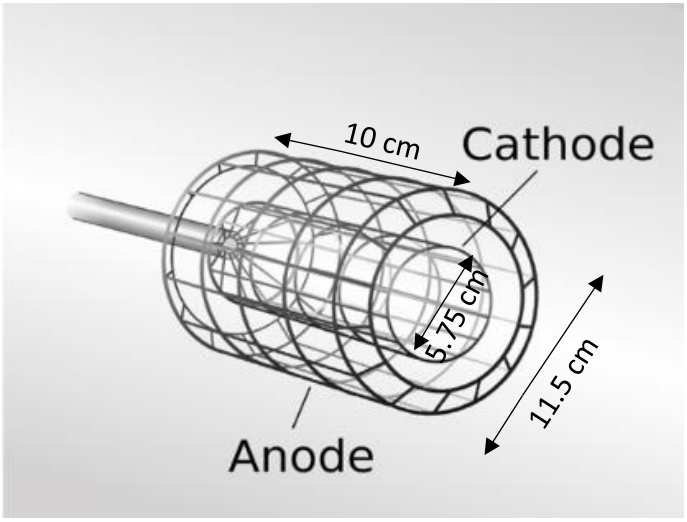

Fig 4-1

Schematic diagram for cylindrical TCD

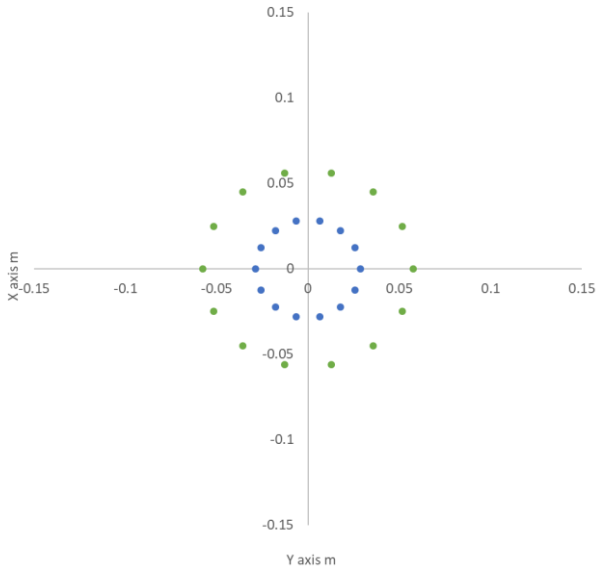

Fig. 4-2

Two-dimensional grid structure used in simulation

Figure (4-2) shows the geometry implemented in the two-dimensional simulation. The general arrangement has already been discussed in Chapter 3, but the arrangement is shown here again so that a comparison with the three-dimensional experiment can be made. As in

the experiment, the anode and cathode grids are aligned and have 14 wires in the longitudinal direction, they are in a square chamber of 30 cm a side. For the particle-surface interaction calculation, the wires and the wall have been given the electrical properties of stainless steel.

Since the two-dimensional plane of simulation is located axially in the middle of a ring of apertures, the rings visible in the real grid that connect the wires are not represented in the simulation. This will have two main effects. The first is that there will be an extra electric field around these circular wires, which cause the simulation field structure to differ slightly from the experiment, in which an additional electric force on the charged particles will be exerted in the axial direction as well. The second is that the surface area available for particle interaction will be reduced in the simulation (higher electrode transparency) as compared with the experiment, because of the proportionately smaller wire surface. Another difference concerns the end effects, where the electrical potential distribution at the ends of the cylindrical electrodes is different to that in the middle, as well as the effect of the stalk that provides the electrical connection and holds the cathode in the chamber. These effects will cause additional ion bombardment which is likely to cause premature breakdown [1] compared to the simulation.

Figure (4-3) shows the potential distribution given for the 2D simulation. This distribution has already been presented and discussed in Section 3.1.1, it shows the distribution, the general features of the distribution, such as the large field in the inter-electrode space, the non-zero field outside the anode, and the flat distribution in the central region inside the cathode, so the points that will be discussed in this chapter, can be clearer.

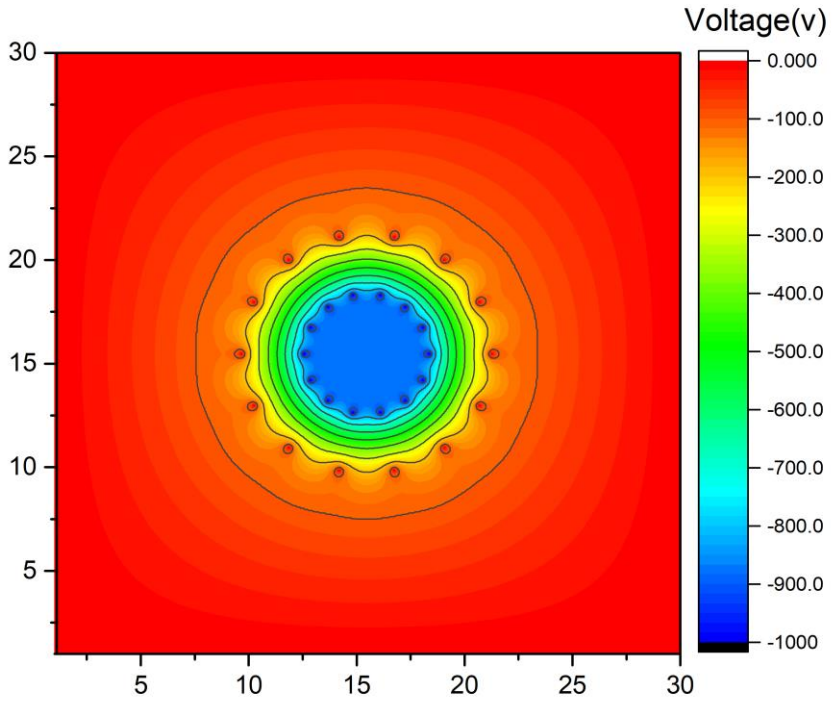

Fig 4-3
Potential Distribution for 14 wires aligned electrodes, 1 kV applied voltage

4.2 Effect of Different Breakdown Criterion

4.2.1 An Alternative Breakdown Criterion

To be more confident about the results, an alternative approach was used to determine the value of the breakdown voltage. The approach that is described in Chapter 3 and used to determine the results in the previous section is based on calculating a large set of particles simultaneously for a pre-determined time, and comparing the number of particles at the end of the calculation with the number of seed particles at its beginning. The alternative approach was based on tracking particles in a single avalanche, and tracking multiple seed particles to see how many of these generate successful avalanches, and also how particles generate an avalanche that dies away quickly. In this approach, a single ion was tracked until either it was lost, or a pre-set simulation time was reached. Information about the location, time, position and velocity of any new particle generated (electron, ion and energetic

neutral) was recorded. When the original particle was lost, or the simulation time reached, the trajectory of the next particle in this avalanche was calculated until it too was lost or reached the end of the simulation time. In this way, all the newly generated particles were tracked one-by-one starting from time they were created.

To handle this in the code, a two dimensional vector v was used. The parent ion is assumed as the first element, i.e. v(0,0) and the array (vector) was extended as necessary to contain the created ions, so the first daughter created either by the ion itself or by its fast neutral creations - was assumed v(0,1) and so on. The criterion for breakdown assumed that if at the end of the simulation starting with one ion there is still at least one ion in the system, the charged particle is sustained, and any small increase in voltage will lead to charge particle accumulation and consequently breakdown. Because it is a random process, the ion may be lost in very early stages or trapped. The code is designed to run for multiple parent ions, and the appearance of a successful avalanche was monitored. The results of this alternative approach were in good agreement with the adopted approach.

4.2.2 Quantitative Changes to Original Breakdown Criterion

Another issue is that the effect quantitative changes to the original breakdown criterion, i.e. time-step, simulation time and number of seed particles, the chosen time-step was 10^{-11} sec, when changing that to 10^{-10} sec, the output breakdown voltage for multiple runs differed more from run to run with respect to original time-step, while, by changing the time-step to 10^{-12} sec the output has no remarkable difference from the original one.

Simulation time was chosen to be 10^{-5} sec. Through analysing data during simulation, i.e. effective ions number (ion not trapped), number of energetic neutrals . . . etc., these quantities are found to fluctuate up and down noticeably in the beginning, then the fluctuation reduces with time until it became respectively small. This time required for the data to be almost stable was chosen as the simulation time, because before that time, the

output may be at a peak or a minimum, making the result unreliable. Since after that time, the data is almost stable, there is no point in exceeding that time.

The number of seed particles was chosen to be 100 particles (for both ions and electrons) in a way to get an acceptable statistical error in output of the simulation. Reducing that number causes an increase in the statistical error interval, while little difference is caused by increasing that number. All these choices are made in compromise between acceptable statistical error and computational cost.

4.3 Paschen Curves for this TCD Configuration

Figure (4-4) shows the Paschen curves determined by experiment (as already noted, these measurements were made separately to the research described in this thesis), and by simulation. For the simulation results, it can be seen that the agreement is best at the lowest pressures. They have in general the same trend in spite of the simulation voltages being significantly higher for higher pressures. This difference can be due to at least two main reasons. The first is that the cylindrical TCD configuration can be viewed as a two-dimensional spherical TCD [1], this will lead to what was mentioned in Section 4.1 about the effect of the difference between the two dimensional simulation and three-dimensional experiment. The second is that the fast electrons lost to the wall and anode mostly cause x-ray emission through bremsstrahlung; these x-ray photons will travel through the chamber and hit the wall, the anode or the cathode, resulting in emission of energetic photo-electrons, that can cause ionization collisions. At low pressures the mean free path is longer, so the particles will suffer fewer collisions and gain more energy before colliding, i.e. less charged particles but more energetic, so fewer electrons will hit the wall or the anode, and produce fewer more energetic x-ray photons. As the pressure increased, the number of these photons will be higher but have less energy, so the effect of the photo-electrons will be more

significant. This may explain why the simulations and the experimental curves are close at low pressure, while the simulations curves are higher for higher pressures. The existence of x-rays was confirmed when the safety team checked the regime during the experiment, since their equipment detected that.

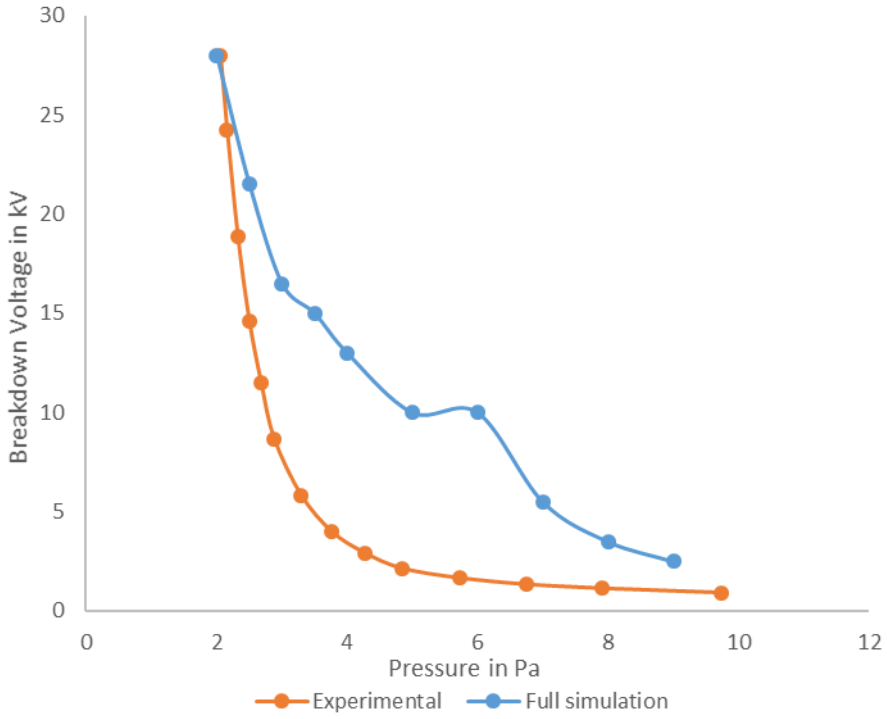

Fig 4-4

Pressure vs Breakdown Voltage for Full Simulation and Experimental

To take this effect into account research is proposed, to measure the x-ray flux, and the average energy of x-ray photons in the system for each pressure, and so if possible reach a formula for the relation between the pressure and x-ray flux and average energy. Alternatively, tabulated values of these for each pressure could be fed to the code. With the absorption coefficient and the secondary photo-electron yield for the material of the wall and electrodes, statements could be added to the code that use all these factors to calculate the x-ray effect on breakdown.

4.4 Analysis of Breakdown Processes

The main conclusion from Section 4.3 is that the breakdown voltages calculated from the simulation code are in semi-quantitative agreement with the experimental values. This agreement gives confidence that the physical mechanisms contained in the simulation code are a reasonable representation of the real situation. This section analyses the processes and how they influence the breakdown process.

4.4.1 Effect of Individual Mechanisms

Figure (4-5) shows the ionization events induced by different processes in the plasma volume. As explained in Chapters 2 and 3, ionization in the discharge volume can occur through collisions of energetic species with background gas atoms, with the energetic species including fast neutral atoms created by elastic and charge-exchange collisions with ions.

The figure shows a reduction in ionizations caused by ions and fast neutrals as the pressure increased, while the electron ionization is slightly raised then slightly reduced as the pressure increased. Consequently, the total ionization for high pressures was dominated by the electrons' ionization. There is a property that affects most of these mechanisms, that is, as the pressure increases the number of background particles increases, which leads to reduction of the mean free path for all species. Change in the collision cross sections depend on the type of collision, consequently the number of collision will be different according to the kind of collision. So the number of ionization collision reduced as the pressure is raised because the charged particle suffered other collisions before they gain enough energy to ionize, the same logic applied for the creation fast neutrals (fast neutral can cause ionization) as in Fig. (4-5).

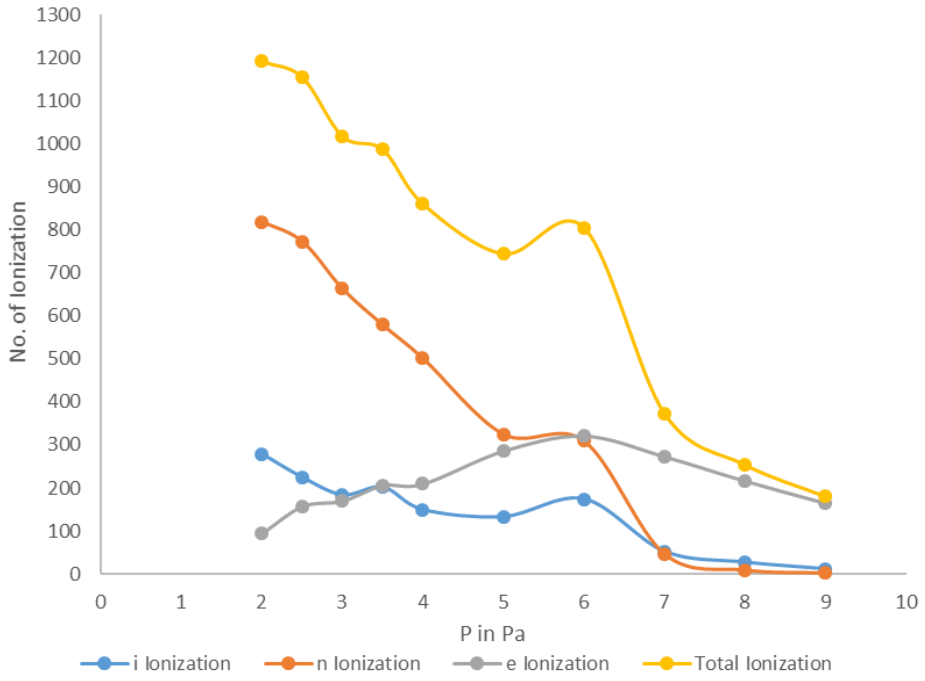

Fig 4-5

Pressure vs Ionization Events by Ions, Electrons & Fast Neutrals at Breakdown Voltage

Figure (4-6) shows the number of secondary electron emission (SEE) at the cathode surface and electron back-scattering (BS) from all surfaces (cathode, anode and wall) for different pressures at breakdown voltages. It shows reduction for both with increasing pressure, because the number of particles that reached the boundaries were less for the same reason mentioned above.

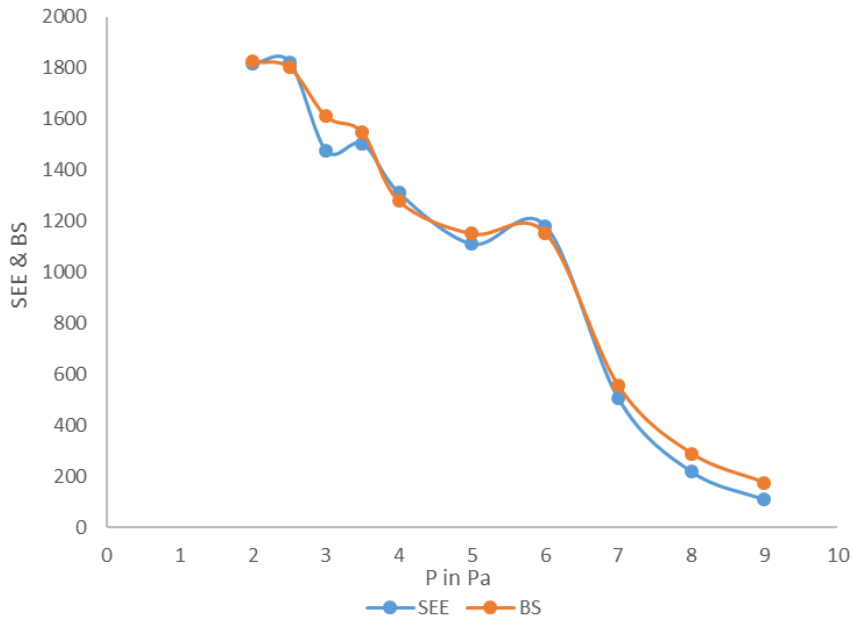

Fig 4-6

Pressure vs Secondary Electrons Emission at the cathode & Electron Back-Scattering at Breakdown Voltage

The number of ions converted to neutrals by reflecting from the cathode and the number of neutrals converted to ions at the wall and anode are shown, at breakdown voltages for different pressures, in Fig. (4-7), these numbers decreased in general as the pressure increases, because the number of particles that reached the boundaries were less and as is their energies, due to mean free path and collisions effects mentioned previously. Because of the energy issue, the fast neutrals could not reach the threshold energy needed to be converted to an ion.

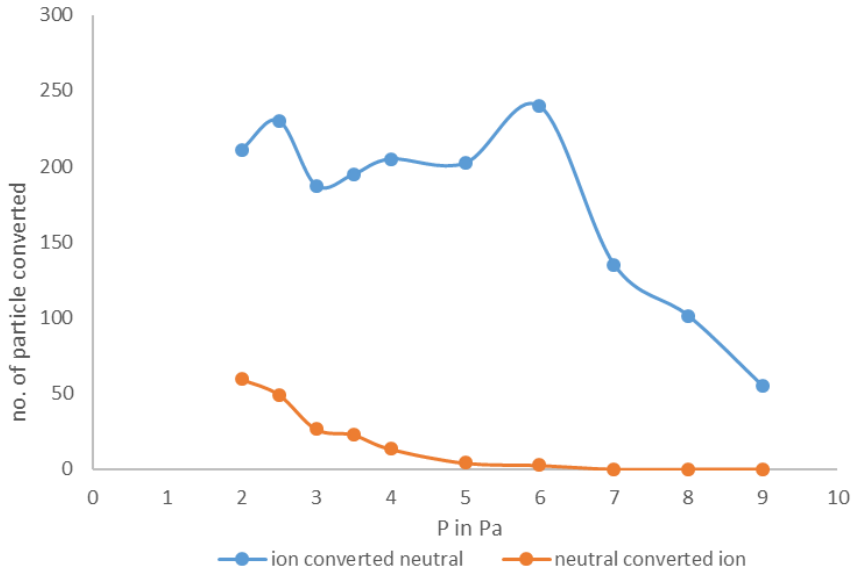

Fig 4-7

Pressure vs Particle Converted (Ions & Neutrals) at Breakdown Voltage

The effect of mean free path, cross section, and collision due to increasing the pressure, on other processes were noted, so at the end of the simulation with the pressure increment, the number of remaining ions in the domain decreased, the number of ions and electron lost to the electrodes and wall decreased, and excitation events for all species decreased, thus the influence of various processes as shown and discussed above according to the simulation are an acceptable representation of real situation.

4.4.2 Cumulative Effects of Particle Processes on the Paschen Curve

The discussion above focused on the effect of how individual processes changed over the pressure range of interest. It is also interesting to see the cumulative effect of these processes, and how they influence the value of breakdown determined from the simulation code.

In order to see the cumulative effects of the different collision processes, Paschen curves were obtained for the different simulation conditions outlined below. As can be seen, the first condition contains a very restricted set of physical mechanisms, and the simulation becomes increasingly realistic as further mechanisms are added.

Case A: Only volume processes, including all the gas phase collision processes described in Section 2.3.

Case B: All the volume processes contained in Case A, plus secondary electron emission at the cathode surface (SEE). As discussed elsewhere, secondary electron emission from the anode and wall surfaces are not considered as the emitted electrons are rapidly driven back onto the surface due to the electric field above these surfaces.

Case C: All the processes contained in Case B, plus backscattering (BS) processes for electrons incident on surfaces.

Case D: All the processes contained in Case C plus the neutral-ion conversion processes. This case is the same as that shown in Fig. (4.4), as this case represented the full simulation.

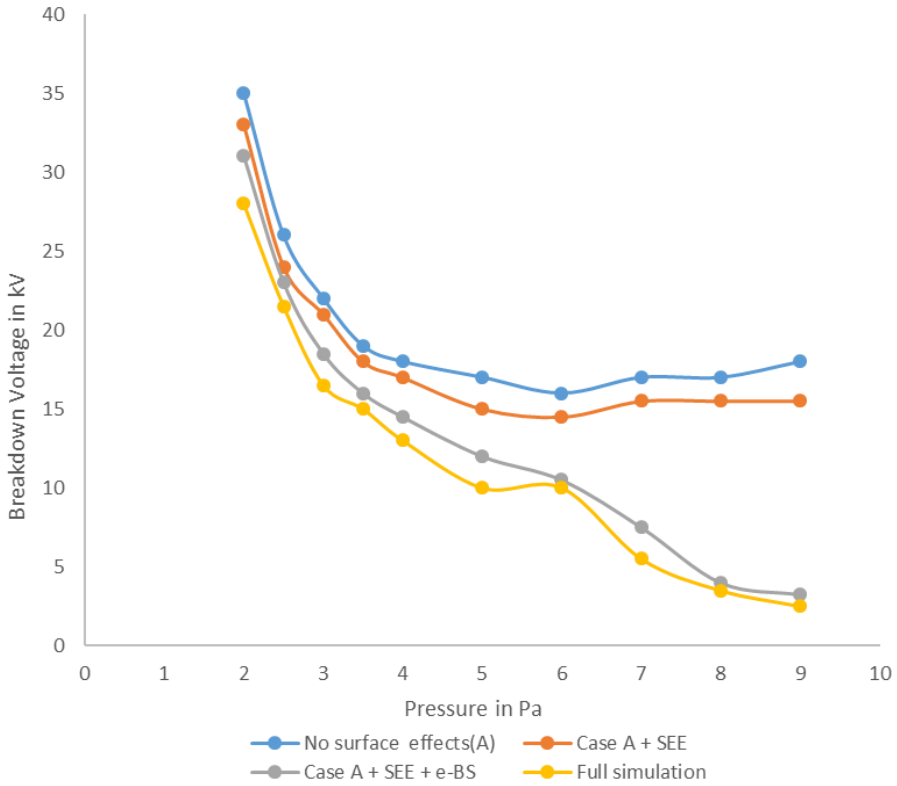

Fig 4-8

Pressure vs Breakdown Voltage for Different Simulation Conditions

Fig. (4-8) shows that the breakdown voltages are decreased for each condition as further mechanisms are added, although, the four cases are close to each other at lowest pressures, at which they are also in best agreement with reality. On the other side, as the pressure increased, Cases A & B are still close to each other, and split from Cases C & D, which means that the secondary electron emission makes only a small contribution to the ionisation yield, while the electron back scattering contributes more to the simulation than either SEE or the mechanism added in the last case, i.e. particle conversion. This with curve of fig (4-7) may explain the bomb in the curve of simulation at pressure 6 Pa, which reveal that this bomb is not exist before adding particle conversion and it caused by ion conversion to neutrals.

4.5 Accumulation of Particles in the Centre of the Cathode

It was mentioned in Section 1.5 that the ions are accelerated toward the transparent cathode, and pass through its centre to the other side unless they suffer a collision event, which may cause the collided ion to lose most of its energy and become, a low-energy ion in the centre will move very slowly in a free space area where there is no electric field except around the cathode's wires, thus trapped in the centre until the ion comes near a grid wire, and is accelerated toward the cathode, hit and lost. These ions accumulate in the centre and establish a high ion population in the centre. While these low energy ions are considered to play no role in determining whether or not breakdown occurs, the process of depositing low energy ions in the cathode centre may play a significant role in the evolution of the discharge from breakdown to a steady-state, and so it is interesting to see how this process develops in the simulation.

Fig. (4-9) shows the ion distribution at the end of full simulation breakdown at a pressure of 2.5 Pa and applied breakdown voltage of 21 kV as an example. In Fig (4-9 a) the x axis divided into intervals of 2 cm long and the number of ions in each intervals is plotted, the same idea in Fig (4-9 b) but for the y axis, in Fig (4-9 c) the domain is divided to nine cells each cell of 3 cm × 3 cm the number of ions in each cell is recorded in the pot of this grid. These plots show the high density ions in the cathode interior, although even if there are 725 ions in the center, they are still less than sufficient to cause space charge.

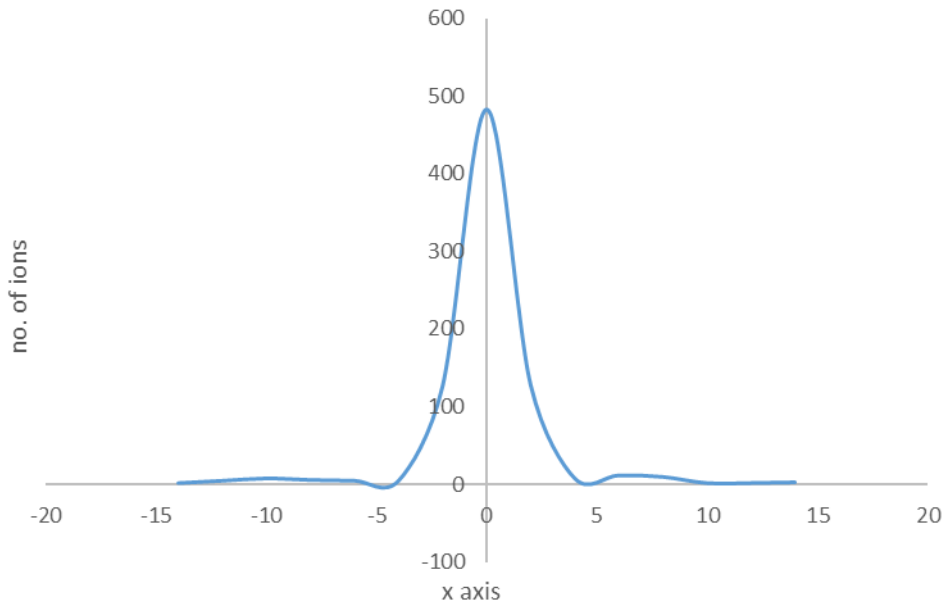

Fig 4-9 a

X axis intervals vs ions number in each interval

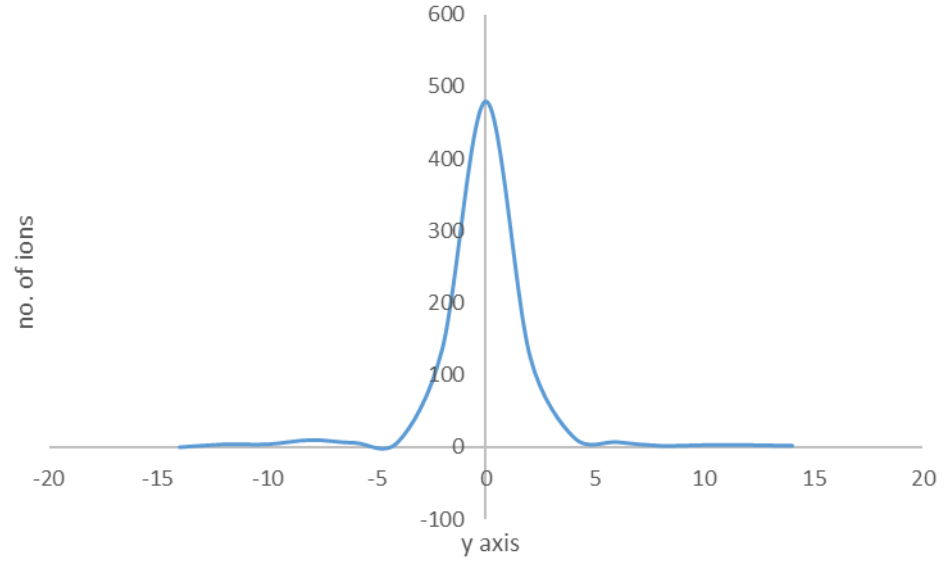

Fig 4-9 b

Y axis intervals vs ions number in each interval

	(-0.15 to -0.9)	(-0.9 to -0.3)	(-0.3 to 0.3)	(0.3 to 0.9)	(0.9 to 0.15)
(0.15 to 0.9)	0	2	2	1	2
(0.9 to 0.3)	4	3	6	9	1
(0.3 to -0.3)	5	6	725	4	3
(-0.3 to -0.9)	3	4	4	13	0
(-0.9 to -0.15)	2	1	1	3	1

Fig 4-9 c

Domain grid cells and ions number in each cell

The simulations show accumulation of ions within the interior of the cathode which supports the assumption of virtual electrode (anode) formation; in the next stage, the repulsion between them will leave a low ion density area in the centre and the ions will be distributed around this area in a way they will be denser in the places where they face the in between of the cathode wires, where the attraction effects are less than those facing them where they are stronger. The virtual electrode is assumed to confine the opposite charge species (electrons) which is supported by the results through the number of trapped electrons within the cathodes (electrons with low energy that cannot escape from the interior of the cathode), believed to be created by ionization collisions take place in the interior of the cathode by ions or energetic neutral; table (4-1) shows these numbers for different pressures in full simulation.

Table 4-1

Number of trapped electrons in the cathode interior in full simulation

Pressure(Pa)	2	2.5	3	3.5	4	5	6	7	8	9
Trapped electrons	436	412	375	394	341	298	269	127	63	37

4.6 Comparison with Breakdown Reported for other Configurations

Liang Xu et al. [24] and Hartmann, P. et al. [23] discussed helium low pressure breakdown between two parallel plates. They concluded the importance of fast neutrals on breakdown at very low pressures, through their ionization collisions and induced secondary electron emission, and also they studied the effect of electron backscattered from the anode, Liang Xu et al. discussed the influence of the reflection of ions from the cathode as fast neutral, but neither of them mentioned anything about the fast neutrals conversation to ions. In summary their findings were in good agreement with the results of the present simulation, taking into consideration the differences between the two configurations.

Miley, George H., et al. [14] studied breakdown voltage characteristics for a single-gridded spherical IEC, where the chamber wall is the anode. They mentioned the effect of the mean free path, and cross section as the pressure increased, which is in agreement with results of present work. They also compared breakdown with a solid spherical cathode to that using conventional plane parallel plates and also a transparent cathode. They found that the parallel plates and the solid cathode discharges are a good match to each other, and for the same breakdown voltage the (*Pd*) is about three times that of the transparent cathode. This difference is attributed to ion flow through the transparent grid cathode.

4.7 Effect of Electrode Transparency

Cathode transparency allows the ions to travel through it back and forth many trips before they hit the cathode and are lost from the system, compared to conventional solid electrode, where the ions cannot go through and have only one trip, hit it and are lost. This will elongate their path and life time, which will increase their possibility of interaction with background neutrals on one hand, and will create high density ions region in the interior of the cathode on the other hand.

Electrons on the other hand, instead of hitting the anode - as in solid electrode - will mostly pass through the anode towards the walls of the chamber. This will lengthen the electron trajectory and consequently raise their interaction probability, and could create ions in outer region of the anode.

Neutrals unlike the charged particles are not attracted to either of the electrodes, and move all around the chamber, so the neutrals can travel through the transparent electrodes and benefit from extra movement space compared to solid electrodes, therefore the fast neutral often created by ion charge exchange collisions can generate ions anywhere in the domain.

The transparency of the electrodes causes the formation of what is called ion microchannel, these microchannels guide the ions through the opening of electrode grid. Microchannel can be visualized in very low pressure discharge of IEC as spokes of light emanated through the grid holes, they radiate both outward from the cathode to the anode and inward to the centre of the cathode [1,13].

Backscattering at the walls causes electrons to lose energy, which increase their cross section (see Fig. 2-7), i.e. increases their ability to produce ions in the outer region of the anode, ions created in the outer region of the anode gain maximum possible energy due to

electrical field, not like the ones created between the electrodes as in solid electrodes, which they benefit only from part of that energy.

Because of all these factors, at very low pressures, breakdown voltages in transparent electrodes are significantly less compared to that of conventional solid electrodes which increases dramatically as pressure reduces.

4.8 Summary and Conclusions

In summary the agreement of the simulation with the experimental is the best for the lowest pressures, but there are noticeable differences between them at higher pressures. This might be due to differences between the two dimensional simulation and the three dimensional experiment, in addition to the effect of x-ray emission through bremsstrahlung by the impact of fast electrons on the wall and anode. The effect of pressure increment on mean free path, collision cross sections and consequently on breakdown were confirmed.

Chapter 5

Simulation of Breakdown for Alternative Electrode Configurations

The aim of this chapter is to use the code to study the effects of different configuration factors on breakdown, e.g. number of electrodes wires. To reveal the role of each factor on breakdown, different values substituted for the original configuration by making suitable arrangements in the code. This is the one of the main advantages of simulation; that saves the time, and cost of building an experiment for each case.

5.1 Alterative Configurations

Three different effects were investigated:

1. The number of wires effect. By implementing 20- and 8-wires aligned electrodes instead of the original 14-wires aligned electrodes, using the same electrode and chamber sizes.
2. The effects of the electrode radius. By taking two values for anode radius, 1.25 and 0.75 times of the original anode radius, 0.072 and 0.043 cm respectively, with 14-wire aligned electrodes and the same sizes for cathode and chamber.
3. The alignment effect, half out of phase aligned electrodes by rotating the anode through an angle of $\pi/14$, i.e. half the angle between the apertures, with the same numbers of wires, and electrode and wall sizes.

For each of these five cases the work is restricted to pressures 2-7 Pa (estimated operation pressures), and the potential and electrical field components E_x , E_y distributions were calculated according to the methods explained in Section 2.2.

Fig. (5-1) shows the potential distribution for the original configuration. Although this was shown before in chapter 3, but it is shown here again so comparison with the other configurations can be made.

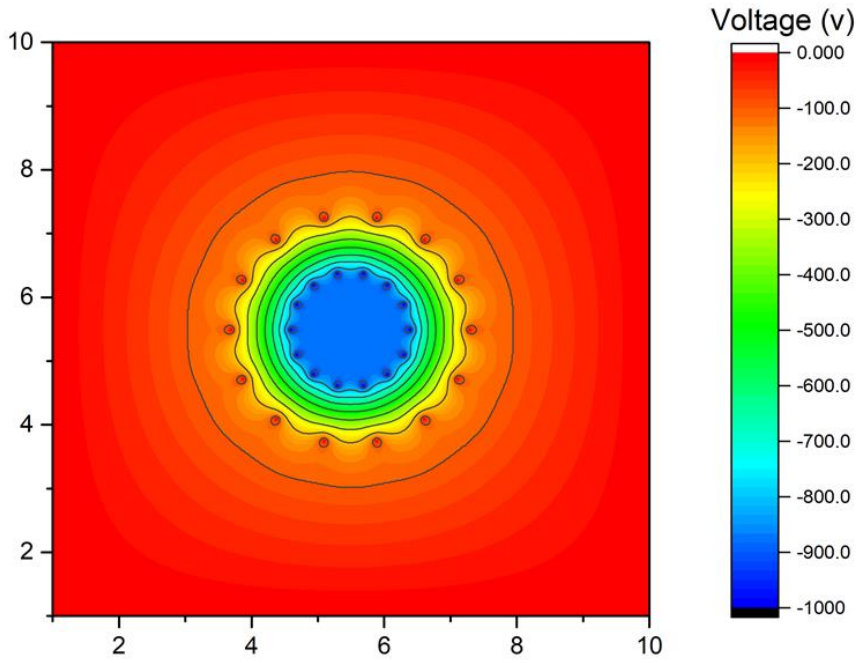

Fig 5-1
Potential Distribution for 14 Wires Aligned Electrodes, 1 kV Applied Voltage

5.2 The Effect of Changing the Number of Electrode Wires

As mentioned in Section 5.1 two different numbers of wires were simulated, 20 and 8, using the same stainless steel wires. The two electrodes were aligned, and have the same radius as the original, arranged within the same chamber. These changes cause to change the geometrical transparency; effects of electrode transparency on breakdown has been already discussed in Section 4.7.

Figures (5-2) and (5-3) shows the potential distribution for 8 and 20 wires respectively, to compare with each other and with the original configuration potential distribution. There are four areas to be noticed: around the electrodes wires, in the interior of the cathode, the area between the electrodes and the area between the anode and the walls of the chamber. In general, the potential for the 8-wire configuration is distributed wider than the original in the whole domain except near the walls, while the 20-wires is the narrowest and the original is in between. The potential around the 8-wires reduces very fast to the inside direction, and reduces relatively slowly to the outside direction, so the interior of the cathode and a narrow shell around it has almost the same potential – remarkably less than that around the wires. There are regions outside the anode with significant potential. While the potential around 20-wires is almost the same for the interior of the cathode, the potential reduces dramatically between the cathode and the anode. This causes very narrow regions with different potential from the cathode to the anode, and a very low potential in the outer region between the anode and the chamber walls. The original configuration is in between these two cases as would be expected. So the potential in the centre is high but still a little less than that around the wires, and the potential reduces gradually to the outside direction, so there is relatively narrow region outside the anode with noticeable potential.

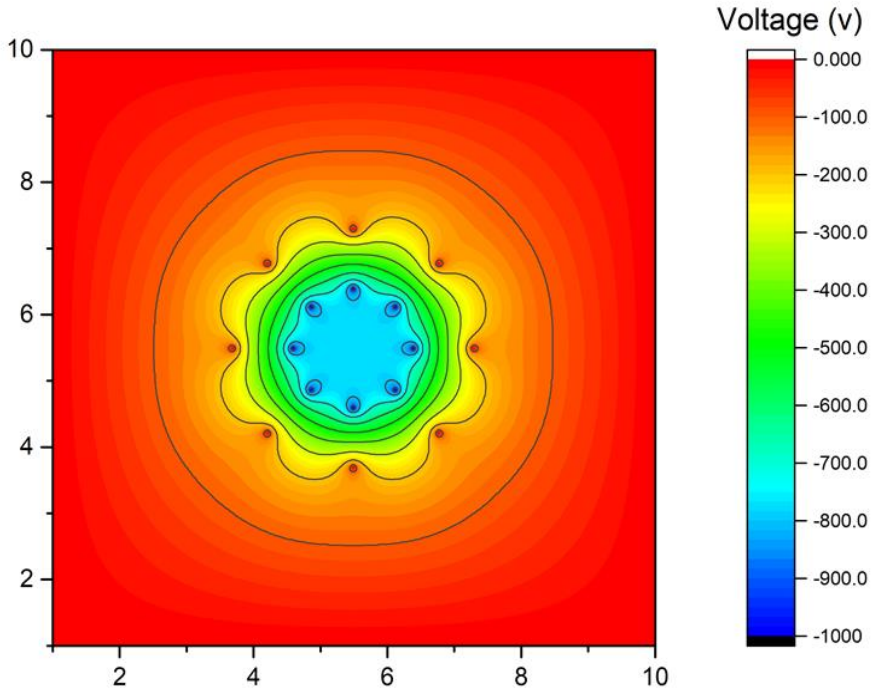

Fig 5-2
Potential Distribution for 8 Wires Aligned Electrodes, 1 kV Applied Voltage

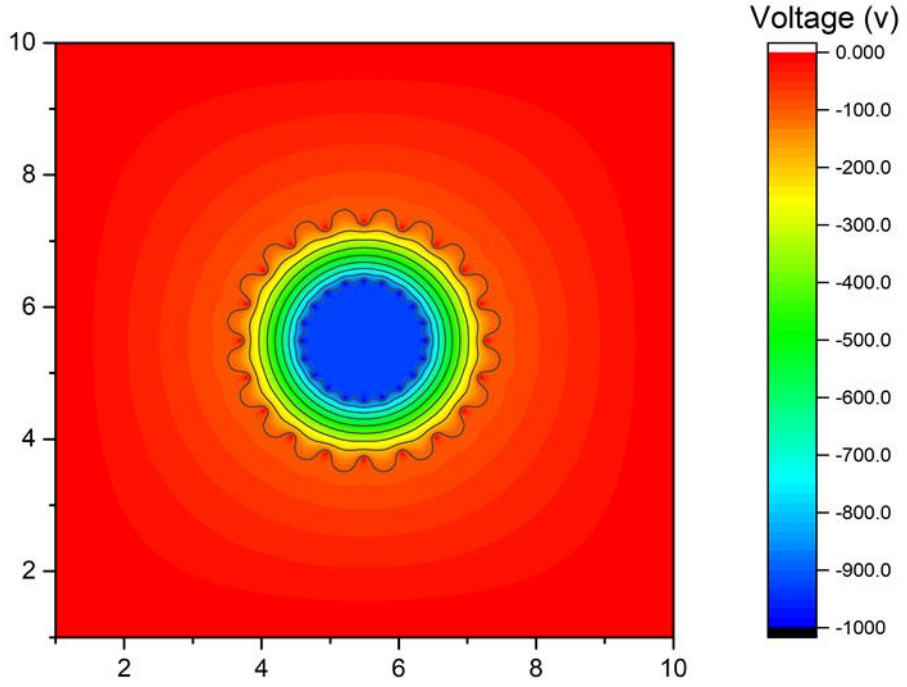

Fig 5-3
Potential Distribution 20 Wires Aligned Electrodes, 1kV Applied Voltage

The results of the simulations for both configurations and the original were plotted in Fig. (5-4) for comparison.

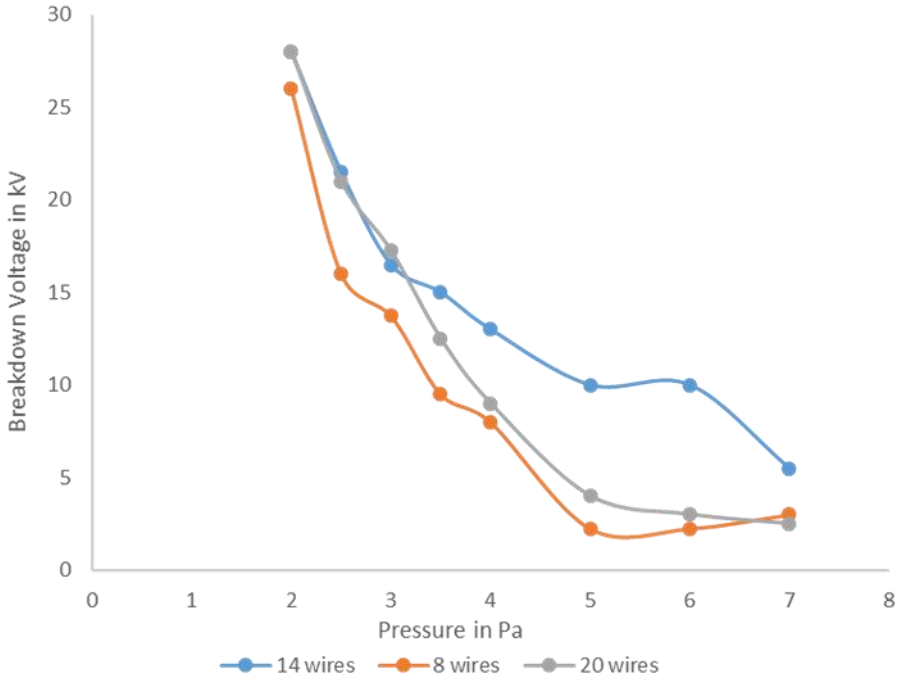

Fig 5-4

Pressure vs breakdown Voltage for Different Wires Number

The plot shows that the 20-wire configuration results are almost the same as the original at very low pressures, but it split from the original for higher pressures and become very close to the 8-wire results. Breakdown voltages for the 8-wire are smaller than those for both the 20-wire and original for the pressures of interest. This is mainly because of the effects of the electrodes' transparency and the potential distribution, so in one hand the ions that hit the electrodes are less and they survive more in case of higher transparent electrodes, while on the other hand the higher electric field between the electrodes causes more ionizations for the higher wires configurations. Essentially, ions in the microchannels are guided through the grid, minimizing interception of the grid wires [1], this noticed from the number of ions converted to neutrals, where is higher remarkably in case of 14 wires.

5.3 The Effect of Changing the Anode Radius and Electrodes Separation

This section describes the results of simulations to investigate the effect of changing the separation of anode and cathode. The original anode has radius of 5.75 cm. In these tests, two new cases were simulated with anode radius of 7.2 cm and 4.3 cm. These correspond to a change in anode radius of 1.25x and 0.75x respectively. Other electrode properties, such as the size of the cathode, the wire radius, the number of electrode wires and the chamber size, were unchanged.

Changing the anode radius should have several broad effects. One effect is that the anode transparency is slightly different, because the anode radius is different but the electrode wires have the same size. This will have the effect of slightly changing the surface area available for surface processes at the anode. A second effect is that the channelling of charge particles through the apertures will be affected, because the separation of the wires on the anode is different for the different cases. The main effect, however, is the change of the magnitude of the electrode field between the anode and cathode, simply because the electrode separation is different. This change will affect the acceleration of charged species during ignition.

More detailed information on the effect of changing the anode radius can be seen in Figures (5-5) and (5-6), which show the vacuum potentials used for two new simulation cases. To view the differences between them. The distributions take the shape of a serrated disk around the electrodes. The outer region beyond the larger anode has very low potential, while there are significant values in the region outside the smaller anode. In a circle of radius almost the same as the larger anode radius, the potential values increase gradually in the area from the larger anode to the cathode, while the smaller anode case, these increase

rapidly and the contours are condensed due to the smaller distance between the electrodes. In both cases the interior of the cathode has almost constant potential not like between the electrodes, but remarkably higher at the apertures for the smaller anode, while the larger has potential closer to that at the electrodes.

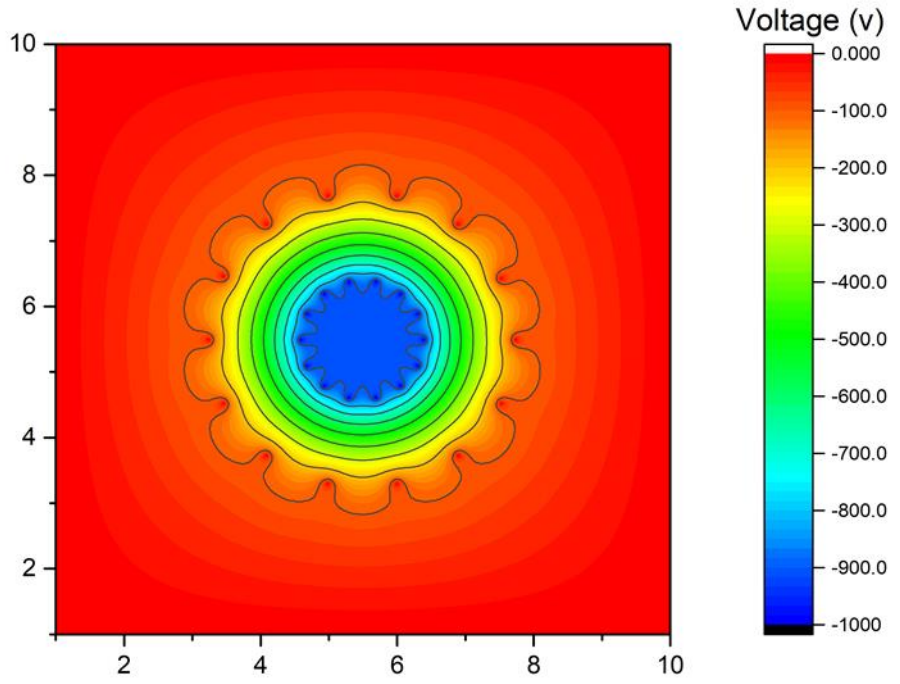

Fig 5-5
Potential Distribution for Larger anode 1.25, 1 kV Applied Voltage

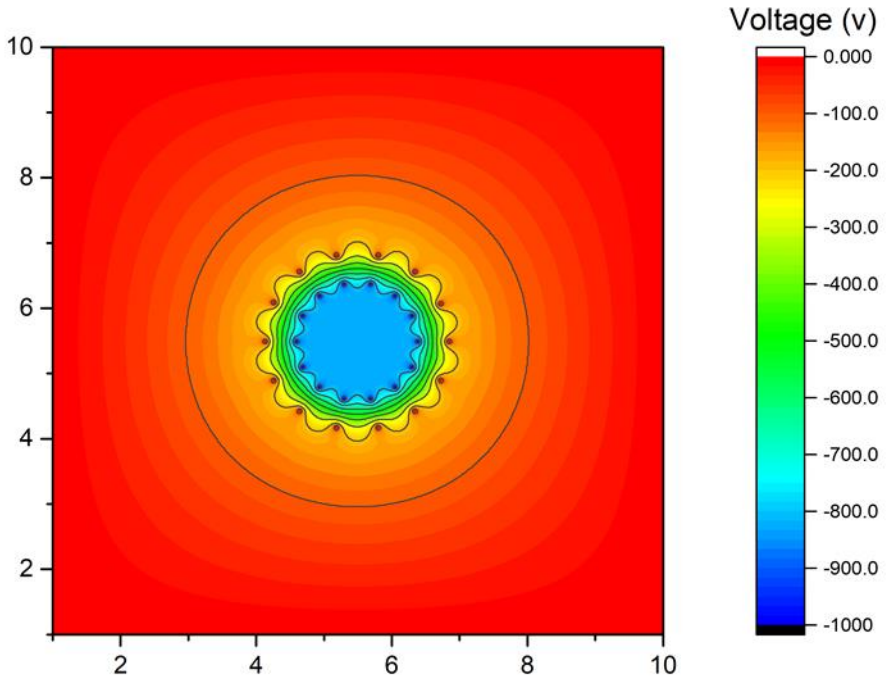

Fig 5-6
Potential Distribution for Smallar Anode, 1kV Applied Voltage

Figure (5-7) shows pressure versus breakdown voltage for the original and these two configurations for comparison.

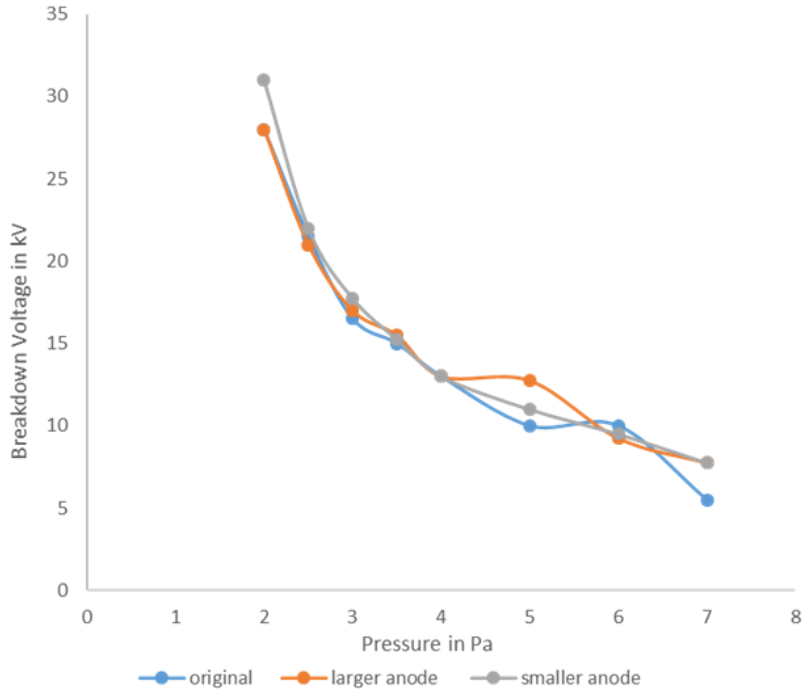

Fig 5-7

Pressure vs breakdown Voltage for Different Anode Radius

The three curves are almost the same, which gives the impression that the effect of changing the anode radius is negligible. In spite of the electrodes separation differences between the cases, the energy gained by an ion is similar, because the potential difference is the same; in the larger anode case the electric field is weaker but compensated by longer path, in addition to that the ions ionization cross section is not very dependent on energy. Plotting the results for *Pd* versus breakdown voltage (conventional Paschen curve) as in Fig. (5-8) shows a different story however, with the curves shifting to the right as the anode radius increase, i.e. the distance between the electrodes d [1,13], so for the same value of *Pd* the breakdown voltage increases as the d increase. The microchannels for the smaller anode are wider and the path that guides the ion to hit the wires are narrower, in addition the ions can be accelerated from outside the anode due to the tangible potential there, and gain higher energy than that for the larger anode in the region between the electrodes. This increase the ability of the ions to ionize neutrals, and the short distance gap may reduce the loss of ions through charge exchange in this region.

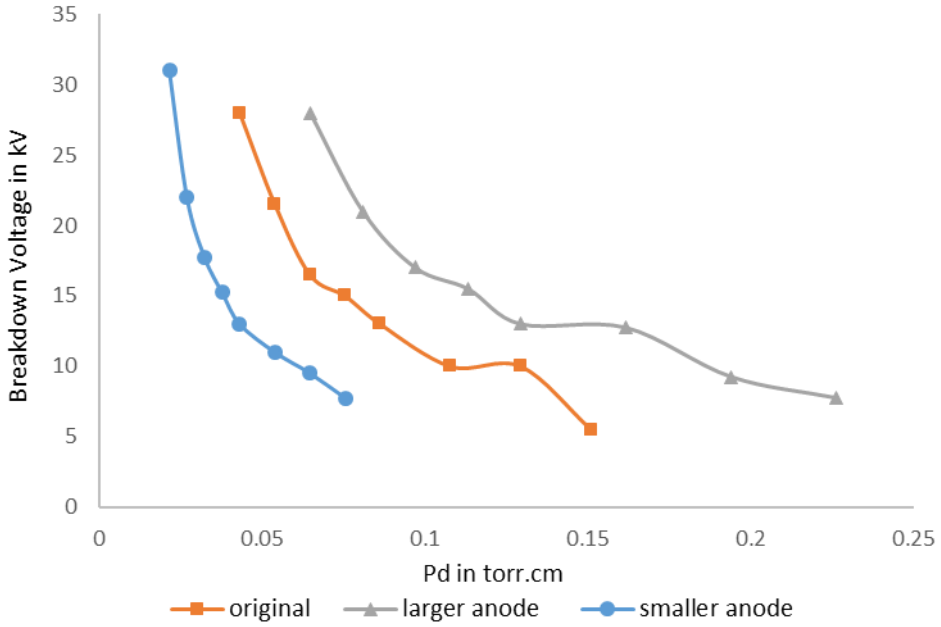

Fig 5-8

Paschen Curvevs for Different Anode Radius

5.4 The Effect of Wires Apertures Alignment of Cathode and Anode

This section explores the effect of making the apertures of the electrodes to not face each other, as in the case of rotating the anode half the angle between two successive wires. This causes the path of the charged particles to intersect with the wires are more possible, in other words their path through the transparent electrodes to be narrower, i.e. narrower microchannels.

Fig. (5-9) shows the potential distribution for such configuration. By comparison with original configuration it seems very similar at the first look, and in the outer region of the anode, the region between the electrodes and the interior of the cathode this is so. A closer look however reveals that the location of the anode wires is shifted and located facing the mid-points between the cathode wires, which leads to the potential around the anode wires being also rotated, which is to be expected, but this raises the possibility of charged particles hitting the electrodes in either direction.

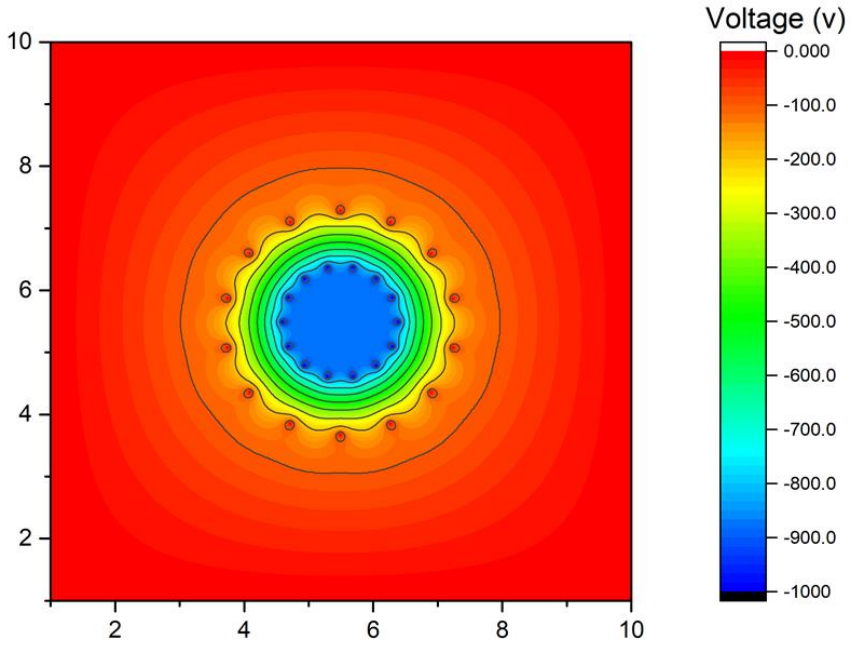

Fig 5-9
Potential Distribution for Half Antiphase, 1 kV Applied Voltage

Figure (5-10) shows simulation result for this configuration compared to the original one.

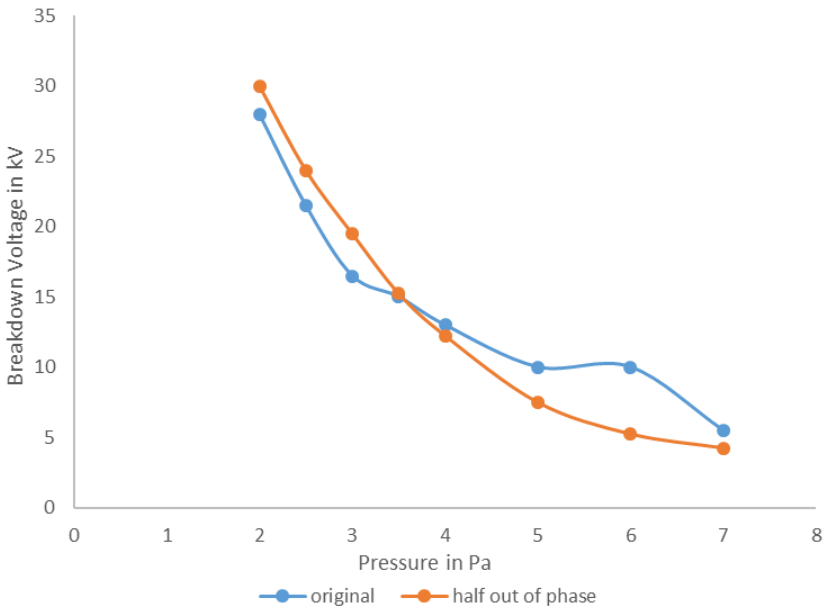

Fig 5-10

Pressure vs breakdown Voltage for Original and Half out of Phase

The cur than the original for low-pressure cases, while they are less for higher pressures. This might be because electrons become more effective as the pressure is increased, since in the out-of-phase configuration the number of ions impacting the cathode are higher and the secondary electron will be more. At low pressures, due to the electron mobility and size they reach the boundaries (wall or anode) and are lost very fast with a small ionization effect, but as the pressure increases the effect of electrons increases also.

5.5 Comparison with Other Work Reported

Miley, George H., et al. [14], reported experimental and simulation work on a single gridded spherical IEC, i.e. where the chamber serves as the anode. They used different cathodes and anode diameters, in order to study the effect of that on transparency and microchanneling. In addition, they studied the hypothesis of effective transparency experimentally by covering the cathode with solid foil except for two holes. Once the holes were arranged 180° apart

and again in a 90° angle. The first gave results close to transparent cathode, in spite of the geometric transparency differences. The second gave results close to the solid hollow sphere cathode results despite having the same geometric transparency. They also stimulated different transparency values, finding that the output with transparency of 99% matches the experimental results of different cathodes and anodes despite the latter being less transparent than this. They concluded that the discharge is a function of effective transparency rather than geometrical. Their work was executed in very low pressure conditions of 5-15 mtorr, this agrees with results in pervious sections, 5.2, 5.3 and 5.4, which agrees with the raise in discharge voltage found at low pressures for out-of-phase electrodes, since this reduces the effective transparency.

Jung, Bong-Ki, et al. [16] investigated cathode radius and transparency effects on a cylindrical IEC, for which the chamber was cylindrical as well. The experiment was done under consistently very low pressures of 1-15 mtorr, and they found that the discharge voltages were unaffected by the cathode radius in case of smaller cathode radius than the electrode gap distance, while it decreased as the cathode radius increased for the cases of larger cathode radius than electrodes gap distance. The last can be compared to the case of the smaller anode simulated here and that is in agreement with this present work.

5.6 Discussion of Other Configuration Changes and Their Effects

There are many changes in configuration that can be made, this work investigates some and may cover other changes, examples are:

(i) Wall and wire material, which mainly effects the SEE and BS of electrons and heavy particles. The SEE has some effect but is not so important at low pressures as results have

shown in Section 4.4.2. The effect BS could cause effects if there is big difference between the stainless steel atomic mass and that suggested wall material.

(ii) Wire diameter, which effects electrodes transparency, which is already discussed though changing number of electrode wires.

(iii) Chamber size, which expected to have influence if its dimension is comparable to the electrodes radius, otherwise this effect has been already investigated in the second test by changing the anode size.

5.7 Summary and Conclusions

In sum, the investigation of making changes in configuration setting has revealed that these changes have influence on:

(i) Potential distribution across the domain, the interior of the cathode, region between electrodes, outside the anode to the chamber's walls and around the wires.

(ii)Effective electrodes transparency rather than geometric transparency, where in spite of changing the number of electrode wire and the anode size, in general, the effect was weak, because the effective transparency is almost the same for these cases, while the breakdown voltage raised in the case of unaligned electrodes compared to aligned one, because the effective transparency reduced in spite of both have the same geometric transparency.

(iii) These two factors influence were linked to the ion microchanneling, because these microchannels are function of the curvature in equipotential surfaces near the electrodes grid, i.e. electrodes potential and grid opening size [13]. Since they are guiding the charged

particle through the electrode grid apertures, the effect on them will cause effect on breakdown, so wider microchannel as in the case of increasing transparency, or condense microchannel as higher potential, will reduce breakdown voltage, and vice versa. So the effective transparency, in addition to the effect of the microchannels that guide the ion trajectory is confirmed by the present work.

(iv) The transition from ion dominate effect on discharge at low pressures to significant effect for electrons at higher pressures was confirmed, where the results showed that the points mentioned above become less effective as the pressure increased, this may justify the star mode in spherical IEC glow discharge at low pressures 0.3-3 Pa which is distinguished by spokes of light emanating through most of the grid holes, while jet mode occurs at higher pressures 3-7 Pa in IEC glow discharge [1,13].

Chapter 6
Summary and Conclusions

This thesis describes research into the breakdown mechanism of a transparent cathode discharge. Existing researches in this field have concentrated mainly on experiments and applications, and there is still a need to understand basic discharge mechanisms such as the discharge ignition process. The aims of the research were to

(i) Develop a particle trajectory calculation that provided a realistic simulation of the breakdown processes,

(ii) To use this code to investigate breakdown in a standard grid geometry, for which experimental results exist, and to identify the most important mechanisms for breakdown at low pressure,

(iii) to use the simulation code to investigate alternative electrode arrangements, in order to understand the way in which electrode geometry affects discharge ignition, and to identify the factors that might lead to breakdown at lower voltages.

The outcomes of the research align relatively well with these aims. There are three principal outcomes, each of which represents an original contribution to the field.

The first achievement of the research is the development of a particle trajectory code that provides a realistic simulation of the discharge ignition processes. This simulation code is simpler than many codes used to simulate low pressure plasma operation, because the particle trajectories are calculated under the vacuum electric fields, and it is assumed that the charge particle densities not to affect these fields. The difficulty, however, lies in the identification of important mechanisms and the wide range of energy over which reaction processes have to be modelled. Most plasma simulation codes require cross-sections over a relatively small range of particle energies, but simulation of TCD breakdown required assembling cross-section sets over a much wider range of energies, and for electron, ion, and neutral-induced reactions.

The accuracy of the particle trajectory simulation was verified by comparing it with experimental results for one particular electrode configuration, which is described in Chapter 4. Although there was not an exact match between experiment and simulation, there was reasonable agreement in the general trend of breakdown voltage with pressure, and good agreement at lower pressures where there is the most interest in TCD plasma applications. The discrepancy between simulation and experiment was attributed to difference between the 2D calculation environment and the 3D aspects of the experiment, and to the possibility of x-ray production by particle impact having some role in ionization. In addition to the effective transparency rather than the geometric, which make the grid look like 99% transparent in experiment even if the real transparency is less than that (say 85%).

The second achievement of the research is the understanding of the processes that influence ignition in a transparent cathode discharge, which is also described in Chapter 4. The reasonable agreement between simulation and experiment meant that the different physical mechanisms could be examined and the most important processes identified. From this analysis, the conclusions were

(i) Individual mechanisms on breakdown such as, ionization by different particles, effects of fast neutrals, and surface effects processes, such as secondary electron emission, particles backscattering, also ion and neutral conversion by reflection, have minimized as the pressure increased.

(ii) Electron backscattering was the most cumulative effect of particle processes on Paschen curves, the comparison was among electron BS, the secondary electron emission and heavy particle conversion by reflection.

(iii) A plot of ions location at the end of simulation showed an accumulation of ion population in the interior of the cathode, and explained as early stages of virtual electrode formation.

The third achievement of the research is the understanding of effect of electrode geometry on the ignition process. Chapter 5 contains a study of the effect of changing the most important geometrical properties of the wire grid electrodes. The properties that were studied were the density of wires, which affects the size of the apertures and the transparency of the grids, the separation of the grids, which mainly affects the vacuum electric fields, and the alignment of the grids, which affects the vacuum fields and especially the channelling of charged particles through the grid apertures. Analysis of the simulation studies of these effects led to the conclusions that

(i) The main effect on breakdown was ion microchannels which guides charged particles through apertures were affected by the vacuum electric field and transparency.

(ii) Effective transparency is the one count rather than geometrical, where at changing the geometrical transparency did not show remarkable differences, while with the same geometric transparency showed some differences as in unaligned electrodes.

(iii) The effects of changing geometry reduced as pressure increased due to the increase of electron effectivity on account of ions effectivity.

The text above highlights the main conclusions from Chapters 4 and 5. A further general conclusion can be drawn from this project research, based on the complete set of work.

A general conclusion is the effectiveness of using a particle trajectory simulation rather than a full particle-in-cell simulation. The results of this research indicate that this computationally less-intensive approach works well for breakdown research, when the assumption of no space-charge allows the vacuum electric fields to be used for the calculation. The limitation of this approach is that the transition from ignition to steady-state discharge cannot be studied, but the gain in calculation time enabled the investigation of different geometries, as done in Chapter 5, to be done in a relatively fast and efficient way.

The simulation offers the opportunity to do more investigation on geometry effects, especially the effect raising the interior of the cathode compared to the distance between the electrodes and both of them compared to the chamber size. In addition to ability to design TCD devices according to the aims targeted to get optimum output.

The code can be developed to 3D simulation rather than 2D to be more realistic to overcome the differences caused by this, and match the experimental conditions for comparison.

Another future work may be proposed, the x-ray effects on breakdown, through measuring x-ray flux in the system and the average energy of x-ray photons for each pressure,

determine the effect of such phenomenon, and if possible find a way to add it to the simulation.

References

1. Miley, George H., and Murali, S. K. 2014. *Inertial electrostatic confinement (IEC) fusion.* Springer.

2. Francis, F. C. 1984. Introduction to Plasma Physics and Controlled Fusion. *Plasma Physics*.

3. Bellan, Paul M. 2008. *Fundamentals of plasma physics.* Cambridge University Press.

4. *Plasma (physics)*

   https://en.wikipedia.org/wiki/Plasma (physics)

5. http://www.plasmaprometeo.unimib.it

6. Bogaerts, Annemie. 1996. *Mathematical modelling of a direct current glow discharge in argon.* Universitaire Instelling Antwerpen.

7. Wagenaars, Erik. 2006. Plasma breakdown of low-pressure gas discharges. *Dissertation Abstracts International* 68, no. 02:.

8. Druyvesteyn, MJ, and Fi M. Penning. 1940. The mechanism of electrical discharges in gases of low pressure. *Reviews of Modern Physics* 12, no. 2:87.

9. *Paschen's Law* 2017. https://en.wikipedia.org/w/index.php?title=Paschen%27s_law&oldid=809496574.

10. Lieberman, Michael A., and Allan J. Lichtenberg. 1994. Principles of plasma discharges and materials processing. *MRS Bulletin* 30, 899-901.

11. Dolan, TJ. 1994. Magnetic electrostatic plasma confinement. *Plasma Physics and Controlled Fusion* 36, no. 10:1539.

12. Lavrent'ev, OA, et al. 1963. Jenergiya i plotnost'ionov v jelektromagnitnoj lovushke. *Ukrain Fiz* 8, 440-445.

13. Meyer, Ryan M., Mark A. Prelas, and Sudarshan K. Loyalka. 2008. Experimental observations of a spherical transparent cathode glow discharge. *IEEE Transactions on Plasma Science* 36, no. 4:1881-1889.

14. Miley, George H., et al. 1997. Discharge characteristics of the spherical inertial electrostatic confinement (IEC) device. *IEEE Transactions on Plasma Science* 25, no. 4:733-739.

15. Hagelaar, Gerardus J. M. 2000. *Modelling of microdischarges for display technology.* Technische Universiteit Eindhoven Eindhoven.

16. Jung, Bong-Ki, et al. 2011. Study on Discharge Characteristics of a Cylindrical Inertial Electrostatic Confinement (IEC) Device for High-Yield Fusion Sources. *Fusion Science and Technology* 60, no. 1T:107-111.

17. Hochberg, Timothy A. 1992. Characterization and Modelling of the Gas Discharge in a SFID Neutron Generator. M.S. thesis, Department of Nuclear Engineering, University of Illinois at Urbana-Champaign

18. Birdsall, Charles K. 1991. Particle-in-cell charged-particle simulations, plus Monte Carlo collisions with neutral atoms, PIC-MCC. *IEEE Transactions on Plasma Science* 19, no. 2:65-85.

19. Alves, MV, MA Lieberman, V. Vahedi, and CK Birdsall. 1991. Sheath voltage ratio for asymmetric rf discharges. *Journal of Applied Physics* 69, no. 7:3823-3829.

20. Birdsall, Charles K., and Langdon, A. B. 2004. *Plasma physics via computer simulation.* CRC Press.

21. Hockney, Roger W., and Eastwood, James W. 1988. *Computer simulation using particles.* CRC Press.

22. Tskhakaya, David. 2008. The particle-in-cell method. In *Computational Many-Particle Physics* Springer.

23. Hartmann, P., et al. 2000. Effect of different elementary processes on the breakdown in low-pressure helium gas. *Plasma Sources Science and Technology* 9, no. 2:183.

24. Xu, Liang, Alexander V. Khrabrov, Igor D. Kaganovich, and Timothy J. Sommerer. 2017. Investigation of the Paschen curve for helium in the 100–1000 kV range. *Physics of Plasmas* 24, no. 9:093511.

25. Skullerud, HR. 1968. The stochastic computer simulation of ion motion in a gas subjected to a constant electric field. *Journal of Physics D: Applied Physics* 1, no. 11:1567.

26. Nanbu, Kenichi. 1994. Simple method to determine collisional event in Monte Carlo simulation of electron-molecule collision. *Japanese journal of applied physics* 33, no. 8R:4752.

27. Nanbu, Kenichi. 2000. Probability theory of electron-molecule, ion-molecule, molecule-molecule, and Coulomb collisions for particle modeling of materials processing plasmas and gases. *IEEE Transactions on Plasma Science* 28, no. 3:971-990.

28. Langley, Robert A., et al. 1984. Data compendium for plasma-surface interactions. *Nuclear Fusion* 24, no. S1:S9.

29. Baglin, V., et al. 2000. *The secondary electron yield of technical materials and its variation with surface treatments*.

30. Szapiro, B., JJ Rocca, and T. Prabhuram. 1988. Electron yield of glow discharge cathode materials under helium ion bombardment. *Applied Physics Letters* 53, no. 5:358-360.

31. El Gomati, MM, CGH Walker, AMD Assa'd, and M. Zadražil. 2008. Theory experiment comparison of the electron backscattering factor from solids at low electron energy (250–5,000 eV). *Scanning* 30, no. 1:2-15.

32. Thomas, TM, Herschel Neumann, AW Czanderna, and JR Pitts. 1986. Scattered ion yields from 0.2 to 2 keV helium neutral or ion bombardment of solids. *Surface Science*175, no. 2:L737-L746.

33. Souda, R., and M. Aono. 1986. Interactions of low-energy He^{+}, He^{0}, and He^{*} with solid surfaces. *Nuclear Instruments and Methods in Physics Research Section B: Beam Interactions with Materials and Atoms* 15, no. 1-6:114-121.

34. Press, William H. 2007. *Numerical recipes 3rd edition: The art of scientific computing.* Cambridge university press.

35. Vahedi, Vahid, and G. DiPeso. 1997. Simultaneous potential and circuit solution for two-dimensional bounded plasma simulation codes. *Journal of Computational Physics*131, no. 1:149-163.

36. Bittencourt, José A. 2013. *Fundamentals of plasma physics.* Springer Science & Business Media.

37. Goldston, Robert J., and Rutherford, Paul H. 1995. *Introduction to plasma physics.* CRC Press.

38. Fowles, Grant R., and Cassiday, George L. 1999. *Analytical mechanics.* Saunders College.

39. *Elastic Collision*

http://williamecraver.wix.com/elastic-equations

40. *Elastic Collision*

https://en.wikipedia.org/wiki/Elastic_collision

41. Vahedi, Vahid, and Maheswaran Surendra. 1995. A Monte Carlo collision model for the particle-in-cell method: applications to argon and oxygen discharges. *Computer Physics Communications* 87, no. 1-2:179-198.

42. Alves, LL, et al. 2013. Comparisons of sets of electron–neutral scattering cross sections and swarm parameters in noble gases: II. Helium and neon. *Journal of Physics D: Applied Physics* 46, no. 33:334002.

43. Ralchenko, Yu, et al. 2008. Electron-impact excitation and ionization cross sections for ground state and excited helium atoms. *Atomic Data and Nuclear Data Tables* 94, no. 4:603-622.

44. Cramer, WH, and JH Simons. 1957. Elastic and Inelastic Scattering of Low-Velocity He Ions in Helium. *The Journal of chemical physics* 26, no. 5:1272-1275.

45. Hegerberg, R., Thorarinn Stefansson, and MT Elford. 1978. Measurement of the symmetric charge-exchange cross section in helium and argon in the impact energy range 1-10 keV. *Journal of Physics B: Atomic and Molecular Physics* 11, no. 1:133.

46. Okasaka, R., Y. Konishi, Y. Sato, and K. Fukuda. 1987. Excitation cross section in He - He collisions. I. Excitation function and potential curve crossing. *Journal of Physics B: Atomic and Molecular Physics* 20, no. 15:3771.

47. Gilbody, HB, and Hasted, JB. 1957. *Ionization by positive ions.* Vol. 240. The Royal Society.

48. A. V. Phelps, see https://jila.colorado.edu/~avp/collision_data/ for crosssection data on elastic scattering of neutral helium atoms on each other.

49. Kempter, V., F. Veith, and L. Zehnle. 1975. Excitation processes in low-energy collisions between ground state helium atoms. *Journal of Physics B: Atomic and Molecular Physics* 8, no. 7:1041.

50. Hayden, Howard C., and Nyle G. Utterback. 1964. Ionization of helium, neon, and nitrogen by helium atoms. *Physical Review* 135, no. 6A:A1575.

51. Barnett, CF, et al. 1990. ATOMIC DATA FOR FUSION VOLUME. *ORNL* 6086, V1.

52. Kadota, Kiyoshi, and Yozaburo Kaneko. 1974. Secondary electron ejection from contaminated metal surface by He and Ar atoms. *Japanese Journal of Applied Physics* 13, no. 10:1554.

53. Paetow, H., and W. Walcher. 1938. über den Einfluß von Adsorptionsschichten auf die Auslösung von Elektronen und die Reflexion von Ionen beim Auftreffen von positiven Caesiumionen auf Wolfram. *Zeitschrift für Physik* 110, no. 1-2:69-83.

54. Berry, HW. 1958. Liberation of Electrons by Fast Neutral Helium Atoms from a Tungsten Target. *Journal of Applied Physics* 29, no. 8:1219-1225.

55. Utterback, Nyle G. 1963. Ionization of nitrogen and oxygen molecules by nitrogen and oxygen molecules. *Physical Review* 129, no. 1:219.

56. Thomas, EW, RK Janev, and J. Smith. 1992. Scaling of particle reflection coefficients. *Nuclear Instruments and Methods in Physics Research Section B: Beam Interactions with Materials and Atoms* 69, no. 4:427-436.

57. Eckstein, Wolfgang. 2010. Reflection (backscattering). *Bulletin of the Russian Academy of Sciences: Physics* 74, no. 2:141-148.

58. Darlington, EH. 1975. Backscattering of 10-100 keV electrons from thick targets. *Journal of Physics D: Applied Physics* 8, no. 1:85.

59. Hardiment, Thomas. 2017. Operating characteristic of a Transparent Cathode Discharge. PhD Thesis. University of Liverpool, Liverpool.